

Molecular Dynamics Simulation of Gold Growth on MnAs

Inauguraldissertation
zur Erlangung des Doktorgrades
der Naturwissenschaften
(Dr. rer. nat.)

von
Andreas Rühl
geboren am 14. Juni 1987 in Alsfeld

Oktober 2016

Betreut durch Prof. Dr. Christian Heiliger

Institut für Theoretische Physik
AG Festkörpertheorie
Justus-Liebig-Universität Gießen



We are not enemies, but friends. We must not be enemies. Though passion may have strained, it must not break our bonds of affection. The mystic chords of memory will swell when again touched, as surely they will be, by the better angels of our nature.

ABRAHAM LINCOLN
First Inaugural Address (1861)
abridged excerpt

Contents

1	Introduction	1
2	Theoretical Background	5
2.1	Molecular Dynamics (MD)	5
2.1.1	MD Basics	6
2.1.2	Effective Potentials	16
2.1.3	Integration Schemes and Thermostats	18
2.2	Force Matching (FM)	23
2.2.1	FM Basics	23
2.2.2	<i>potfit</i> : An Implementation of FM	24
3	Generation of Effective Potentials	29
3.1	Fitting Strategies	29
3.1.1	Basic Setup	32
3.1.2	General Remarks	35
3.2	Effective Potential for the MnAs/Au Interface System	37
3.2.1	Fitting Process of the Potential	37
3.2.2	Validation of the Potential	45
4	Simulation Results	53
4.1	Surface Simulations	53
4.1.1	Simulation Setup and Settings	54
4.1.2	Analysis of the Different Surfaces of MnAs	56
4.2	Deposition Simulations of Au on MnAs	63
4.2.1	Deposition on the {10-10} _{As} 1 Surface Termination	63
4.2.2	Analysis of the Grown Gold Structure	66
5	Conclusions	71
	Appendix: MnAs/Au EAM potential	75
	Bibliography	86
	Danksagung	87

1 Introduction

Motivation. Manganese arsenide (MnAs) is an interesting transition metal compound. It is ferromagnetic above room temperature [1]. It can be grown as clusters in arranged patterns on gallium arsenide (GaAs) substrates [2–4]. The pattern of those clusters have great tunability, since the mean distance between clusters, the cluster size, and the cluster shape are individually adjustable (see Figure 1.1). Further, the Curie temperature of the clusters is around 340 K, which is higher than the one for bulk MnAs ($T_c = 318$ K) [5]. All of this makes MnAs a promising material for electronic devices with integrated magnetic elements, so-called magnetoelectronic devices.

The most prominent application of magnetoelectronic devices is the data storage on computers. Like it is the case for most magnetoelectronic devices, such applications make use of the giant magnetoresistance (GMR) [6, 7] or tunnel magnetoresistance (TMR) [8]. In both cases two ferromagnetic layers are separated by a thin non-magnetic metal layer (GMR) or insulating layer (TMR). Depending on the relative orientation of the magnetization of the ferromagnetic layers, the resistance through the layer system is higher – anti-aligned magnetizations – or lower – aligned magnetizations – due to low or high spin-dependent scattering, respectively.

The magnetoresistance effect can be utilized in any applications where magnetic fields have to be measured. However, the commercially biggest impact was the introduction of the GMR in read heads of magnetic hard disk drives for computer storage [9]. A GMR element or – more likely today – a TMR element sitting at the top of the read head is used to read the storage information on the disk, which is saved as magnetized regions representing the data bits of 0 and 1.

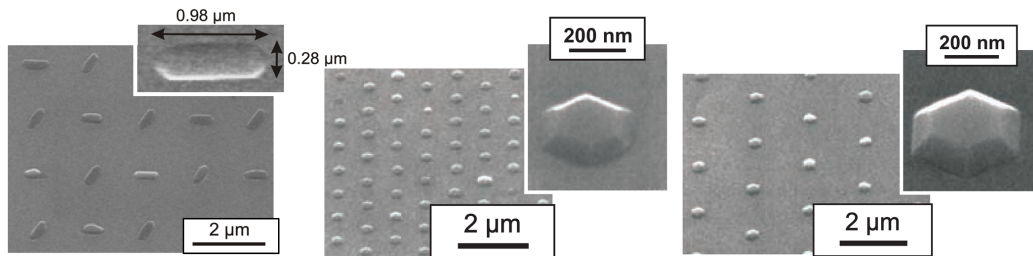


Figure 1.1. Scanning electron microscope (SEM) pictures of the different shaped, sized, and arranged MnAs nanocluster: The diameter of the clusters varies between 170 nm and 1.2 μm [4].

Such kind of storage devices are non-volatile, as the information does not get lost when the power-supply is shut down. In contrast to that, dynamic random-access memory (DRAM) – currently used as main memory of computers – is volatile, since each data bit is stored as electrical charge in one capacitor (1C) accessed by one transistor (1T) [10]. Those 1T1C cells are arranged in two-dimensional arrays, making it possible to access any data bit in almost constant time, independent of its physical location. This is not the case for conventional, non-volatile hard drives, as the data access depends on the physical location due to, for example, rotation speed of the disk and arm movement of the read head [11].

In order to combine both advantages – non-volatile and random-access – magnetoresistive RAM (MRAM) devices have been proposed and developed since the early 90s [12]. The basic setup of MRAM devices is a planar array of GMR or TMR elements on a substrate. Reading the storage bit of each element is done by measuring the magnetoresistance of the layered structure, with layers oriented parallel to the substrate. For writing the concept of a spin-valve is introduced. The magnetization of one of the ferromagnetic layers is kept fixed (hard layer), while the other can be easily changed by an external magnetic field (soft layer) [13]. There are different approaches as to how the soft layer is switched. The field-induced switching – achieved by currents through nearby wires – has a scale limitation, since the current has to be increased when reducing the wires. The diameter of the minimal possible element is 90 nm [12]. A switching utilizing the spin-transfer torque (STT) [14] – a spin current through the layer rotates the magnetization – does not have such scaling problems. Recent research by Nowak and co-workers from IBM shows promising results for an STT-MRAM 4 kbit chip on which individual device sizes were tested [15].

In MRAM devices the layers of GMR or TMR elements are stacked perpendicular to the substrate. This is also true for other magnetoelectronic devices, since GMR or TMR structures are usually made from thin film structures. Integrating those kinds of geometries into larger planar device concepts – like in MRAM concepts – is challenging. From the manufacturing point of view, current flows perpendicular to the surface are not ideal [4].

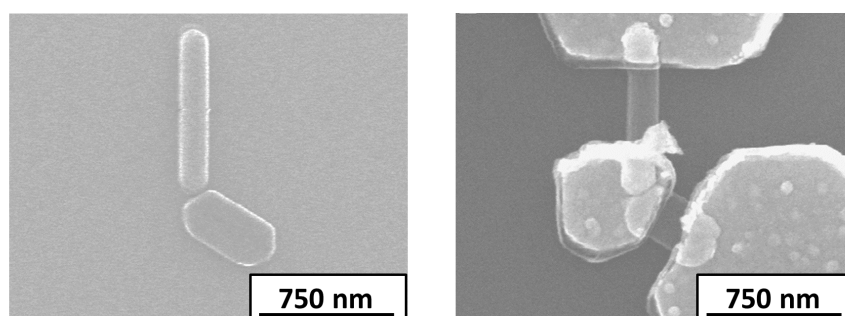


Figure 1.2. SEM pictures of two elongated MnAs nanocluster with a gap of about 10 nm: The structure is shown before (left) and after (right) connecting the clusters by gold deposition (as well as contact stripes). The dimensions of the resulting GMR-like device structure are about 870 nm for the long cluster and 540 nm for the shorter cluster [16].

An alternative architectural approach is to create planar GMR devices, which are parallel to the substrate. This can be realized with hybrid structures like MnAs nanocluster on GaAs. Figure 1.2 displays such an example. The simplest magneto-electronic device has been constructed by connecting two MnAs clusters – grown in close proximity to each other – with the help of thermal deposition of gold in the cluster gap. Martin Fischer et al. performed magnetotransport measurements through such arrangements of nanoclusters and observed magnetoresistance effects as well as spin-valve like behavior of the structure [17]. Heiliger et al. calculated theoretically the electrical transport through planar structures consisting only of MnAs clusters [18]. Calculations of electrical transport through MnAs cluster arrangements including gold layers are only possible, if the exact structure of gold on MnAs is known. This leads to the main objective of this work, since the gold/MnAs interface structure is unknown by experiment or theory and investigating it is a crucial step for further research. Another interesting research question concerns the exact structure of the surface facets of the MnAs nanocluster, as little is known about the surface reconstructions of those crystal facets [2].

In order to investigate the raised question of how the gold grows on a MnAs surface, a combined approach of Molecular Dynamics and Force Matching has been chosen. Molecular Dynamics (MD) is an established computer simulation method for simulating the classical movements of atoms or molecules. Among other applications the method is able to simulate the atomic deposition on a substrate. That kind of problem – deposition simulations with MD – has been already applied several times in research for different material systems, including surface analysis [19–24]. However, MD simulations for the system of MnAs and gold – either in the case of deposition simulations or for any other research problem – have never been done. This means that there is no effective potential available in literature, which is needed to describe the interaction in an MD simulation. Therefore, the method of Force Matching is used additionally to create an effective potential by fitting a potential model to *ab initio* reference data. In this way, since the effective potential is still based on *ab initio* data, the approach with MD and Force Matching keeps the predictive power of *ab initio* calculations. The alternative approach with *ab initio* MD is not appropriate, as in this case the interaction is represented by full quantum mechanical calculations in each simulation time step, which would be too time consuming for a large-scale atomic deposition simulation.

Outline. This thesis is divided into five chapters. Chapter 1 – the above introduction of the thesis – is followed by setting the theoretical background for the thesis in Chapter 2. This includes the basics of Molecular Dynamics (Section 2.1) and Force Matching (Section 2.2). Chapter 3 gives details on fitting strategies for the generation of effective potentials by providing general concepts as well as explicit setup rules in Section 3.1. It also presents the created effective potential for MnAs and gold, continued by the validation of the potential in Section 3.2. In Chapter 4 the simulation results obtained with the force-matched potential are discussed. The first half of the chapter (Section 4.1) is dedicated to the surface simulations – preparing steps for the deposition simulations – and the subsequent analysis of the different

surfaces of MnAs. In the second half (Section 4.2) the results of the actual deposition simulation of gold on MnAs and the analysis of the grown gold structure are presented. The thesis ends with a summary of the main conclusions in Chapter 5.

2 Theoretical Background

As already mentioned, Molecular Dynamics is the main method for the investigation of the physical problem at hand. Hence, most of the theoretical background is about this established and popular simulation method. Since the conducted simulations apply force-matched potentials, the basics of the complementary method of Force Matching build the second big part of the chapter.

2.1 Molecular Dynamics

In Molecular Dynamics – also commonly abbreviated as MD – one solves Newton’s equations of motion of a many-body particle system numerically in discrete time steps. This basic summary of MD is a good starting point and guideline to get to know the main concepts of Molecular Dynamics:

1. A *discrete time step* in MD consists of the following: Calculating the forces between a set of particles with positions and velocities and afterwards obtaining new positions and velocities of the system via Newton’s second law and the previously calculated forces. This concludes one time step. It will be repeated in a loop as often as time steps are required, resulting in a discrete time evolution of the many-body particle system.
2. The many-body problem in MD needs to be treated *numerically* as only the two-body problem can be solved analytically. The two-body problem has been thoroughly investigated in the field of astronomy where the analytic solution can be expressed by Kepler’s laws of planetary motions. In case of the three-body problem, there exists in general no analytic solution. The three-body problem has been also discussed most prominently in the field of astronomy.
3. The particles of the *many-body particle system* can be chosen as molecules, as it might be suspected when looking at the name of MD. Molecules will occur mostly in research areas like biology or chemistry. Since this work is centered in solid state physics, the investigated systems consists of atoms, usually in the crystallized state. However, in both cases only atoms or molecules are described explicitly, the corresponding electrons are in general just included effectively (see the following section for details).

4. MD can be employed wherever *Newton's equations of motion* apply and the system behaves classically. In most cases atoms can be approximated as classical particles, as it will be discussed later. The use of Newtonian mechanics also means that MD is deterministic, in comparison to the related Monte Carlo simulation method which is of stochastic nature.

First introduced by Alder and Wainwright in the 1950s [25], MD was largely responsible for establishing computer simulations as a third valid approach besides theory and experiment. The success of this rather new research field was and still is strongly linked to the emergence of computing powers over the last decades, making it possible to simulate significantly large system sizes. Lying in between of theory and experiment, computer simulations combine elements of both. Thus, it is more than reasonable to name the field also computer experiments or numerical experiments. Like in an experiment one has to set up a sample first and then investigate the evolvment of the system over time. On the other hand, it is still purely theoretical. Broken down, it is a calculation on a computer, solving the basic theoretical equations of physics.

2.1.1 MD Basics

Quantum Mechanical Foundations. In its core MD is built upon Newton mechanics. Like mentioned above, this work employs simulations of atoms in the research field of solid state physics, a research field where at first glance it may be a natural concern to ask why classical Newton laws should work there. But as a matter of fact, the foundations for the justified use of MD in this case is directly linked to the non-relativistic quantum mechanical equation of motion: the stationary many-body Schrödinger equation of the solid state¹

$$\hat{H}\Psi(\mathbf{r}, \mathbf{R}) = E\Psi(\mathbf{r}, \mathbf{R}), \quad (2.1)$$

with

$$\hat{H} = \hat{T}_n + \hat{T}_e + \hat{V}_{n-n} + \hat{V}_{e-e} + \hat{V}_{e-n}. \quad (2.2)$$

The arguments of the many-body wave function Ψ of a system of atoms are the positions of the electrons $\mathbf{r} = (\vec{r}_1, \dots, \vec{r}_{N_e})$, a $3N_e$ -dimensional vector with N_e being the number of electrons, as well as the positions of the nuclei $\mathbf{R} = (\vec{R}_1, \dots, \vec{R}_{N_n})$, being the $3N_n$ -dimensional vector of N_n nuclei. \hat{T} is the operator corresponding to the kinetic energy of the nuclei or the electrons respectively. \hat{V}_{i-j} represents the operator for the Coulomb pair interaction with an index defining the interaction partners i and j .

¹ Notation of the stated equation and the following derivation of the Born-Oppenheimer approximation are based on [26].

The next step in solving the many body Schrödinger equation is applying the Born-Oppenheimer approximation. The relatively low mass ratio of electrons to nuclei makes it possible to treat the kinetic energy of the nuclei as a distortion, $\hat{H} = \hat{H}_0 + \hat{T}_n$, allowing to decouple the motion of nuclei and electrons. The electrons – adapting almost instantly to the positions of the nuclei – move as if there are in a potential of fixed nuclei. This leads to a Schrödinger equation just for the electrons, since the nuclei only enter the equation as a parameter due to their position \mathbf{R} ,

$$\hat{H}_0\phi_\alpha(\mathbf{r}, \mathbf{R}) = \varepsilon_\alpha(\mathbf{R})\phi_\alpha(\mathbf{r}, \mathbf{R}). \quad (2.3)$$

For every parameter \mathbf{R} there is a full basis set of quantum mechanical states denoted by the electronic quantum number α . Hence, for every fixed \mathbf{R} the analytic $\Psi(\mathbf{r}, \mathbf{R})$ of the general problem (2.1) can be expanded in this set, meaning

$$\Psi(\mathbf{r}, \mathbf{R}) = \sum_{\alpha} \chi_{\alpha}(\mathbf{R})\phi_{\alpha}(\mathbf{r}, \mathbf{R}). \quad (2.4)$$

After inserting the above expansion in (2.1) and some further calculations – including the usage of the above mentioned low mass ratio – we get another Schrödinger equation, this time just for the nuclei

$$(\hat{T}_n + \varepsilon_{\alpha}(\mathbf{R}))\chi_{\alpha}(\mathbf{R}) = E\chi_{\alpha}(\mathbf{R}). \quad (2.5)$$

The energy eigenvalues of the electrons – depending parametrically on the nuclei positions \mathbf{R} – act as the effective potential for the nuclei. $\varepsilon_{\alpha}(\mathbf{R})$ is the high-dimensional energy hypersurface defining the movements of the nuclei.

The focus lies now on the last equation: the Schrödinger equation for the nuclei. There is no explicit description of electrons in MD, at least concerning the actual time evolution of the many-body system. One usually speaks of atoms in MD suggesting the electrons are somehow included directly, but that is only due to terminology. They are represented indirectly by the eigenenergies $\varepsilon_{\alpha}(\mathbf{R})$ of course.

At this point the foundations stop being fully quantum mechanical.² Instead of solving the Schrödinger equation (2.5), one considers the electronic ground state $\varepsilon_0(\mathbf{R})$ as the effective potential V_{eff} and puts it into Newton's equation of motions for the nuclei or – from now on – atoms with masses m_i

$$m_i \frac{d^2 \vec{R}_i}{dt^2} = \vec{\nabla}_i V_{\text{eff}}(\mathbf{R}) = \vec{F}_i. \quad (2.6)$$

The justification for this final step to Newtonian mechanics is done in the scope of the Ehrenfest theorem. There, one can show the correspondence principle stating that Newton's laws are included in the laws of quantum mechanics when going to the classical limit. This limit is applicable for the relatively heavy atoms behaving like classical particles. If the *de Broglie* wavelength $\lambda_{\text{Br}} = \hbar/p$ of a particle with momentum p has a magnitude significantly smaller than other characteristic quantities

² As long as the effective potential is based in some way on quantum mechanical *ab initio* calculations, one could argue that the whole approach is still partly quantum mechanical or semi-classical.

of the system, quantum effects are negligible. Assuming a mean thermal velocity of $v_{\text{th}} \propto \sqrt{k_{\text{B}}T/m}$ at temperature T , the following approximation should hold for the system to be still classical [27],

$$\lambda_{\text{Br}} = \frac{\hbar}{p} \propto \frac{\hbar}{\sqrt{mk_{\text{B}}T}} \ll \begin{cases} \text{length of interaction,} \\ \text{mean inter-particle distance,} \end{cases} \quad (2.7)$$

with k_{B} being the Boltzmann constant and \hbar being the Planck constant divided by 2π . Thus, very light atoms like hydrogen or helium can be problematic as well as systems at extremely low temperatures (further details in [27]).

Depending on how the effective potential or the forces in (2.6) are evaluated, MD can be split in two separate branches: *ab initio* MD and classical MD.³ One possibility is to do a full quantum mechanical calculation of the electronic ground state in each time step by solving the electronic Schrödinger equation (2.3) with *ab initio* methods. Hence, this branch is called *ab initio* MD. In that regard – meaning the force calculation – the electrons are treated explicitly, while keeping in mind the earlier statement about the treatment of electrons in MD being not explicit.

The other possibility is approximating the effective potential by a model – represented by analytic or tabulated functions – to reproduce the energy hypersurface. As it is the originally proposed approach, the branch is referred to as classical MD. The parameters of the models are determined by fits to reference data, which is theoretical – or more precisely – *ab initio* data in this work. The notion “classical” should not be confused in the way that this approach is more classical than *ab initio* MD since *ab initio* MD uses Newton’s equation as well. Even further, by using force-matched potentials – effective potentials based on *ab initio* data – the concept remains still *ab initio*.⁴

When comparing both branches, one has to acknowledge the simple fact that classical MD includes a considerable approximation by modeling the high-dimensional energy hypersurface. The forces in *ab initio* MD are calculated accurately, at least in the context of approximations needed to solve the Schrödinger equation with *ab initio* methods (details in [26]). To be fair, the full quantum mechanical calculation in an *ab initio* MD step is usually done with a lower accuracy than the *ab initio* calculation of the reference data for a potential model. The *ab initio* MD would take too much time otherwise. Nevertheless, the models can only achieve an effective representation of the quantum mechanical effects and interactions as the electrons are left out explicitly, leading to a certain loss of accuracy. The successful description of the energy hypersurface – and with that the implicit representation of the electrons – depends strongly on the set of *ab initio* data and the quality of the potential model. An important aspect which will be discussed in further details in Section 3.1.

³ Aspects of *ab initio* MD and classical MD are partly based on [28]. Exact details on the foundations of *ab initio* MD and its different types – for example Ehrenfest or Car-Parrinello MD – can be also found there.

⁴ Of course, the statement is not true for empirical potentials, i.e., potentials based on experimental data.

Despite the shortcomings of classical MD, the effective models work surprisingly well as it has been proven multiple times in research since the introduction of MD [28]. Classical MD has not been replaced by *ab initio* MD because in question of simulation duration and system size it is strikingly superior over *ab initio* MD. A time step requires a full *ab initio* calculation, which can take up to several hours or even days depending on the system size. Furthermore, the system size itself is limited as only a calculation in the range of hundreds of atoms is still computationally feasible. A simulation in classical MD can easily have millions of atoms, system sizes which seem to be limitless in comparison. The same holds for the number of time steps. Responsible for those advantages is the fast calculation of the forces. In one time step classical MD just needs to evaluate the functions of the models and their derivatives.

This work applies classical MD with force-matched potentials, since deposition simulations require both, a reasonable large system size and a significant number of time steps. Furthermore, force-matched potentials are applied to keep an *ab initio* description. Consequently, in the following MD always refers to this classical MD approach without further notice.

Numerical Aspects and the Phase Space of Statistical Mechanics. The above section is dedicated to justify the use of MD as a tool for atomistic simulations. There, the forces between the atoms and especially their origin in quantum mechanics were focus of the discussion. But up to now, it was never mentioned how – with knowledge of those forces – Newton’s equation of motions are solved, besides the fact that it is done numerically. This numeric integration of Newton’s equation of motions is not exact, leading to some undesirable long-term behavior of an MD simulation. *Symplecticity* – a special property of an integration scheme – and *ergodicity* – a concept from statistical mechanics – ensure that MD is still producing meaningful results despite the downside. A fact suggesting the following aspects can be called numerical foundations of MD, in the same way like it were the quantum mechanical foundations in the previous section.

To get an idea of symplecticity and ergodicity some basic principles of statistical mechanics need to be introduced. However, the introduction will be by no means a complete rendition of this subject.⁵ For in-depth details the reader is referred to standard works on statistical mechanics.

Looking at experiments and MD simulations, at first sight the direct connection between simulation results and experimental measurements is missing. In MD one has the microscopic knowledge of positions and velocities of every particle. This data is not accessible in experiment, at least when dealing with atomic particles. In experiment macroscopic properties are measured, quantities like temperature or pressure. The precise link between those two kinds of data is provided by the theory of statistical mechanics, drawing the connection from the microscopic states (microstates) to the macroscopic states (macrostates).

⁵ It loosely follows an extraction of the textbook *Thermodynamics and Statistical Mechanics* by Greiner et al. [29]

The first thing to do is to give a precise description of the microstate of a many-body system. Knowing all generalized coordinates $q(t)$ and momenta $p(t)$ at any time defines the complete motion of the system. A microstate of a system with N particles is identified as a set (q_ν, p_ν) with $\nu = 1, \dots, 3N$, which is interpreted as a point in a $6N$ -dimensional space, called phase space. The Hamiltonian of the system determines the sequence of phase space points $(q_\nu(t), p_\nu(t))$, the phase space trajectory. Hence, $H(q_\nu(t), p_\nu(t))$ describes the temporal evolution of the system. For a closed system with constant particle number N , volume V , and total energy E as well as a Hamiltonian H with no explicit time dependency, the possible trajectories always correspond to the same energy E . Thus, the particle system passes through different phase points which all belong to the same hypersurface $\sigma(N, V, E)$ in the phase space. For instance, the harmonic oscillator has the hypersurface in form of an ellipse in two-dimensional phase space. The hypersurface is proportional to the possible number of microstates $\Omega(N, V, E)$ and can be written down as an integral over the phase space,

$$\Omega(N, V, E) = \frac{\sigma(N, V, E)}{\sigma_0} = \frac{1}{N!h^{3N}} \int_V d^{3N}q \int_{-\infty}^{+\infty} d^{3N}p \delta(H(q_\nu, p_\nu) - E). \quad (2.8)$$

σ_0 is considered as the unit surface element occupied by a microstate. However, that statement is somewhat problematic, since classic phase space is continuous and the microstates are infinitely dense packed. Nevertheless, the consideration of the uncertainty relation $\Delta q \Delta p \geq h$ for every component ν makes it possible to discretize the phase space, as quantum mechanically the microstates cannot be packed arbitrarily without contradicting the uncertainty relation. Thus, all microstates (q_ν, p_ν) occupy at least the volume h^{3N} . The additional factor $N!$ is necessary if the particles are indistinguishable, which is identical to the condition that the Hamiltonian does not depend on the explicit order of coordinates (q_ν, p_ν) .

With the above considerations in mind, one can give a definition of a so-called ensemble: a collection of microstates on a hypersurface defined by macroscopic properties. In case of a microcanonical ensemble, the macroscopic properties are number of particles, volume, and total energy, hence an NVE ensemble. A different example is the canonical ensemble with a constant temperature T instead of the total energy E .

Ensembles have certain characteristics and properties. In the following some of which will be shortly stated for the microcanonical ensemble. The number of states Ω of the NVE ensemble is related to the entropy S of the system by the expression $S = k_B \ln \Omega$. Further, if two microcanonical systems are in direct contact – while keeping the number of particles and volume for each system fixed – they will exchange a net energy until the entropy is maximized. The two systems are then in equilibrium and have the same temperature. This fact is captured by the thermodynamic definition of temperature

$$\left. \frac{\partial S}{\partial E} \right|_{N,V} = \frac{1}{T}. \quad (2.9)$$

The most important characteristic of a microcanonical system is the basic postulate of statistical mechanics. The probability of an NVE system to be in a certain microstate is the same for every microstate. Or in other words, each microstate of a constant energy hypersurface is equally likely.

With that last property of an ensemble – the probability of a microstate – the earlier mentioned connection between microstates and macrostates is made. Macroscopic quantities are the mean values of weighted microscopic quantities,

$$\langle A \rangle_{\text{ensemble}} = \sum_{\substack{\text{micro} \\ \text{states } i}} \rho_i^{\text{ensemble}} A_i, \quad (2.10)$$

the weight being the probability of a microstate. (2.10) describes the so-called ensemble average of a microscopic observable A_i , for convenience, in discrete notation.⁶

The probability ρ_i^{mc} for the microcanonical ensemble is simply the inverse of the number of states Ω , since it is – in terms of statistics – the frequency of an event divided by the total number of events,

$$\rho_i^{mc} = \begin{cases} \frac{1}{\Omega} & E = H(q_\nu, p_\nu), \\ 0 & \text{otherwise.} \end{cases} \quad (2.11)$$

The probability for the canonical ensemble is proportional to the well-known Boltzmann factor $e^{-E_i/(k_B T)}$. It is derived when considering the probability of a microstate with energy E_i represented by a small system in a large heat reservoir with temperature T . The canonical partition function Z ensures normalization of the probabilities,

$$\rho_i^c = \frac{1}{Z} e^{-E_i/(k_B T)} \quad \text{with } Z = \sum_{\substack{\text{micro} \\ \text{states } i}} e^{-E_i/(k_B T)}. \quad (2.12)$$

There is a direct connection between ρ_i^c and ρ_i^{mc} as Z can be expressed with the help of the number of states Ω by summing up over all constant energy states,

$$Z = \sum_{E_i} \Omega(N, V, E_i) e^{-E_i/(k_B T)}. \quad (2.13)$$

Assuming only one energy state E_i , the expression for ρ_i^c reduces to ρ_i^{mc} . Then, ρ_i^c is indeed the probability of having a microstate of energy E_i . However, in a microcanonical ensemble the value is identical for every microstate. (2.13) shall conclude the brief overview of statistical mechanics.

With this proper background the original starting point of the section – the somewhat problematic long-term behavior of MD – is reconsidered. The numeric integration of Newton's equation of motion is achieved with so-called step-by-step integrators. Without getting into much detail here (see Section 2.1.3), each step

⁶ For continuous notation: $i \rightarrow (q_\nu, p_\nu)$, $\sum_i \rightarrow 1/h^{3N} \int d^{3N}q d^{3N}p$ including the factor $(N!)^{-1}$ if particles are indistinguishable.

introduces a local error in order of the time step $O(\Delta t^p)$, since the trajectories are approximated. By choosing small time steps the local error is relatively low. However, the local errors sum up to a global error, which depends exponentially on the difference between exact and approximated trajectories times the order of the local error. This can be demonstrated by the Lyapunov instability, also known as the “butterfly effect” [28, 30]. Comparing two MD simulations with nearly identical initial conditions shows an exponential divergence of initially close trajectories. Consequently, MD cannot predict the true trajectories of a classical system in the long run. Even if the real initial conditions were exactly known, the trajectories will diverge significantly at some point. That raises the valid question why MD should be applied at all.

The answer is given by statistical considerations in the context of ensemble theory, where symplecticity – a property of the used integrator – plays an important role. A symplectic integrator conserves the volume in phase space. As a consequence, the numerically computed trajectories $(q_\nu(t), p_\nu(t))$ – solutions of the Hamiltonian of the system – stay on the same hypersurface in phase space. The integrator never leaves the ensemble. However, since it is an approximation, the hypersurface deviates from the exact hypersurface. It can be shown that the approximated hypersurface belongs to a so-called shadow Hamiltonian: a Hamiltonian perturbed in the order of the time step which transfers to the true Hamiltonian in the limit of small time steps. As the calculated trajectories solve the shadow Hamiltonian exactly, conserved quantities of the Hamiltonian – like the total energy – are conserved on those trajectories. Thus, throughout the simulation an approximated value of the total energy is conserved and no drift in total energy is observed. The same holds for other ensemble averages [28, 31]. Hence, in question of statistical averages, MD is indeed a valid tool despite the divergence of the trajectories.

But even the divergence of trajectories is not as problematic as one might think and should be considered from another point of view. Although the trajectories are sensitive to the initial condition and slowly diverge from the exact temporal evolution, they stay in the same ensemble or – to be more precise – in a shadow ensemble close to the exact one. The phase space is accessed on different routes over time, but in the long run they will explore the same part of the phase space. This whole aspect can be interpreted physically as a slight disturbance within the experimental setup, like thermal fluctuations. Furthermore, as the initial conditions are unknown, the divergence of trajectories is even advantageous. The system will evolve into the correct hypersurface, regardless from where exactly the simulation started. The longer the simulation runs, the more the system loses its initial state. This loss of memory to the initial state is desirable, since the initial conditions are artificially imposed and – by losing them – the system ends up in a natural state in equilibrium. Another thought is to look at the divergence from exact trajectories not as a result of numerical approximations but rather as a result of different initial conditions (further reading in [28, 32, 33]). From that perspective the concerning numerical long-term behavior loses its weight.

To conclude the purpose of this section, the ergodic hypothesis has to be introduced. In a nutshell symplecticity ensures the correct ensemble averages in an

```

init(R,V)      !initialization
do while (t<tmax)
  force(R,F)      !determine the forces
  integrate(R,V,F) !integrate equations of motion
  t = t + delt
  sample()        !sample averages
end do

```

Listing 2.1. Fundamental structure of a simple MD program in pseudo code [33]

MD simulation. Ergodicity on the other hand, offers a strategy to actually calculate those ensemble averages. It connects (2.10) – the formula for ensemble averages of an observable – with the time average of that observable,

$$\langle A \rangle_{\text{ensemble}} = \frac{1}{\tau} \int_{t_0}^{t_0+\tau} A_{\text{ensemble}}(q_\nu(t), p_\nu(t)) dt. \quad (2.14)$$

The relation is fulfilled, if – in the limit of $\tau \rightarrow \infty$ – the ensemble average is independent of the initial coordinate $(q_\nu(t_0), p_\nu(t_0))$ at time t_0 . An additional requirement is that the trajectories explore the whole hypersurface of the ensemble in phase space for $\tau \rightarrow \infty$ [28, 29]. Consequently, an MD simulation has to run sufficiently long, especially to reach nearly every phase point of the ensemble for a proper statistical distribution. Notice, according to (2.14) the explicit knowledge of the probabilities ρ^{ensemble} is not necessary. It just has to be guaranteed that the MD simulation produces the correct ensemble.

Fundamental Structure of a Simple MD Program. At the beginning of this chapter, the basic procedure of an MD loop has been already mentioned. In the following an implementation of such a loop will be presented.⁷ Listing 2.1 displays the fundamental structure of a simple MD program whose elements are presented shortly. The `force` and `integrate` routine are discussed in more details in Section 2.1.2, *Effective Potentials*, and Section 2.1.3, *Integration Schemes and Thermostats*.

init(R,V)

Before starting the actual time evolution of the many-body system, it needs to be initialized first. The positions $\mathbf{R} = \{\vec{r}_i\}$ and velocities $\mathbf{V} = \{\vec{v}_i\}$ of the particles have to be set.⁸ Whereas the positions depend directly on the particular physical problem at hand and can be specified accordingly, the velocities are not known per se and therefore have to be generated randomly as well as scaled afterwards to the

⁷ largely based on [33]

⁸ The notation of the nuclei or atoms positions changes here from the capitalized symbols to uncapitalized ones. The notation is not to be confused with the notation for electron coordinates in the paragraph about quantum mechanical foundations of MD.

starting temperature T_0 . The equipartition theorem of thermodynamics,

$$\langle E_{\text{kin}} \rangle = \frac{N_f}{2} k_B T, \quad (2.15)$$

makes it possible to define the so-called instantaneous temperature $T(t)$ by replacing the mean kinetic energy with the current kinetic energy, resulting in

$$k_B T(t) = \frac{2}{N_f} E_{\text{kin}} = \frac{1}{N_f} \sum_{i=1}^N m_i \vec{v}_i(t)^2. \quad (2.16)$$

In thermal equilibrium $T(t)$ fluctuates around the actual temperature T of the system. N_f is usually assumed as $3N$, the number of degrees of freedom of an N particle many-body system in three dimensions. This, however, is strictly speaking not exact. Due to momentum conservation the effective degrees of freedom are reduced by three. Nevertheless, the particle number is mostly big enough in order for the approximation $3N - 3 \approx 3N$ to hold. If periodic boundaries are turned off (free boundaries), the number N_f is reduced even more, because in this case angular momentum is conserved as well. When simulating molecules, the treatment of degrees of freedom has to be done more carefully. Some degrees of freedom are not active, hence, “frozen” at low temperatures, since the molecules can have stiff bonds which “break” only at higher temperature. Only then, the corresponding degrees of freedom can be accessed.

In order to scale the velocities to the starting temperature T_0 , they are multiplied with a scaling factor of

$$\lambda = (T_0/T(t))^{1/2}, \quad (2.17)$$

according to the rule $v_i \rightarrow \lambda v_i$.

force(\mathbf{R}, \mathbf{F})

After initializing positions and velocities, the actual MD loop starts by executing the computationally most expensive routine. From the positions $\mathbf{R} = \{\vec{r}_i\}$ the forces $\mathbf{F} = \{\vec{F}_i\}$ on each atom as well as the potential energy of the system are calculated using the effective potentials. To reduce computational effort, those potentials have certain cutoff radii in order to limit the atomic interaction ranges. In general, at every time step the routine has to loop over all atoms to determine the neighboring atoms lying in the interaction range of one atom. This is avoided by using so-called neighbor lists. A complete loop is only done after a predefined number of time steps to update those lists. The force routine also contains the implementation of periodic boundaries, since the interaction with particles from periodic boxes has to be considered.

integrate(R,V,F)

The integrate routine updates the position $\mathbf{R} = \{\vec{r}_i\}$ and velocities $\mathbf{V} = \{\vec{v}_i\}$ from the previously calculated forces $\mathbf{F} = \{\vec{F}_i\}$. As mentioned in the beginning of this section, this is achieved with a step-by-step integrator, which has a local error of the order of the time step $O(\Delta t^p)$. Due to this local error, the size of the time step has to be sufficiently small, resulting in the general limitation of the timescale in MD. The convergence of the algorithm cannot be ensured for certain choices of the time step size. The estimate

$$\frac{\Delta t}{t_{\text{unit}}} = 0.1 \dots 0.001 \quad (2.18)$$

gives an upper limit for the time step [27]. t_{unit} is the time unit of the applied system of units. The calculation within SI units is avoided for numerical reasons. Instead, the chosen units have magnitudes according to the ones of the system. Specifying a unit for energy, mass, and length ($E_0/m_0/L_0$) defines a complete system of units. A measure of energy divided by mass gives a measure of velocity squared. Building the inverse, taking the square root, and multiplying the result with the measure of length gives a measure of time [33], hence

$$t_{\text{unit}} = L_0 \sqrt{\frac{m_0}{E_0}}. \quad (2.19)$$

With this formula t_{unit} is equal to 1.018×10^{-14} s for a system of units with $E_0 = 1$ eV / $m_0 = 1$ u / $L_0 = 1$ Å. Thus, in order to satisfy (2.18), a time step of $\Delta t = 1$ fs is appropriate. A high temperature is also problematic, since two atoms can get too close to each other in the duration of a time step. In case of $k_B T \gg E_{\text{unit}}$, the estimate (2.18) is adapted in such a way that t_{unit} is replaced by

$$\tau = \frac{L_0}{\bar{v}_{\text{therm}}} = \sqrt{\frac{m_0}{k_B T}} L_0, \quad (2.20)$$

where the atom velocities are described with the mean thermal velocity $\bar{v}_{\text{therm}} \propto \sqrt{k_B T / m_0}$. However, only for very high temperatures like $T = 11\,606$ K, the corresponding energy $k_B T$ is equal to the chosen unit of energy $E_0 = 1$ eV. Next to those two conditions, the time step Δt should be smaller than the inverse of the highest frequency of the system (Debye frequency in case of solids). This is important for simulations including molecules, since molecular vibrations with very high frequencies can occur [27].

sample()

After incrementing the time step, the storage of the ensemble quantities is executed at the end of the MD loop inside the sample routine. Instantaneous temperature as

well as kinetic, potential, and total energy belong to that group. With the help of the virial theorem the instantaneous pressure

$$P(t) = \frac{1}{3V} \left(\sum_{i=1}^N m_i \vec{v}_i(t)^2 + \sum_{\substack{i,j=1 \\ i < j}}^N \vec{F}_{ij} \vec{r}_{ij} \right) \quad (2.21)$$

is also calculated in this routine [28].

2.1.2 Effective Potentials

As mentioned in Section 2.1.1, effective potentials are used to approximate the global potential hypersurface produced by the electronic ground state $\varepsilon_0(\mathbf{R})$. Since the electrons are left out explicitly, one has to be careful in cases where electrons play a key role in interactions or effects which are important in simulations, like chemical reactions. Those effects have to be included in the fitting database of the force-matched potential. But most importantly, the model has to be able to capture them as well.

The approximation is carried out by an expansion of many-body potentials depending on the atom positions $\mathbf{R} = \{\vec{r}_i\}$,

$$\varepsilon_0(\mathbf{R}) = V_{\text{eff}}(\mathbf{R}) = \sum_{i=1}^N \phi(\vec{r}_i) + \sum_{\substack{i,j=1 \\ i < j}}^N \phi(\vec{r}_i, \vec{r}_j) + \sum_{\substack{i,j,k=1 \\ i < j < k}}^N \phi(\vec{r}_i, \vec{r}_j, \vec{r}_k) + \dots \quad (2.22)$$

The first term describes an external potential and is therefore not important for the interaction of the atoms among each other. These interactions are captured by the second and higher order terms. The higher order terms are quite expensive to calculate. Hence, the expansion usually stops at the second term. By assuming isotropic potentials, the models become simple pair potentials with different pair functions for each element pair interaction. Truncating the expansion after the second term is in some cases not sufficient, since many-body effects are neglected. There are various models which overcome the shortcomings of pair potentials. Such models are proposed for different types of interaction and binding types. The Embedded Atom Method (EAM) is a potential model proposed for metals. For that reason it has been chosen as the potential model to describe the ferromagnetic metal compound MnAs and the metal gold.

The Embedded Atom Method. The EAM model⁹ has first been introduced by Daw and Baskes [36] for the simulation of metals. Since then, it has become the standard potential for MD simulation of metals [28].

⁹ also known as Glue Model – an equivalent model of Ercolessi et al. [34] – or Finnis-Sinclair potential by Finnis et al. [35].

Within this model the potential energy of one atom does not depend linearly on the neighborhood or coordination of that atom. This is in contrast to pair potentials. For pair potentials the relation is linear, since the pair energy of an atom and one of its neighbors is added to the total potential energy of the one atom independent of other neighboring atoms. In case of the EAM model, however, each atom is treated effectively as an impurity atom, which is embedded in the environment of the other atoms. The energy – which the embedded atom gains – depends on the density of the surrounding atoms. In this way, the model considers many-body effects and ensures a non-linear dependence on the atom coordination. Daw and Baskes originally identified the density of the atoms as the local electron density of the atoms. For this reason, the derivation of EAM in their publication is based on the density functional theory. However, due to gauge degrees of freedom, one should not attribute a physical meaning to the density. Hence, in the following the density will be only referred to as the transfer density.

The complete model consists of a standard pair term – accounting for repulsive forces – and an embedding term,

$$\begin{aligned}
 V_{\text{EAM}} &= \sum_{\substack{i,j=1 \\ i < j}}^N \phi_{ij}^{\text{pair}}(r_{ij}) + \sum_{i=1}^N U_i^{\text{emb}}(n_i), \\
 n_i &= \sum_{\substack{j=1 \\ j \neq i}}^N \rho_j^{\text{host}}(r_{ij}).
 \end{aligned} \tag{2.23}$$

The transfer density n_i is the sum of the so-called transfer functions $\rho_i^{\text{host}}(r_{ij})$. Those functions depend on the type of the surrounding atoms or host atoms. The type of embedding function is determined by the atom which is embedded within the host atoms. The force component F_i^α acting on the i th atom is calculated by

$$\begin{aligned}
 F_i^\alpha &= -\frac{\partial}{\partial x_i^\alpha} V_{\text{eff}}(R), \\
 &= -\sum_{\substack{j=1 \\ j \neq i}}^N \left(\frac{\partial \phi_{ij}(r_{ij})}{\partial r_{ij}} \frac{x_i^\alpha - x_j^\alpha}{r_{ij}} + \frac{\partial U_i(n_i)}{\partial n_i} \frac{\partial \rho_j(r_{ij})}{\partial r_{ij}} + \frac{\partial U_j(n_j)}{\partial n_j} \frac{\partial \rho_i(r_{ij})}{\partial r_{ij}} \right) \frac{x_i^\alpha - x_j^\alpha}{r_{ij}}.
 \end{aligned} \tag{2.24}$$

As already mentioned, the EAM model has several gauge degrees of freedom. According to [37, 38] there exist the following transformation rules

$$\begin{aligned}
 \phi_{ij}(R) &\rightarrow \phi_{ij}(R) + \lambda_i \rho_j(R) + \lambda_j \rho_i(R), \\
 U_i(n_i) &\rightarrow U_i(n_i) - \lambda_i n_i \quad \lambda_i, \lambda_j \in \mathbb{R} \text{ for each atom type,}
 \end{aligned} \tag{2.25}$$

as well as the two invariances

$$\begin{aligned}
 \rho(R) &\rightarrow \kappa \rho(R), \\
 U(n) &\rightarrow U\left(\frac{n}{\kappa}\right).
 \end{aligned} \tag{2.26}$$

As the transformation rule (2.25) shows, all linear contribution of the transfer density n_i to the potential energy can be moved completely to the pair functions. This confirms that the embedding term introduces the coordination-dependent interaction. It also shows that the embedding function has to be non-linear. Otherwise, the corresponding EAM model could be replaced by an equivalent model of pair functions.

Those gauge degrees of freedom have to be fixed in order to get a unique effective potential, which is especially necessary when the model is used to fit it to reference data. The fitting cannot be successful if there are – in the context of the optimization – unnecessary degrees of freedom.

The fixing of the gauge degrees of freedom in (2.25) can be done by setting the gradient of the embedding function at an arbitrary density to zero ($U'(n_{\text{arb}}) = 0$). Thus, the n_{typ} transformation constants λ_i are defined, meaning, all the gauge degrees of freedom of (2.25) are fixed. Either directly enforcing the transformation rules with the λ_i or indirectly assuring the particular gradient gets adjusted to zero, both ways will apply a certain gauge. The degree of freedom in (2.26) is applied by restraining the domain of the embedding function to a distinct interval. That way the scaling factor κ is fixed. This can also be achieved by fixing the transfer function for a particular distance to an arbitrary value ($\rho(r_{\text{arb}}) = \rho_{\text{arb}}$).

2.1.3 Integration Schemes and Thermostats

The integration of Newton’s equations of motion is closely connected to thermostats and their implementations. The integrator used in this work – embedded in the MD software package LAMMPS – produces an *NVE* ensemble. By modifying directly the integrator, a temperature controlled *NVT* ensemble can be achieved, meaning, a thermostat can be implemented. The section first presents the derivation of this so-called Velocity-Störmer-Verlet integrator and concludes with a short rendition about the applied thermostats.¹⁰

Störmer-Verlet Method. The Verlet algorithm [39] – based on the integration method of Störmer [40] – is directly derived from the Taylor series of the position $\vec{r}(t)$, expanded at the time $t_n \pm \Delta t$ about the point t_n . The index n denotes the time discretization of the problem. The simulation duration is divided into $k + 1$ fixed time steps $t_n = n\Delta t + t_{\text{start}}$ ranging from t_{start} to t_{end} . In particular, there is $t_n + \Delta t = t_{n+1}$. Thus, for each i th atom one gets

$$\vec{r}_i(t_{n\pm 1}) = \vec{r}_i(t_n) \pm \vec{v}_i(t_n)\Delta t + \frac{\vec{F}_i(t_n)}{2m_i}\Delta t^2 \pm \frac{d^3\vec{r}(t_n)}{dt^3}\frac{\Delta t^3}{3!} + O(\Delta t^4). \quad (2.27)$$

In this Taylor expansion, Newton’s equations of motion (2.6) have been already used to replace the second derivative of the position \vec{r} . Summing up both terms in

¹⁰The following mathematical derivations are mostly based on [28].

(2.27) and solving for $\vec{r}_i(t_{n+1})$ yields

$$\vec{r}_i(t_{n+1}) = 2\vec{r}_i(t_n) - \vec{r}_i(t_{n-1}) + \frac{\vec{F}_i(t_n)}{m_i}\Delta t^2 + O(\Delta t^4), \quad (2.28)$$

which is the Störmer-Verlet method for \vec{r} . In order to calculate the new position $\vec{r}_i(t_{n+1})$, one needs to know the positions of the previous times t_n and t_{n-1} . However, the velocities are only implicitly given. By taking the difference of (2.27),

$$\vec{r}_i(t_{n+1}) - \vec{r}_i(t_{n-1}) = 2\vec{v}_i(t_n)\Delta t + O(\Delta t^3), \quad (2.29)$$

an expression for the velocity is derived,

$$\vec{v}_i(t_n) = \frac{\vec{r}_i(t_{n+1}) - \vec{r}_i(t_{n-1})}{2\Delta t} + O(\Delta t^2). \quad (2.30)$$

A direct control over the velocities – for example, needed for rescaling the velocities in order to adjust the temperature – is achieved by the equivalent Velocity-Störmer-Verlet method [41].

The velocity enters the algorithm by using (2.30). Replacing the term $-\vec{r}_i(t_{n-1})$ in the Störmer-Verlet method (2.28) with the help of (2.29) and transforming it to $\vec{r}_i(t_{n+1})$ gives

$$\vec{r}_i(t_{n+1}) = \vec{r}_i(t_n) + \vec{v}_i(t_n)\Delta t + \frac{\vec{F}_i(t_n)}{2m_i}\Delta t^2 + O(\Delta t^3). \quad (2.31)$$

Further, using (2.28) also in (2.30) leads to

$$\vec{v}_i(t_n) = \frac{\vec{r}_i(t_{n+1}) - \vec{r}_i(t_{n-1})}{2\Delta t} = \frac{\vec{r}_i(t_n) - \vec{r}_i(t_{n-1})}{\Delta t} + \frac{\vec{F}_i(t_n)}{2m_i}\Delta t + O(\Delta t^2). \quad (2.32)$$

Adding the same expression for $\vec{v}_i(t_{n+1})$, one gets

$$\vec{v}_i(t_n) + \vec{v}_i(t_{n+1}) = \frac{\vec{r}_i(t_{n+1}) - \vec{r}_i(t_{n-1})}{\Delta t} + \frac{\vec{F}_i(t_{n+1}) + \vec{F}_i(t_n)}{2m_i}\Delta t + O(\Delta t^2). \quad (2.33)$$

Finally, inserting (2.30) and solving for $\vec{v}_i(t_{n+1})$ results in an expression for the velocity at the new time step t_{n+1}

$$\vec{v}_i(t_{n+1}) = \vec{v}_i(t_n) + \frac{\vec{F}_i(t_{n+1}) + \vec{F}_i(t_n)}{2m_i}\Delta t + O(\Delta t^2). \quad (2.34)$$

Both equations – (2.31) and (2.34) – constitute the Velocity-Störmer-Verlet method. Because the forces have to be known at two times (t_n and t_{n+1}), the implementation is different to the previous one of the basic MD program in Listing 2.1. The calculation of the velocity is split into two parts, one with the “old” and one with the “new” forces. Listing 2.2 shows the changed pseudo code of the MD program.

```

init(R,V)  !initialization
force(R,F) !determine forces before MD loop
do while (t<tmax)
  integrate1(R,V,F) !first step velocity verlet
  force(R,F)         !determine new forces
  integrate2(R,V,F) !second step velocity verlet
  t = t + delt
  sample() !sample averages
end do

```

Listing 2.2. Velocity-Störmer-Verlet MD program in pseudo code [33]

The choice for the Störmer-Verlet method as MD integrator is founded on several advantages. It is easy to implement, it is direct instead of implicit, and it offers the explicit control over the velocities. Next to that, the MD integrator is time-reversible and symplectic. As discussed in Section 2.1.1, especially the last property is very important concerning the long-time stability of an MD integrator.

Thermostats through Friction. A thermostat has to supply or withdraw energy to a many-body particle system via a heat current J_Q in order to control the temperature of that system. In experiments, thermostats are realized by coupling the regarded system to a much bigger system – the heat reservoir – with the desired temperature T_D . Due to heat exchange, the temperature of both systems gets equalized. Since the second system is significantly bigger than the first, small one, this temperature is nearly equal to the desired temperature T_D . The duration for this equilibration depends on the strength of the coupling to the heat reservoir.

In MD such a coupling to a heat reservoir can be implemented by introducing a friction term into the equation of motions (2.6),

$$m_i \frac{d\vec{v}_i}{dt} = \vec{F}_i - \kappa m_i \vec{v}_i, \quad i = 1, \dots, N. \quad (2.35)$$

By rearranging the time discretized version of the above equation,

$$m_i \frac{\vec{v}_i(t_{n+1}) - \vec{v}_i(t_n)}{\Delta t} = \vec{F}_i(t_n) - \kappa(t_n) m_i \vec{v}_i(t_n), \quad (2.36)$$

for $\vec{v}_i(t_{n+1})$, one gets

$$\begin{aligned} \vec{v}_i(t_{n+1}) &= \vec{v}_i(t_n) + \Delta t \frac{\vec{F}_i(t_n)}{m_i} - \Delta t \kappa(t_n) \vec{v}_i(t_n), \\ &= (1 - \Delta t \kappa(t_n)) \vec{v}_i(t_n) + \Delta t \frac{\vec{F}_i(t_n)}{m_i}. \end{aligned} \quad (2.37)$$

(2.37) shows how the friction term influences the velocity. For the n -th simulation step, the velocities are effectively scaled by a factor. Velocity scaling has been already

introduced earlier to initialize the velocities at the beginning of a simulation. The relation of this scaling factor λ to the coupling factor κ is

$$\lambda = (1 - \Delta t \kappa(t_n)), \quad (2.38)$$

or

$$\kappa(t_n) = (1 - \lambda) / \Delta t. \quad (2.39)$$

Inserting the expression for the force of (2.35) into the equations of the Velocity-Störmer-Verlet algorithm, one obtains an adapted version of this integrator scheme, where additional friction terms are included. By performing that extended algorithm scheme, a thermostat can be successfully applied in an MD simulation. Different definitions of the coupling κ result in different types of thermostats.

Berendsen Thermostat. The thermostat after Berendsen [42] is based on the assumption that the heat current J_Q depends linearly on the temperature difference of the system and heat reservoir,

$$J_Q = \frac{\Delta Q}{\Delta t} = \alpha (T_D - T(t)). \quad (2.40)$$

The heat quantity ΔQ – added or removed from the system – is the difference in kinetic energy. By using the scaling factor λ and $\beta = N_f k_B / 2$, it has the form

$$\Delta Q = \Delta E_{\text{kin}} = \sum_{i=1}^N \frac{m_i}{2} \vec{v}_i(t)^2 (\lambda^2 - 1) = \beta T(t) (\lambda^2 - 1). \quad (2.41)$$

Combining (2.40) and (2.41) yields

$$\begin{aligned} \lambda^2 &= 1 + \frac{T_D - T(t)}{T(t)} \frac{\alpha}{\beta} \Delta t, \\ &= 1 + \left(\frac{T_D}{T(t)} - 1 \right) \gamma \Delta t, \quad \gamma = \frac{\alpha}{\beta}. \end{aligned} \quad (2.42)$$

The dampening parameter γ defines the strength of the coupling. With $\gamma = 1/\Delta t$, eq. (2.42) reduces to $\lambda^2 = T_D/T(t)$, also known as the constraint method. The correction to the desired temperature is executed instantly, which is the same for the velocity initialization. A value of γ within the interval $[0, 1/\Delta t]$ adapts the current temperature exponentially to T_D , as proven by the equation

$$\frac{\Delta T}{\Delta t} = \frac{\alpha}{\beta} (T_D - T(t)), \quad (2.43)$$

which is obtained when dividing (2.40) with β .

A direct expression for the coupling κ can also be derived [27]. Approximating the root in the following expression with a Taylor expansion and using the relation (2.38), one gets

$$\begin{aligned}\lambda &= \sqrt{1 + \frac{T_D - T(t)}{T(t)} \gamma \Delta t}, \\ &\approx 1 + \frac{1}{2} \left(\frac{T_D}{T(t)} - 1 \right) \gamma \Delta t, \\ &= 1 - \kappa(t) \Delta t, \\ \Leftrightarrow \kappa(t) &\approx \frac{\gamma}{2} \left(1 - \frac{T_D}{T(t)} \right).\end{aligned}\tag{2.44}$$

The Berendsen thermostat is easy to implement, since it can be realized by a simple scaling of the velocities. Hence, the introduction of the friction term is not mandatory. The disadvantage is – although the ensemble of a system in a heat reservoir is by definition a canonical ensemble – the Berendsen thermostat does not produce an exact canonical ensemble. However, it can be used to get a particle system to a certain temperature. For a true canonical ensemble, the Nosè-Hoover thermostat has to be applied.

Nosè-Hoover Thermostat. This thermostat was proposed by Hoover [43], who modified the so-called extended system method of Nosè [44]. The basic idea is to consider the heat bath as an additional degree of freedom, which also determines the coupling of the particle system to the heat bath. The time behavior of the coupling factor $\kappa(t)$ is described by the ordinary differential equation¹¹

$$\frac{d\kappa}{dt} = \frac{1}{M} \left(\sum_{i=1}^N m_i \vec{v}_i^2 - N_i k_B T_D \right).\tag{2.45}$$

There are several ways to implement the integration of this differential equation [27, 28], but they all have in common that $\kappa(t)$ is integrated in a similar way like the equations of motion. The dampening factor M is a free parameter, which has to be determined beforehand to get the appropriate strength for the coupling.

Langevin Thermostat. The Langevin thermostat has been proposed to simulate solvent atoms or molecules, without explicitly simulating the solvent. The idea behind it is that the solved particles randomly bump into the not existing particles of the solvent or the heat bath. For that reason a stochastic noise term $\vec{S}(t)$ is added next to the standard friction term of (2.35),

$$m_i \vec{v}_i = \vec{F}_i - \kappa m_i \vec{v}_i + \vec{S}_i(t).\tag{2.46}$$

The exact background of the thermostat is described in [46]. The thermostat can be used beyond the original purpose. Like the Berendsen thermostat, it is suited to get the system efficiently to a desired temperature. In the used MD software LAMMPS, the implementation is equal to Brownian dynamics [47].

¹¹Details on the derivation of this equation can be found in [43, 45]

2.2 Force Matching

This section is intended to convey the basic concepts of Force Matching (FM): the fitting of a potential model to *ab initio* data. Those basics of FM include in principle the quantum mechanical basics of solving the electronic Schrödinger equation (2.3), since the calculation of forces and energies from that equation is crucial for FM. However, details on how (2.3) is solved explicitly is omitted at this point. The reader is referred to basic literature on the topic, for example found in here [26].

The section is split into two parts. Apart from a short description of the basics of FM, the implementation of FM within the software package *potfit* is presented.

2.2.1 FM Basics

The concept of FM was proposed and tested by Ercolessi and Adams in 1988, based on the example of generating a glue potential for aluminum [48]. In this concept the main task is optimizing the so-called target function¹²

$$Z(\boldsymbol{\alpha}) = Z_{\text{R}}(\boldsymbol{\alpha}) + Z_{\text{C}}(\boldsymbol{\alpha}), \quad (2.47)$$

with

$$Z_{\text{R}}(\boldsymbol{\alpha}) = \sum_{k=1}^{N_{\text{R}}} u_k \left(F_k(\boldsymbol{\alpha}) - F_k^0 \right)^2, \quad (2.48)$$

$$Z_{\text{C}}(\boldsymbol{\alpha}) = \sum_{r=1}^{N_{\text{C}}} \omega_r \left(A_r(\boldsymbol{\alpha}) - A_r^0 \right)^2. \quad (2.49)$$

The potential model – depending on the set of parameters $\boldsymbol{\alpha}$ of length n – is fitted to N_{R} reference data values F_k^0 by taking the squared difference to the values $F_k(\boldsymbol{\alpha})$ of the model. The reference values F_k^0 belong to so-called reference configurations – atomic structures the model should describe – and can be the force component of each atom, the energy per atom of each configuration, and the stress tensor of each configuration box. By varying the parameters $\boldsymbol{\alpha}$, the corresponding values $F_k(\boldsymbol{\alpha})$ – calculated from the potential model – have to be adjusted to the reference values. Each configuration can be weighted by the factor u_k . Also, energy and stress reference data have individual weights. The number of force components is significantly larger than the number of energy or stress values, since there is, for example, only one energy per configuration. Hence, those values have to be weighted separately in the target function. The forces are usually weighted by the inverse of the magnitude of the corresponding atomic force vector. In addition to reference data, the target function can also include special constraints, represented by the term Z_{C} . Those constraints get important when the potential model has degrees of freedom which have to be fixed.¹³

¹²notation as in [48, 49].

¹³In *potfit* the constraints are referred to as dummy constraints, which are discussed in Section 3.1.1.

Optimizing the target function Z is nothing else than applying the method of least squares derived by Gauß. The function $f_{\alpha}(x_j)$ – described by n parameters $\alpha = \{\alpha_i\}$ – has to be fitted to known data values y_j , consequently

$$f_{\alpha}(x_j) = y_j, \quad j = 1, \dots, m. \quad (2.50)$$

Such a system of equations is usually overdetermined ($m > n$). Hence, no exact solution exists for those systems. However, minimizing the sum of the squared residuals yields an approximate solution for the requested set of parameters α_i . The proposed target function Z is basically such a sum and with the above definitions one gets

$$Z(\alpha) = \sum_{j=1}^m \omega_j (f_{\alpha}(x_j) - y_j)^2. \quad (2.51)$$

The optimization of Z can be conducted directly in one step if $f(x_j)_{\alpha}$ is a linear polynomial of the form $\sum_{i=1}^n x^{i-1} \alpha_i$.¹⁴ This is not the case for FM. The highly non-linear problem has to be solved with iterative methods. From a starting point α_0 , these methods approximate the minimal solution α_m step by step. The software *potfit* for applying FM uses different iterative methods. The software – including the implemented search algorithms – is presented in the following section.

2.2.2 *potfit*: An Implementation of FM

The program *potfit* uses a deterministic method derived by Powell to minimize (2.51). It is deterministic, since it usually leads always to a minimum. However, the resulting minimum does not necessarily coincide with the global minimum of the configuration space spanned by parameters α_i . Thus, an additional algorithm called Simulated Annealing is implemented, which searches the configuration space stochastically. Due to its stochastic nature, Simulated Annealing cannot get stuck in local minima. But being stochastic also means that the method is very slow. For this reason *potfit* combines both methods.¹⁵ At the beginning of the optimization, Simulated Annealing gets the target function to the attraction regime of the global minimum. After that, the algorithm of Powell provides the final optimization of Z . In Figure 2.1 this basic scheme of *potfit* is shown. The scheme is taken from the doctoral thesis of the first developer of *potfit* Peter Brommer [49], where further details of the program can be found. Here, only the basics of the two mentioned optimization methods are shortly introduced.

¹⁴From there, an equivalent set of normal equations is derived. This is a system of linear equations which can be solved by direct methods like Gaussian elimination.

¹⁵Instead of Simulated Annealing *potfit* also offers an alternative named Differential Evolution. However, since the method has not been applied in this work, it will not be discussed any further.

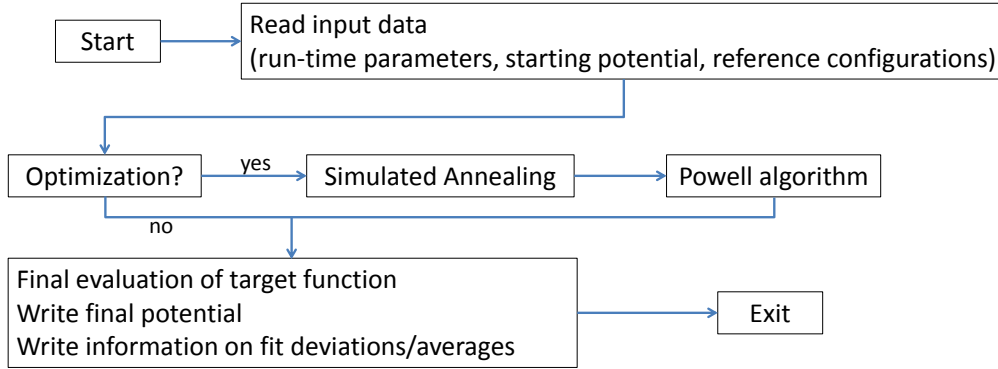


Figure 2.1. Basic working scheme of *potfit* [49]: After reading different input data, the stochastic algorithm Simulated Annealing is executed. This is followed by a run of the deterministic Powell algorithm. In the end the output data is written, including final potential and fitting errors. Those values can be also calculated directly for a given potential by turning off the optimization step, making it easier to compare quickly different potentials.

Simulated Annealing. Proposed by Kirkpatrick et al. [50], Simulated Annealing is based on the Monte Carlo (MC) method [51]. But instead of minimizing the total energy of a many-body system – which is the typical application for MC – the target function $Z(\boldsymbol{\alpha})$ is optimized. In direct analogy to MC, one parameter of the set $\boldsymbol{\alpha}$ is changed randomly. The change $\Delta\boldsymbol{\alpha}$ is accepted if it leads to an improvement of $Z(\boldsymbol{\alpha})$, meaning the value of the target function decreases. If the target function gets worse, the change can still be accepted according to a probability $P(\Delta Z) = \exp(-\Delta Z/T)$, which is the analogue to the Boltzmann factor (compare eq. (2.12)). The artificial temperature T has the units of Z and is only an auxiliary quantity needed for the probability factor. Due to the acceptance of changes where the target functions increases, the algorithm is able to leave the attraction regime of a certain minimum. Again, this is not possible for deterministic algorithms like the one by Powell.

Since the method of Simulated Annealing was originally used for discrete systems, a variable step size has to be introduced for the continuous case to reasonably scan the entire configuration space. For this purpose Corona et al. [52] proposed to change the new parameter set $\boldsymbol{\alpha}'$ with the formula

$$\boldsymbol{\alpha}' = \boldsymbol{\alpha} + rv_h \mathbf{e}_h. \quad (2.52)$$

Every h th coordinate direction of the configurations space has an adaptive step size v_h . The factor r is a random number within the interval $[-1, 1]$ and \mathbf{e}_h is the unit vector of the according coordinate direction. In *potfit* this formula has to be adapted. Changes of a single α_i can lead to overswinging of the interpolating splines, since the α_i are the spline knots of the potential functions. By adding a Gaussian to the sampling point in question, this problem is avoided as the neighboring spline knots are changed as well [49]. The adaptive regulation of the step size is coupled to the acceptance rate. If the acceptance rate is too high, the step size is too small and has to be reduced. If the acceptance rate is too low, the step size has to be increased (details in [52]). With this rule the algorithm begins to scan the configuration space

with a predefined starting temperature. After that, this temperature is successively reduced in defined cycles of iterations, which explains the name Simulated Annealing. Like the annealing of a metal, the algorithm “cools” the system slowly to find the optimum. The repeated reduction of the temperature stops according to two criteria [38]:

1. The values of $Z(\boldsymbol{\alpha})$ of successive temperature cycles do not change within a certain accuracy. The algorithm is therefore located in a minimum.
2. The current value of Z is so far very similar to the previous optimum $Z(\boldsymbol{\alpha}_{\text{opt}})$.

If only the first condition applies, the algorithm is stuck in a local minimum and the algorithm is started again at $\boldsymbol{\alpha}_{\text{opt}}$. If both conditions are true, the algorithm terminates with $\boldsymbol{\alpha}_{\text{opt}}$ as the best value. Starting from a high temperature as well as using a slow cooling increases the probability to find the global minimum. However, those settings also show why this optimization algorithm is very slow in general. Consequently, the accuracy for the stopping criteria is chosen to be relatively big. The algorithm has to find the attraction regime of the global minimum. The final optimization is done by the Powell algorithm.

Powell Algorithm. In numerics there is a typical strategy to find iteratively the minimum of a function depending on various variables \boldsymbol{x} . First, a search direction in the configuration space of the variables is determined according to specific criteria. Beginning from a starting point \boldsymbol{x}_0 , the minimum along that direction is calculated. This concludes one iteration. From the found minimum \boldsymbol{x}_1 the next iterations k start in the same fashion until the \boldsymbol{x}_k remain unchanged within a defined accuracy. The speed of the algorithms strongly depends on the way how directions are chosen. The simplest idea is to take the steepest descent of the function, which is the negative gradient $g = -\nabla Z(\boldsymbol{\alpha})$. However, unlike conjugate gradients¹⁶ those standard gradients discard previous gained search directions towards the minimum, often resulting in a lengthy zigzag search path. Consequently, conjugate gradient methods are the standard iterative search algorithms.

There are different implementation of such conjugate gradient methods. The special form of Z as well as the expensive calculation of its gradients make the algorithm of Powell especially suited for Force Matching and is therefore implemented in *potfit*. In the following a very shortened rendition of the original publication of Powell [53] is given. Details like omitted steps during the derivation or convergence performances of the algorithm can be found there.

Using Powell’s notation, (2.51) can be written as

$$Z(\boldsymbol{\alpha}) = \sum_{k=1}^m \left[f^{(k)}(\boldsymbol{\alpha}) \right]^2. \quad (2.53)$$

¹⁶Exact definition and introduction will be omitted at this point.

Further, the first and second derivations of $f^{(k)}$ are defined by

$$\begin{aligned} g_i^{(k)}(x) &= \frac{\partial}{\partial x_i} f^{(k)}(x), \\ G_{ij}^{(k)}(x) &= \frac{\partial^2}{\partial x_i \partial x_j} f^{(k)}(x). \end{aligned} \quad (2.54)$$

Now, the variable vector $\boldsymbol{\xi}$ shall be the iterative approximation to the actual minimum at $\boldsymbol{\xi} + \boldsymbol{\delta}$. Then, the derivatives in each direction are zero at this point $\boldsymbol{\xi} + \boldsymbol{\delta}$. By applying the chain rule and subsequently dividing with the factor two, one gets

$$\sum_{k=1}^m g_i^{(k)}(\boldsymbol{\xi} + \boldsymbol{\delta}) f^{(k)}(\boldsymbol{\xi} + \boldsymbol{\delta}) = 0, \quad i = 1, \dots, n. \quad (2.55)$$

Taking the Taylor series in $\boldsymbol{\xi}$ about $\boldsymbol{\delta}$ and neglecting the expression $G_{ij}^{(k)}(\boldsymbol{\xi}) f^{(k)}(\boldsymbol{\xi})$ finally leads to

$$\sum_{j=1}^n \left\{ \sum_{k=1}^m g_i^{(k)}(\boldsymbol{\xi}) g_j^{(k)}(\boldsymbol{\xi}) \right\} \delta_j = - \sum_{k=1}^m g_i^{(k)}(\boldsymbol{\xi}) f^{(k)}(\boldsymbol{\xi}), \quad i = 1, \dots, n. \quad (2.56)$$

Solving the linear system of equations in (2.56), gives the correction $\boldsymbol{\delta} = \sum_{i=1}^n \delta_i \mathbf{e}_i$ to the current approximation $\boldsymbol{\xi}$. With that, the minimum can be iteratively calculated via the points $\boldsymbol{\xi}_s = \boldsymbol{\xi}_{s-1} + \lambda_m \boldsymbol{\delta}$, whereby λ_m is determined when minimizing the function $Z(\boldsymbol{\xi} + \lambda \boldsymbol{\delta})$ along the direction $\boldsymbol{\delta}$. As long as $\boldsymbol{\xi}$ does not happen to be a stationary point during the iterations, the convergence of the algorithm is mathematically guaranteed [53].

The disadvantage of this so-called generalized least squares method is the explicit evaluation of the gradients $g_i^{(k)}(\boldsymbol{\xi})$ at every iterative step. Therefore, Powell proposed a method without calculating derivatives, based on the generalized least squares method. This iterative method starts by initializing n linear independent directions $\mathbf{d}(1), \mathbf{d}(2), \dots, \mathbf{d}(n)$, which span the configuration space of the variable $\boldsymbol{\xi}$. Additionally, one defines the estimated derivative of $f^{(k)}$ along the i th direction as

$$\gamma^{(k)}(i) \approx \sum_{j=1}^n g_j^{(k)}(\boldsymbol{\xi}) d_j(i), \quad i = 1, \dots, n, \quad j = 1, \dots, m. \quad (2.57)$$

By taking the coordinate directions as the directions $\mathbf{d}(i)$, the above derivatives are calculated according to a normalized numerical derivative,

$$\gamma^{(k)}(i) = s_i \frac{f^{(k)}(\xi_1, \dots, \xi_{i-1}, \xi_{i+\epsilon_i}, \xi_{i+1}, \dots, \xi_n) - f^{(k)}(\boldsymbol{\xi})}{\epsilon_i}, \quad (2.58)$$

for the first iteration. In the next step, the correction $\boldsymbol{\delta}$ is expressed with the help of the vectors $\mathbf{d}(i)$. Substitution in (2.56) yields

$$\begin{aligned} \sum_{j=1}^n \left\{ \sum_{k=1}^m \gamma^{(k)}(i) \gamma^{(k)}(j) \right\} q(j) &= p(i), \quad i = 1, \dots, n, \\ \text{with } \boldsymbol{\delta} &= \sum_{i=1}^n q(i) \mathbf{d}(i) \text{ and } p(i) = - \sum_{k=1}^m \gamma^{(k)}(i) f^{(k)}(\boldsymbol{\xi}). \end{aligned} \quad (2.59)$$

Like in (2.56) new corrections of $\boldsymbol{\delta}$ can be calculated with the above formula. In order to get an approximation $v^{(k)}(\boldsymbol{\delta})$ for the gradient along the direction of $\boldsymbol{\delta}$, the derivative with respect to λ from minimizing $Z(\boldsymbol{\xi} + \lambda\boldsymbol{\delta})$ ¹⁷ is used. In each iteration one $\gamma^{(k)}(t)$ and one $\boldsymbol{d}(t)$ are substituted by the mentioned gradient approximation $v^{(k)}(\boldsymbol{\delta})$ and the correction $\boldsymbol{\delta}$, respectively, according to special criteria [53]. The substituted directions are also pairwise conjugate to each other [53]. The biggest advantage, however, is the fact that the derivatives of Z only have to be calculated once.

¹⁷In *potfit* this minimization is realized by the algorithm of Brent [54].

3 Generation of Effective Potentials

As mentioned earlier in the introduction, the first step towards tackling the initial question of gold (Au) deposition on MnAs is the generation of an effective potential describing the interactions between the different atomic elements in an MD simulation. This is a necessary step, since no effective potential for the MnAs system or the specific problem of depositing Au atoms on a MnAs surface has been developed in the literature yet.

The chapter is split in two parts. First, general facts and ideas concerning fitting strategies beyond the previous mentioned basics of Force Matching are introduced. Second, details on the generation of the EAM potential for the MnAs/Au interface system are presented, including the resulting potential itself as well as the validation of the latter.

3.1 Fitting Strategies

The generation of an effective potential in the scope of Force Matching is by far a non-trivial optimization problem and it involves more than a simple run of the *potfit* program package. In order to produce a potential with the desired properties for a specific situation, it requires “much skill, work, and intuition” [28]. The main reason behind this statement is that the potential development is not a straightforward process, where one explicit strategy must lead to success. Figure 3.1 shall illustrate that point. When looking at the fitting process in the most general and abstract way – counting everything which can influence the potential as a parameter – it is an iterative optimization cycle with parameters being optimized until a termination condition is reached. From that point of view it should be possible to investigate the optimization systematically in order to find the best set of parameters. However, especially the term “systematically” proves to be problematic in several aspects as the situation is more complex than the above statement suggested. As seen in Figure 3.1, there are parameters of different nature: the potential model and parameters, *potfit* run-time parameters, and the reference configurations. Some of those parameters depend on one another. There are various paths to correct and adapt the potential and its parameters, symbolized by the arrows. And, concerning the termination conditions, the criteria selecting the paths act on different levels.

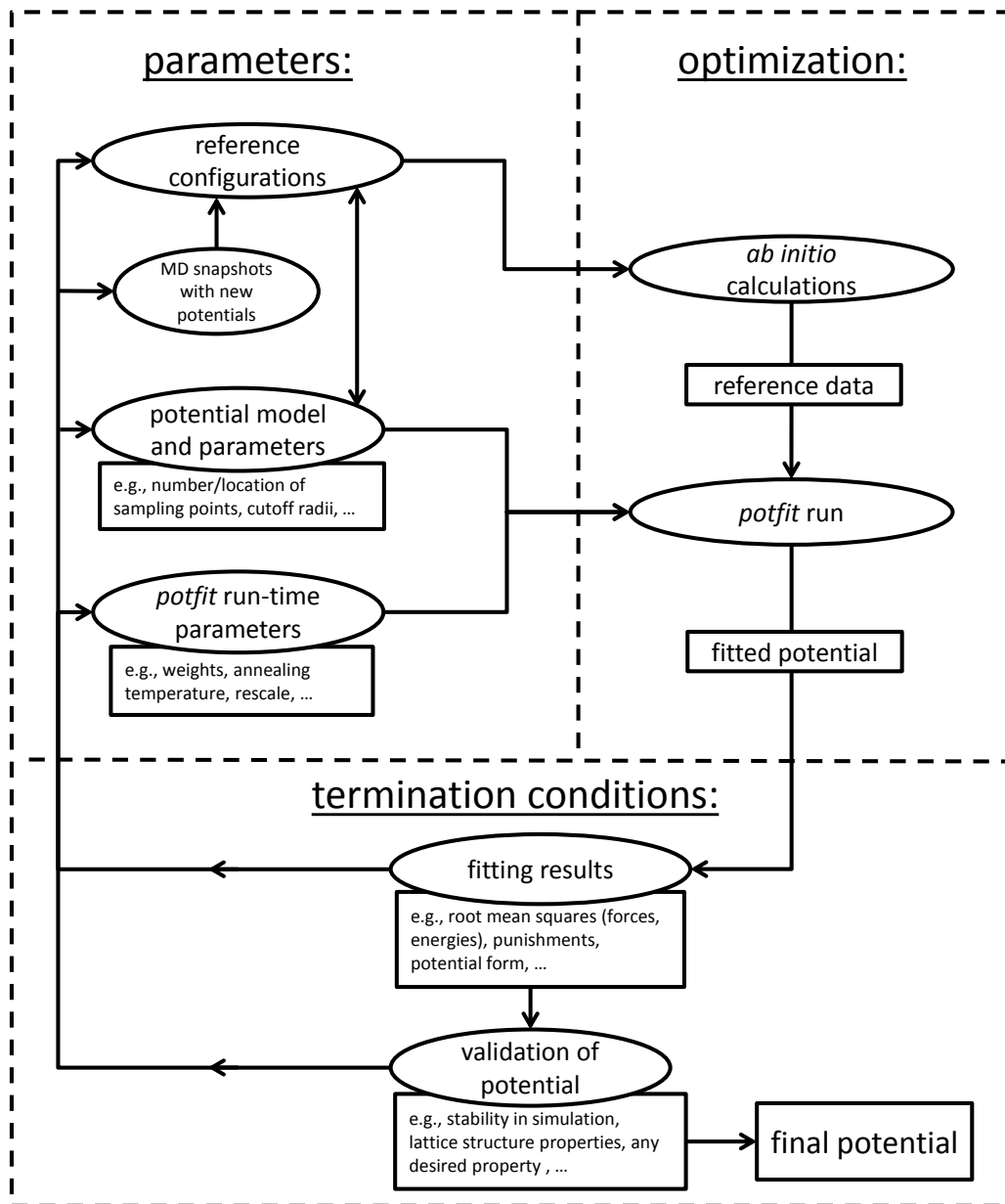


Figure 3.1. Work flow diagram of the general, iterative optimization cycle of a potential generation, considered as a classical optimization loop with termination conditions: The notion “parameters” summarizes all the elements which influence the fitting process of the potential. The arrows depict the different optimization paths and dependencies within the cycle.

The first group of termination conditions are the fitting results, which are available directly after a *potfit* run. Among the fitting results is the root mean square deviation (rms), a measure of the deviation between potential model and reference data. It is therefore a key criterion for the mathematical quality of the fit, but not necessarily an indicator for the physical quality of the potential, since the potential quality strongly depends on the selection of the reference data. The validation of the potential – the important testing of quantities not included in the fit – is the indicator for the quality of the potential. In contrast to the fitting results, the validation of the potential is a post-processing evaluation. Thus, the criteria involved are more of indirect nature. Also, the criteria may have a rather qualitative nature, making it harder to decide which parameter should be changed. In addition, all the stated aspects depend on the physical problem at hand and the individual chosen performance requirements for the potential. Therefore, in summary it is quite difficult to propose a general systematic strategy.

Nevertheless, there are guidelines and rules which should be true in general. For starters, there is some sort of hierarchy within the parameters. A few parameters should be simply set at the beginning, rather than optimized (see Section 3.1.2). That optimization path may be introduced later in the iterative fitting procedure. In accordance with that rule is the fact that there is a typical optimization path in the beginning of every potential generation. After setting up the starting parameters, calculating the *ab initio* reference data, and executing *potfit* the quality of the resulting potential is checked. Either it is obvious from the direct fitting results or more indirectly shown by first validation tests, it will usually be necessary to adapt the parameters of the fitting process. The first thing to consider are the reference configurations, especially when starting from scratch. In that case the reference structures are most certainly unrealistic or, at least, insufficient to represent the desired physical situation. The typical approach to correct for this is producing MD snapshots with the new potential and replace or complement the reference configurations. Then, the optimization process is started again. The cycle can be repeated and offers therefore a general strategy to improve iteratively the reference data and the potential, comparable to a self-consistent mechanism.

However, the optimization and – as the result – the potential can fail despite this strategy and one has to reconsider other parameters and therefore, different optimization paths. The type of failure strongly depends on the physical problem and particular situation. And, as mentioned previously, it is not always directly apparent which of the parameters should be changed.

In the following, a basic set up of a potential generation will be presented by discussing some of the parameters displayed in Figure 3.1. Most of the information can be found in the diploma and doctoral thesis of Peter Brommer [38, 49] and the *potfit* wikipedia [55], as well as further details. At the end, a few general remarks are made trying to summarize some lessons which have been learned from experience.

3.1.1 Basic Setup

Selecting the Reference Configurations. The basic procedure of a potential generation with *potfit* starts with the crucial step of selecting the appropriate reference configurations. Appropriate means selecting them carefully according to the situation the potential will be applied to. That includes crystal structure, composition, temperature, or pressure. The general rule is that the set of structures should be close to the structures which will appear later in the simulation. One should be very careful when using a potential in situation it has not been trained for. In that case it will be some sort of extrapolation, which is not the primary purpose of Force Matching. The goal is to interpolate between the set of structures to describe a particular situation. This sounds like no further information can be gained, but – keeping in mind the limits of *ab initio* calculations – the main advantage of MD and using a force-matched potential is the significant increase in system size as well as decrease of computation time.

The selection of the reference structures also defines the transferability of the potential. The transferability of a potential indicates how broad the application range of the potential is. For example, a potential fitted to bulk structures will most certainly perform bad at surface structures. Including surface structures to the reference database improves the performance at the surface. It has therefore a higher transferability and can be used more generally. However, it shows lower precision at bulk simulations. What may be gained in transferability will be lost in individual accuracy. The cause of this deficiency is the fact that the energy hypersurface $\varepsilon_\alpha(\mathbf{R})$ of equation (2.3) is represented by simple model functions. By solving (2.3), the energy hypersurface $\varepsilon_\alpha(\mathbf{R})$ can be calculated for every possible atomic configuration \mathbf{R} . It is “transferable” to any situation. However, the model functions – an approximation of the energy hypersurface – cannot account for every possible configuration.

After defining the application range of the potential – meaning selecting the fundamental types of structures – those structures have to be modified further. At this point, they are usually available as ground state structures, which is unfavorable for two reasons. First, the reference structure should contain as much reference information as possible. Initially having ground state structures prevents this, since no forces act on the atoms and only the energy of the structure will effectively enter the target function of the fitting routine. Second, the model functions in *potfit* are implemented as tabulated functions,¹ interpolated with splines. The spline knots – sampling points of the functions – are the parameters α of the optimization run with *potfit*. As the potential models are in general functions of the pair distance r_{ij} between two particles (exception: embedding functions or angle dependent terms) the number and location of the sampling points is connected to the occurrence of pair distances in the reference database. Pair distances should appear in every sampling

¹ *potfit* also supports analytic functions. Advantage: parameters are global and less in numbers compared to the sampling points of tabulated functions. Disadvantage: the potential form is constrained by the analytic function.

point interval, otherwise some parameters do not influence the target function. Such non-supported parameters can take an arbitrary value and the optimization run will fail. This problem most certainly arises in case of ground state structures, since the pair distances are distributed as peaks, at least for solids with periodic structure. Thus – as shown in Figure 3.1 – there is a mutual dependence between sampling points and reference configurations. Regarding the problem at hand, either of them has to be set while the other is adapted.

A common approach is setting the sampling points as an equidistant grid and making sure that all parameters are supported by the reference data. This leads to the modification of the ground state structures, which has been already discussed above. The basic idea is to introduce disorder to some extent, which can be achieved with different strategies. One strategy is using an MD simulation at certain temperatures to produce snapshots, similar to the proposed main strategy at the beginning of the optimization cycle. As there is probably no potential available, either an *ad-hoc* potential² is taken or short *ab initio* MD runs are performed. Another possibility is distorting slightly the lattice dimensions and, afterwards, displacing the atoms randomly from their equilibrium position. Those strategies are not mandatory, any other approach with the same effect will suffice. However, they should be in accordance with the physical problem one wants to describe with MD simulations.

Preparing the Starting Potential. Another important preparation is choosing the basic potential model. This step usually occurs at the same time as or even prior to selecting the reference configurations, since the model can help creating sufficient reference configurations. Even more evident, it is essential to check for an appropriate model before considering the generation of an effective potential for the given material system. Every potential model has its limits, some are known at this stage and determine the decision for a particular model. But one must always be aware that problems can arise in the course of the fitting process. A wrong model may be also the reason for a failed fit.

After selecting the potential model, the parameters of that model have to be set. In case of tabulated potentials the parameters are the sampling points, cutoff radius, and gradients at the lower and upper boundary of each function. As discussed earlier, the number and location of the sampling points is related to the reference configurations. Using this relation, a necessary set of sampling points can be found, serving as a first setup. The values of the sampling points can be chosen arbitrarily. Thus, setting all the sampling points to zero is a valid approach. But care must be taken when using EAM models, as the transfer functions have to be different to zero. Otherwise, the transfer density is zero and therefore has no influence on the target function. Any non-zero values correct this behavior. Taking values of a linear function is one way to achieve that.

There are strategies to optimize the number or location of the sampling points but these parameters belong to the group of parameters which should be simply set at the

² Usually a crude approximation of a potential, for example, an effective potential that is intended for a different material.

beginning and only considered later in the whole optimization cycle. The same holds for the cutoff radius and the gradients at the boundary of each function. The cutoff is usually in the range of a few angstroms. It is limited to improve computational speed. A good estimate for the minimal cutoff is given by looking at *ab initio* calculations of different pair distances. Two different choices for the gradients at the boundary can be made. Either they are set to fixed numbers – usually natural boundary conditions are employed – or included as additional free parameters to the optimization. An exception is the gradient at the cutoff radius. As the interaction range ends at the cutoff, the function values of the distance dependent functions are kept at zero in *potfit*. Thus, the only reasonable choice is also fixing the gradients to zero, since the functions should be smooth at the cutoff.

Again, setting the gradient values as well as the other potential parameters is less important at this stage. The goal is having a sufficient set of parameters to work with, meaning, being able to perform first optimization runs with *potfit*. The systematic analysis of those parameters should be introduced later.³

Gauge Considerations. In the case of an EAM potential, the preparation of the starting potential is completed when the transfer densities are scaled to a domain of $(-1; 1]$ for the embedding function, which is the internal *potfit* convention and executed in the context of fixing the gauge degrees of freedom. This fixing is crucial for a successful fit and – as mentioned in Section 2.1.2 – can be achieved by setting the gradients of the embedding functions for a particular density to zero and by scaling the transfer densities to a specific definition area. The general approach of keeping such a gauge during an optimization run is realized by so-called dummy constraints

$$\omega_\rho (f(x_0) - f_0)^2, \quad (3.1)$$

which are added to the target function and should vanish in the optimization minimum ($f(x_0)$ being the gradient for example, explicit details in [38]). In that manner the correct gauge is adjusted throughout the optimization. However, in the course of the optimization run the dummy constraints can be “drown out” leading to transfer densities outside the domain. Two additional strategies are implemented in *potfit* to counteract this behavior. Firstly, by “punishing” densities which are far off the definition area [38],

$$\omega_i \sum_{j=1}^{N_i} d_{ji}^2, \quad i = 1, \dots, N_{\text{config}},$$

$$d_{ji} = \begin{cases} (n_{ji} - n_{\min}) & \text{if } n_{ji} < n_{\min}, \\ (n_{ji} - n_{\max}) & \text{if } n_{ji} > n_{\max}, \\ 0 & \text{otherwise.} \end{cases} \quad (3.2)$$

³ The *potfit* run-time parameters fall into the same category. The most noteworthy ones are energy weight and starting temperature of the Simulated Annealing algorithm, with reasonable values of 50 to 100 for the weight and 1 for the temperature.

Secondly, repeatedly rescaling the potential to the correct gauge by applying directly the transformation rules in eqs. (2.25) and (2.26). Both strategies do not work perfectly well.

At the end of an optimization it is still possible to have punishments. If the punishments are too high, the fit results should be reconsidered as the optimization run has probably been negatively influenced. Reducing the number of sampling points for the embedding functions can help in this situation.

Due to the spline interpolation the periodic rescaling is not an exact operation and introduces errors. That is why rescaling is an additional option which can be incorporated at the compiling stage. And, for that reason, it is listed as a *potfit* run-time parameter in the work flow diagram in Figure 3.1. However, since *potfit* uses internally different gauges for the rescale and non-rescale part, care must be taken. For example, if one performs a run with rescaling and afterwards a run where the rescaling is disabled, either the dummy constraints are able to adjust the potential to the new gauge or the gauge must be adapted to match the gauge of the rescale part.

To conclude this paragraph, the starting potential should be scaled to the correct gauge, for example, by performing one Powell optimization step with an additional rescaling. It is possible to start without the scaling, but the search algorithm – in particular Simulated Annealing – will most certainly take too much time to get to the right gauge.

3.1.2 General Remarks

As mentioned at the beginning of this chapter, the biggest challenge for a successful potential generation proved to be the lack of a general systematic strategy. There are a lot of different parameters of different types. The influence of the parameters on the fit results is difficult to trace, i.e., it is not apparent which conclusion should be drawn when changing such a parameter. Consequently, the overall systematic “grip” on the fitting process is hard to find and a lot of time is spent on getting a “feel” for the parameters. In this paragraph some gained knowledge on how to approach this problem appropriately are presented.

The most important aspect is the building of a potential database where all the relevant information are put together. This includes the fitting parameters as well as the various fitting results. A database is a very helpful tool, since the fitting problem usually evolves rather fast in a significant number of different potentials. Thus, the obvious purpose is to keep track of all the potentials. However, the more important feature of such a database should be the ability to quickly compare the various potentials and their quantities. Since the parameter space is not quite transparent at first sight, the influences of the different parameters have to be investigated extensively. The process involves a lot of trial and error. Nevertheless, it provides deep insight into the particular fitting problem and the shape of the parameter space. For example, despite the fact that the root mean squares differ the corresponding

potentials can be very similar in potential form. They are obviously in the same domain of the parameter space, the fitting just exhibits different local minima which are close together. By just looking at the root mean square this correlation might have been missed. Such knowledge helps evaluating the importance of a parameter or decision criterion at a certain stage in the fitting procedure.

The above statement contains an aspect which has been mentioned before, the hierarchy of parameters. Sampling points, cutoff radii, or energy weight are not important at the beginning of the fitting process. If a potential fails to produce a desired property in any satisfactory manner, adjusting and optimizing those parameters will not introduce this property, even though the rms is reduced in the process. The necessary information was not included in the first place, thus, the reference configurations have to be reconsidered. On the other hand, if the basic information exists in the data, optimizing the parameters of “lower” hierarchy and therefore reducing the rms will most certainly enhance the desired quality of the potential.

At this stage of fine tuning, the “overfitting” of a potential should be tested. This can be used as a strategy to optimize the number of sampling points. Increasing the number of sampling points will improve the rms as more parameters are introduced into the over-determined fitting problem. However, at some point the potentials are fitted too closely to the reference data. The extreme would be one fitting parameter for every reference data. That is not the desired goal. As mentioned earlier, the potential should be able to interpolate between the different reference configurations, describing structures nearby the reference configurations. To avoid this behavior of overfitting, the final potential is checked against reference configurations not included in the potentials. If the rms of those “test structures” does not get reduced or even gets worse, overfitting takes place and the number of sampling points has reached its limit (strategy proposed in [56]).

Another useful strategy is including validation results as early as possible in the fitting cycle. In the context of different types of parameters and their hierarchy, considering the results of the validation helps steering the overall fitting process from the start. The early feedback from validation tests gives hints for wrong or incomplete reference data, which were not visible in the direct fitting results. Also, the influence of parameter modifications can be better seen and understood. Important for this strategy to work is to find a clear definition of what the potential should accomplish at the least, such as a mandatory property (or properties) which the parameters of the potential can be easily checked against. As the validation is a post-processing evaluation, the implementation of this comparison is problematic. Automation of certain evaluation steps should be considered from the beginning, since a lot of different potentials have to be compared in the course of the fitting process.

3.2 Effective Potential for the MnAs/Au Interface System

The generation of the effective potential for the MnAs/Au interface system involved a lot of the adjustment paths shown in Figure 3.1. As previously mentioned, from this flow diagram the optimization loop with the adaption of the reference configurations is important at the beginning of the process. The reference configurations are the core of the potential. For this reason, a short description of those reference configurations is given in the following, where the initial optimization loop is apparent. Afterwards, some additional details on the fitting process are presented, next to the resulting potential. In the end of this section the crucial validation of the effective potential is discussed.

3.2.1 Fitting Process of the Potential

The explicit fitting process for the EAM potential has been done according to the strategies mentioned in Section 3.1. However, most of the general strategies were gained during the process and not applied from the beginning. Therefore, a full description of the process is omitted at this point. The preceding section of the fitting strategies shall fulfill the purpose instead as it conveys the approach taken. The focus in this section lies on the reference configurations used for the final potential as well as on the final stage of the process, the fine tuning.

Reference Configurations. The MnAs/Au interface system with gold growth on MnAs is the main application of the desired potential. Thus, the reference configurations need to describe gold bulk and surface structures (system I), MnAs bulk and surface structures (system II), and interface structures (system III). Table 3.1 gives an overview of the used reference configurations, separated in the three different systems I-III. The crystal type, specific structures, number of configurations, and average number of atoms per configuration are listed as well as some details about the generation of the reference structures. In total, the reference database consists of 174 different configurations with an overall number of 16 246 atoms. Together with three force components for each atom and an energy value for each configuration, the reference database consists of 48 912 single reference data points the final potential has been fitted to. Structures of system I and II were treated separately, meaning potentials for each system were created first. Only in the last step of building the final potential, all three different systems have been considered. The separate treatment was employed, since it is an interface system, hence, MnAs and gold are separated and not mixed in one alloy. Especially concerning the final step this approach proved to be advantageous.

Several approaches were applied to produce a sufficient set of reference structures, strategies already mentioned in Section 3.1.1. The general idea is starting from appropriate ground state structures and modifying them accordingly. Quantitative

details of that modifying process are not crucial. The objective was always to get the radial distribution of the ground state structures smeared out sufficiently.

Table 3.1. An overview of the reference configurations: The first three columns display the general system, lattice type, and specific structure. The structure of the $\{10\text{-}10\}$ MnAs surface includes three different surface terminations, labeled As2, As1 and Mn (see Figure 3.2). The fourth column describes the number of configurations N_c as well as the average number of atoms per configuration N_a . In the last column some information about the generation of the reference configurations are given. MD snapshots with an *ad-hoc* or an intermediate potential were used. Also, the lattice constants have been strained with additional random shifts of the atoms out off their equilibrium position.

system	type	structure	N_c/N_a	comment	
I: Au	fcc	bulk	15/64	strained	
			23/64	MD (<i>ad-hoc</i>), 300 K	
		$\{100\}$ surface	15/72	strained	
			22/84	MD (<i>ad-hoc</i>), 300 K	
II: MnAs	NiAs	bulk	15/108	MD (<i>ad-hoc</i>), 300 K	
			15/128	MD (intermediate), 600 K	
		$\{10\text{-}10\}$ surface	As2	9/85.3	<i>ab initio</i> MD, short run
			As2	8/128	MD (intermediate), 300 K
			As2, As1, Mn	24/90	strained
III: MnAs/Au	NiAs/–	$\{10\text{-}10\}$ surface/ Au adatoms	As2	3/76	manual placement of Au
			As2	9/120	MD (<i>ad-hoc</i>)
			As2, As1, Mn	16/122.6	MD (intermediate) deposition of Au

System I - Au Reference Configurations:

The starting structure for all the different reference configurations was a face centered cubic lattice with the experimental lattice constant. Surface and bulk structures were then modified as follows. The volume was strained along the cubic lattice constant (maximum strain 3%) with additional random shifts of the atoms out off their equilibrium position. Furthermore, MD snapshots simulated with an *ad-hoc* potential were produced at room temperature. The surface structures include only the $\{100\}$ surface. Although the starting structure is based on a face centered cubic crystal (fcc) with the experimental lattice constant, the final potential reproduces the *ab initio* lattice constant (see Section 3.2.2).

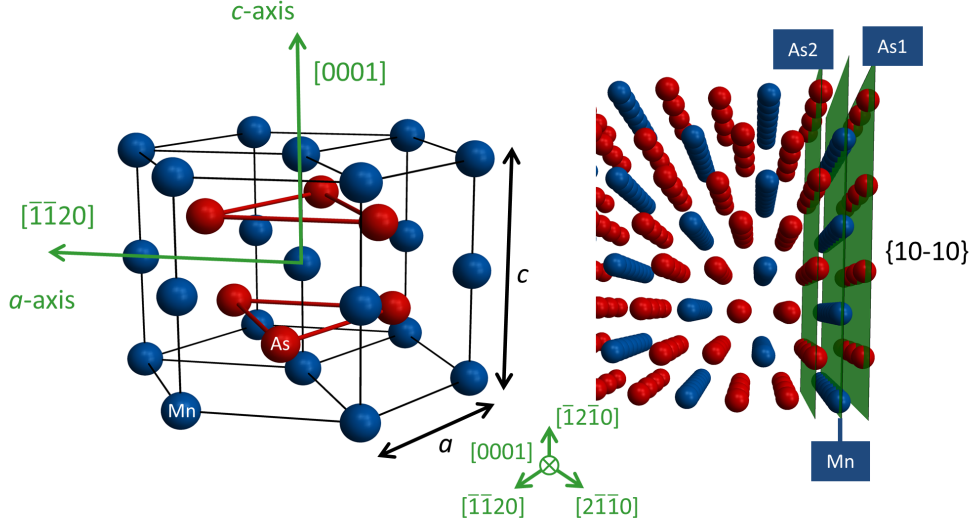


Figure 3.2. MnAs in the hexagonal NiAs structure: On the left, arrangement in a hexagonal cell showing the full dimension of the lattice parameters a and c . On the right, the different surface terminations of the $\{10-10\}$ surface. The surface can either be terminated with one As layer (As1), one Mn layer (Mn), or two successive As layers (As2).

System II - MnAs Reference Configurations:

MnAs reference configurations are based on the hexagonal NiAs crystal structure, the structure in which the MnAs nanoclusters crystallize in experiment [2–4]. The experimental lattice constants were chosen for the starting structure. In a first set of reference structures, an *ad-hoc* pair potential was utilized. This potential is derived from a simple pair distance relation calculated with *ab initio* methods. Several MD snapshots of bulk structures at room temperature were created with the *ad-hoc* potential. Surface structures are considered by including the $\{10-10\}$ surface with three different surface terminations. They are shown in Figure 3.2, next to the hexagonal NiAs structure. The $\{10-11\}$ surface is also apparent in experiment, but investigating that particular surface was originally not intended when building the database. However, as the validation of the potential shows later, other surfaces like the $\{10-11\}$ surface are described by the potential with an accuracy equivalent to the $\{10-10\}$ surface. Snapshots from *ab initio* MD simulations and strained structures are used as reference configurations for the $\{10-10\}$ surface. The strained structures were produced by increasing and decreasing the unit volume up to 20% while keeping the lattice parameter ratio of c over a fixed. Like in the case of the strained gold structures, the atom positions are shifted randomly by a small amount.

The potentials generated from the first set of configurations exhibit non repulsive behavior for short pair distances, especially the As-As interaction. That was corrected by supplementing the final reference configurations with MD snapshots at higher temperature (around 600 K), produced with an intermediate potential.

System III - MnAs/Au Reference Configurations:

For the last system reference configurations had to be found which represent the deposition of gold atoms on the MnAs surface. A first set included configurations where a few gold atoms are manually placed above the MnAs {10-10} surface. Additionally, a small amount of gold atoms were simulated on top of the MnAs surface, again with the help of an *ad-hoc* pair potential based on *ab initio* pair distance calculations. A potential was created with this first set, enabling Au deposition simulations on the three different surface terminations. MD snapshots from those simulations complement the final configuration database.

Ab Initio Calculations. The *ab initio* calculations of the reference calculations were done with the VASP program package [57–60]. That includes also the *ab initio* MD runs required to create suitable reference structures. The projected augmented wave method (PAW) was used with employing the PBE parameterization of the generalized gradient approximation (GGA) to the exchange-correlation functional. Extensive convergence tests were performed beforehand to determine the appropriate numerical parameters of the *ab initio* calculations.

The most important parameter is the k-point mesh as the forces are very sensitive to it. The k-mesh density is kept consistent as far as the different cell sizes of the system I-III allow it. Explicit values for the gamma-centered and automatically generated k-grid are a $4 \times 4 \times 4$ grid for the bulk structures and $1 \times 4 \times 4$ grid for the surface structures. A further essential parameter is the energy cutoff of the plane wave expansion. In VASP this is governed by the variable ENCUT. The influence of the ENCUT parameter turned out to be less important than the k-mesh. Starting from a relatively high setting of ENCUT= 800 eV for the structures of gold (system I), the parameter could be reduced to 400 eV for the other two systems, still yielding sufficiently accurate results. In the final setting the absolute value of the total forces on each atom and the energies for each configuration show convergence of at least two decimal places in their respective units (eV/Å and eV). Since the smallest value of the total force has the magnitude of 10^{-1} , this also means that the accuracy is at least one significant number for the smallest magnitudes of the reference data⁴. It is a reasonable accuracy, as the typical rms of a fitted potential model is in the range of 10 to 100 meV/Å for the forces.

All structures including MnAs were calculated magnetically by setting ISPIN=2 (collinear spin-polarized calculation). For the smearing the method of Methfessel-Paxton order 1 was used with a smearing width of SIGMA=0.2 eV.

Fine Tuning. As mentioned in the previous paragraph, EAM potentials were first generated for gold and MnAs separately. After various different *potfit* runs and intermediate potentials, final potentials for each system were available. Several fine

⁴ Which are the small forces, as the magnitude of the energies is about 1 eV.

tuning steps were done in the last stages of the optimization. The effects of different energy weights, cutoff radii, and reduced sampling point densities were investigated by including some validation results in the process. The lattice parameters and surface energies predicted by the potential were compared to the corresponding *ab initio* values. Both quantities are not used as fit data (keeping in mind, fit data are only forces and energies) and picked as mandatory quantities the potential should at least reproduce. This approach – among other things – made it possible to detect artificial wiggles of the potential functions, especially at the long range boundary. If reducing the sampling points or the cutoff radius of a function has no or only little influence on those quantities, the potential is adapted accordingly. Reducing the sampling points is often a good idea, since it avoids the overfitting problem. In that regard, calculations of the root mean square of test structures revealed no sign of overfitting.

Some additional conclusion could be drawn from the comparisons. The long range contribution of the embedding density in the transfer function turned out to be not important. This led to a significant reduction of the cutoff radius for those functions, as seen in the final potential. The parameter space of the fitting problem in the fine tuning stage consists of various local minima, i.e., having different potentials with a comparable accuracy. Since the changes in that accuracy are small and not always improving the quality of the considered quantity, it showed that the maximal optimization limit for some parameters has been reached. Another important aspect in that fine tuning stage was doing *potfit* runs without the periodic rescaling as it introduces additional errors. Only using the dummy constraint for keeping the gauge avoids the behavior and led to improvements of the potentials. Like mentioned earlier, the internal implementation of the gauge had to be adapted, because *potfit* uses different types of gauges for the rescale and non-rescale part. Furthermore, the embedding function boundary at high densities caused sometimes problems as the extrapolated values outside the definition regime were not “repulsive”, meaning, the embedding function runs to significant negative embedding energies for high densities. Such behavior has been handled by either adapting the number of sampling points or, in this case more efficient, artificially changing and fixing the upper boundary to force the embedding function to a more desirable extrapolation regime. Although the measure seems a bit drastic, the influence on the potential and its accuracy was only marginal and therefore acceptable.

With both EAM potentials available for each system – MnAs and Au – the next effort was joining them in order to build the EAM potential for the complete interface system. Starting from the two generated EAM potentials for each system, the interaction between MnAs and Au has been introduced, i.e., two new pair functions – Mn-Au and As-Au – were added. Taken as a starting potential, an optimization run to reproduce the values of all three reference configuration was performed in a first attempt. The general problem with this approach is that the achieved accuracy of the individual potentials is lost at the end of the optimization run. In order to keep the quality of the potentials, the former interactions had to be fixed (adjustable option in *potfit*). The step is reasonable, since the potential – like mentioned before – should describe an interface system between MnAs and Au

and not some sort of alloy including all elements. Even with that idea of fixing in mind, the joining of all interactions proved to be still challenging. The two new pair functions have to be adapted and therefore were not fixed. However, the question remains if all the functions of the existing potentials for MnAs and Au should be kept fixed. A reasonable choice is keeping the embedding and transfer functions free to be optimized, as those functions can be influenced by the reference configurations. The transfer densities and embedding energies for each element are included in the interaction of Mn-Au and As-Au.

It turned out that this assumption was not mandatory. The interaction of MnAs with Au can be built by the new pair functions and the fixed transfer and embedding functions. The reason is the fact that fixed functions have an influence on the gauge of the EAM model. One gauge degree of freedom makes it possible to move contributions from the pair interactions to the transfer functions and vice versa (see (2.25)). Fixing the pair functions will fix this gauge degree of freedom. But the gauge is now not necessarily equal to the one *potfit* is trying to conserve by applying periodic rescaling and dummy constraints. Further, the optimization with periodic rescaling fails when using fixed pair functions. Thus, periodic rescaling had to be turned off in general. With the dummy constraints enabled, the optimization runs successfully, i.e., a minimum is found. However, the constraints and punishments are unnecessary and even problematic, since they do not vanish in the minimum of the optimization if the gauge is different. In that case they have a negative effect on the search for the minimum.

To find out the best setting for the joining of all interactions, different combinations of those settings were tested. That included fixing either transfer function or embedding function or both, as well as choosing reference configurations from all three systems or just the ones from system III. Disabling the dummy constraints and punishments was also added to the testing, for the reasons discussed above. The best result was achieved by fixing all functions except the new pair functions, turning off any dummy constraints and punishments (*potfit* option “nopunish”), and using only the reference structure of system III⁵. Keeping the transfer function and embedding function free leads to a loss in accuracy of the individual potentials for MnAs and Au, like it was the case when joining the interactions without using fixed potentials.

Final Potential. The numerical quality of a potential fit is represented by the root mean square deviation. As pointed out earlier, the rms is a measure for the deviation of potential values $F_k(\boldsymbol{\alpha})$ and reference data F_k^0 . It is defined by

$$F_{\text{rms}}(\boldsymbol{\alpha}) = \sqrt{1/N_{\text{R}} \sum_{k=0}^{N_{\text{R}}} (F_k(\boldsymbol{\alpha}) - F_k^0)^2}. \quad (3.3)$$

⁵ Technical note: in order to use the generated models for MnAs and Au for this kind of reference structures, a new sampling point at the minimum left boundary had to be added by extrapolation and removed after optimization.

Table 3.2. The root mean square deviations of the energies per configuration as well as the force components of each atom between the EAM model and the reference data of each system: In the case of system I and II, the values correspond to the fit of the individual EAM models for Au and MnAs, respectively. For system III the deviations are the results of fitting the pair functions Mn-Au and As-Au to the reference data, while all other model functions were kept fixed during the optimization.

rms deviations	energies [meV]	forces [meV/Å]
system I: Au	6.38	33.90
system II: MnAs	16.45	92.85
system III: MnAs/Au	45.56	213.33

In contrast to the target function (2.47), the rms does not include any dummy constraints or weights. Hence, the rms is the true indicator for a mathematically successful optimization run, since it describes the unbiased deviation of model values and reference data.

The collective rms deviations of the final potential for MnAs/Au is shown in Table 3.2. The rms errors are calculated for the set of energies and forces separately, which are the two types of reference data the potential has been fitted to. As mentioned previously, individual EAM models of Au (system I) and MnAs (system II) were produced. The interaction between Au and MnAs was realized by fitting the pair functions Mn-Au and As-Au to the reference structures of system III, while keeping all other model functions fixed. For that reason rms deviations of three different optimization runs are available. The rms errors increase with every system, starting from I to III. On the one hand, this behavior can be explained by the applicability of the potential model to the material system in general. However, the conclusion seems obvious that the rising number of elements in the model is responsible for the increasing rms as well. The complexity of the model increases with every element, since new potential functions are added.⁶ As the problem gets more complicated, the EAM model may work better for a system with fewer elements.

With the help of the so-called scatterplot, the fit result is visualized by plotting every fitted potential value against the corresponding reference data point. Figure 3.3 shows the scatterplots of the final potential for each system. The straight line $y = x$ through the origin is equivalent to perfect agreement. A failed optimization run is immediately visible if the scatterplot has absolutely no resemblance to a straight line. The accuracy of a fit is represented by the thickness of the scatterplot, which can be seen by comparing the rms deviations of Table 3.2 to the line thickness of the particular scatterplots. The analysis of the scatterplots makes it also possible to detect problematic reference structures, i.e., structures the model describes significantly worse in comparison to other configurations. Such information is valuable in finding the appropriate reference configurations (referring to Section 3.1.1).

⁶ The total number of functions of an EAM model is $n_{\text{total}} = n_{\text{elem}}(n_{\text{elem}} + 5)/2$, n_{elem} being the number of elements.

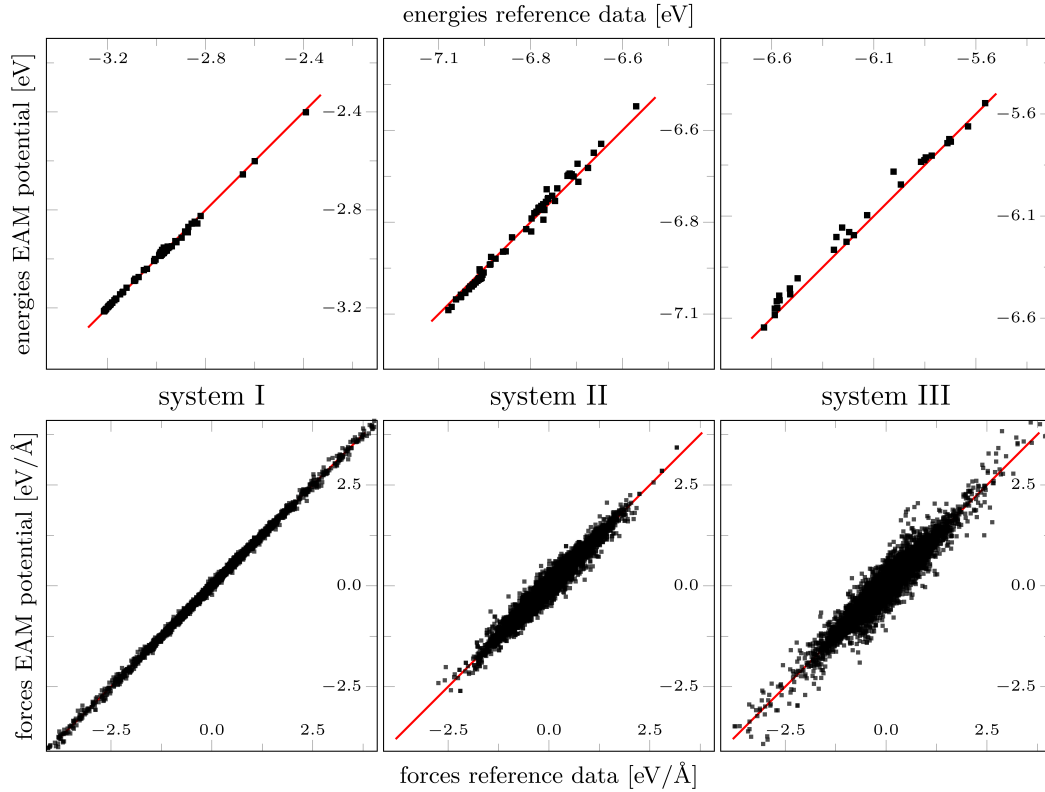


Figure 3.3. The scatterplots representing the fitting data for each system: The potential values (y axis) are plotted against the reference values (x axis). The upper plots show the fitting data of the energies, the lower plots those of the forces. A perfect agreement represents the red line $y = x$ through the origin.

Figure 3.4 displays the functions of the final EAM model for the MnAs/Au interface system. The potential model consists of 12 functions, that includes 6 pair functions for each pair interaction as well as 3 transfer functions and 3 embedding functions for each element. The points on each function line are the optimized sampling points (spline knots) of the *potfit* run, whereas the lines are the tabulated function values of the potential format of the MD package LAMMPS [61, 62]. For this potential format LAMMPS uses a linear interpolation scheme, thus, the function values are the result of a spline interpolation with a very narrow spacing of each point⁷. For the pair functions the number of sampling points is 20 with a relatively high cutoff radius of $r_c = 7 \text{ \AA}$. The pair functions of Mn-Au (14) and As-Au (10) are an exception as they have shorter cutoff radii in the range of 4 to 5 \AA . The same holds for the transfer function with 11 to 12 sample points. Like mentioned previously, the shorter radii are the result of the fine tuning of the potential. The long range contribution of those functions had negligible influence on the target function. For all functions the spacing of sample points is equidistant, with one

⁷ *potfit* offers the possibility to write the potential output for LAMMPS. The responsible routine had to be adapted in order to consider different cutoff lengths correctly.

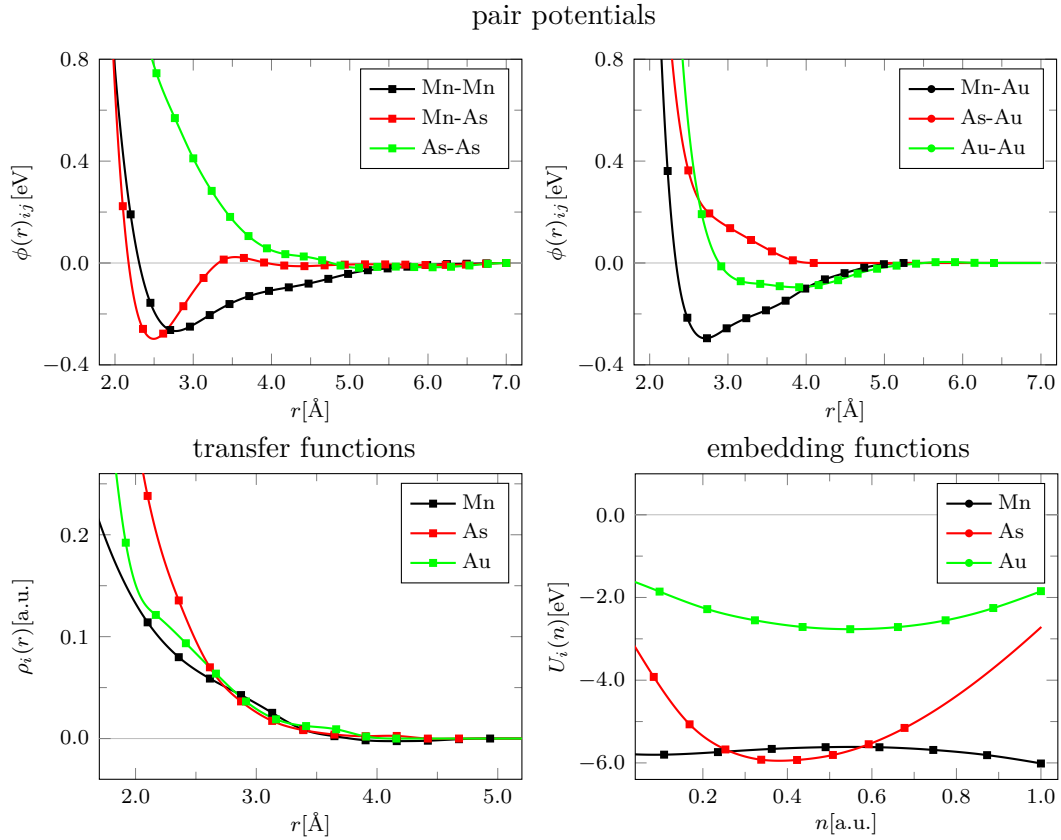


Figure 3.4. The final EAM potential for the MnAs/Au interface system: The plots show the spline knots of each model function and the corresponding cubic spline interpolation.

exception at the lower boundary of the Au pair interaction. The spacings have the same distance of approximately 0.25 \AA for every pair and transfer function. However, the spacing distance of the embedding function depends on the available density range and the applied gauge and is determined in the internal rescaling scheme. The complete list of sampling points can be found in the Appendix.

3.2.2 Validation of the Potential

The importance of validating the potential has already been stressed several times. The optimization on its own does not ensure the quality of a generated effective potential. Only the comparison of quantities – evaluated with the potential – to data not included in the fit can show the reliability. There are all kinds of different quantities the potential can be checked against, but usually one considers properties that are related to the situation the potential will be used later in an MD simulation. In that regard, when using the potential for situations it has not been trained and validated for, one should keep in mind possible shortcomings of the results.

In order to validate the potential for MnAs/Au, bulk properties of both MnAs and Au were tested first. That included the most basic validation test of running a simple MD simulation to check whether the potential model stabilizes the structures of Au and MnAs, which is the fcc or hexagonal NiAs structure respectively. After fulfilling this requirement a quantitative analysis was done by looking at the structural and elastic properties, i.e., the lattice parameters and elastic constants. As the main purpose of the potential is to simulate the gold deposition on the MnAs surface, the focus was put on the surface energies of MnAs for the second part of the validation. Additionally, since in the fitting process different intermediate potentials were unstable during surface simulations, it became necessary to take a closer look at the surface properties of MnAs.

Structural and elastic properties of bulk MnAs and Au. The lattice constants derived by the EAM potential model are $a = 3.658 \text{ \AA}$ and $c = 5.497 \text{ \AA}$ in the case of MnAs. For fcc Au the potential predicts a value of $a = 4.155 \text{ \AA}$. Comparisons to the corresponding *ab initio* values show excellent agreement. The relative deviations are less than 0.1% for all lattice parameters (summarized in Table 3.3 on p. 48). A lot of effort was put into joining all interactions for the final potential to keep this accuracy, already provided by the single EAM models for Au and MnAs (see previous Section 3.2.1). The comparison to experimental values of the lattice constants reveals a typical relative deviation from *ab initio* lattice constants, which is in general of the order of a few percent. On the one hand, the deviations are due to the approximation of the exchange-correlation functional. On the other hand, one has to keep in mind that *ab initio* values are the result of ground state calculations – meaning the values correspond to a temperature of 0 K – whereas the values from experiment are taken at finite temperatures. MD simulations consider temperature effects, but in this case a static calculation was done first to focus on the comparison with *ab initio* data.⁸

The lattice constants were determined by minimizing the potential energy as a function of the atom coordinates, a feature provided in the MD package LAMMPS. Another approach is plotting the potential energy with respect to the lattice constants – like it is done in Figure 3.5 – and subsequently looking for the minimum of the 2d plot. It has been used to check for any inconsistencies. If there are at least two lattice constants, this approach allows only the calculation of the optimal volume by plotting the potential energy over volume or the pressure over volume. Besides the excellent prediction of the *ab initio* lattice constants, the corresponding potential energy hypersurface is represented very accurately as well. Like already mentioned,

⁸ In a dynamic calculation – employed by an MD simulation – the thermal expansion coefficient for gold was estimated to $15.3 \cdot 10^{-6} / \text{K}$ by considering the increase in lattice constant in the temperature range from 287 K to 296 K. This is in good agreement with the experimental thermal expansion coefficient of $14.2 \cdot 10^{-6} / \text{K}$ at room temperature [63]. In case of MnAs the same calculation was done for the volumetric coefficient of thermal expansion. In the ferromagnetic range ($T < 311 \text{ K}$) the calculated coefficient has the magnitude of ca. $5 \cdot 10^{-5} / \text{K}$. Which again is a good qualitative agreement with experiment, since at least two experimental values are reported in literature of the same magnitude ($5 \cdot 10^{-5} / \text{K}$ [64] and $18 \cdot 10^{-5} / \text{K}$ [65]).

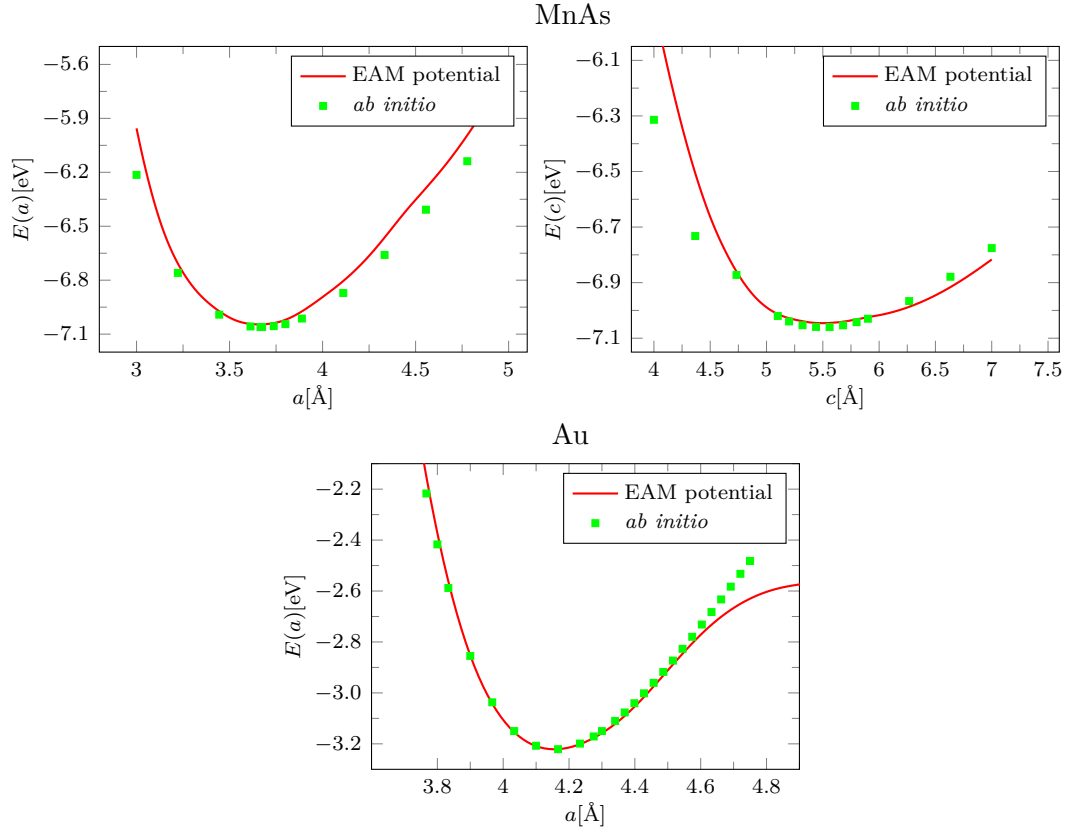


Figure 3.5. Potential energy versus lattice constant: The comparison with *ab initio* data is done for the two lattice constants a and c of the hexagonal MnAs (upper plots) and the one lattice constant a of fcc Au (lower plot). In the case of MnAs the plots were taken by setting the respective other lattice constants to $c = 5.50$ Å and $a = 3.66$ Å, which are the resulting lattice constants from minimizing the potential energy.

Figure 3.5 displays the potential energy versus lattice constants in comparison to *ab initio* data. Again, this is data which has not been considered for the optimization. Concerning MnAs the plots represent cuts through the two dimensional hypersurface $E(a, c)$ at $c = 5.50$ Å and $a = 3.66$ Å. The complete hypersurface shows similar agreement to the *ab initio* counterpart, but is omitted for lack of adequate visualization.

When looking at the reference data, it is not surprising that the potential is able to describe the potential energy depending on the lattice constants. Perhaps not with the explicit accuracy, but the potential is expected to reproduce the basic structural properties, since the reference data contains strained structures. In the neighborhood of the equilibrium lattice constants, the potential is based on strained structures of the reference data. Hence, it accurately interpolates those structures. However, above that range the reference data does not include structures with that level of strain. Thus, outside a lattice constant variation of approx. $\pm 7\%$ for MnAs and $\pm 3\%$ for Au the results are actually an extrapolation, which still results in a very good description of the potential energy.

Table 3.3. Structural and elastic properties in comparison with *ab initio* data not included in the fit. Lattice constants, potential energy per unit cell, and elastic constants are shown. The experimental lattice constants are displayed as well. All data without an upper index are results of this work.

MnAs	EAM	GGA_PBE	Experiment
$a_{\text{lattice}}[\text{\AA}]$	3.658	3.660	3.730 ^b
$c_{\text{lattice}}[\text{\AA}]$	5.497	5.498	5.668 ^b
$E_{\text{pot}}[\text{eV/unit_cell}]$	28.18	28.24	
$C_{11}[\text{GPa}]$	104.53	109.80 ^a	40.00 ^c
$C_{12}[\text{GPa}]$	42.61	42.72 ^a	8.00 ^c
$C_{13}[\text{GPa}]$	41.26	43.38 ^a	10.00 ^c
$C_{33}[\text{GPa}]$	121.11	138.43 ^a	110.0 ^c
$C_{44}[\text{GPa}]$	64.22	69.47 ^a	34.00 ^c
Au	EAM	GGA_PBE	Experiment
$a_{\text{lattice}}[\text{\AA}]$	4.155	4.156	4.078 ^d
$E_{\text{pot}}[\text{eV/atom}]$	3.221	3.220	
$C_{11}[\text{GPa}]$	156.18	154.64	201.07 ^e
$C_{12}[\text{GPa}]$	111.55	132.68	169.37 ^e
$C_{44}[\text{GPa}]$	27.37	25.92	45.10 ^e

^a *ab initio* calculation from [66]. Experimental measurements at:

^b 4.2 K [67], ^c 303 K and in the paramagnetic state [68],

^d room temperature [69], and ^e 50 K [70].

The elastic constants were determined by deforming the simulation box in different directions and calculating the change in the stress tensor, as they are the link between the stress and strain tensors. A LAMMPS script provided by the used distribution version⁹ was employed for the actual calculation. The resulting five independent elastic constants of the hexagonal system MnAs are $C_{11} = 104.53$ GPa, $C_{12} = 42.61$ GPa, $C_{13} = 41.26$ GPa, $C_{33} = 121.11$ GPa, and $C_{44} = 64.22$ GPa. For the cubic system of gold the potential evaluates the three independent elastic constants as $C_{11} = 156.18$ GPa, $C_{12} = 111.55$ GPa, and $C_{44} = 27.37$ GPa. The comparison with *ab initio* data shows a good agreement. For most of the calculated elastic constants the relative deviation is approx. less than 5%, in three cases even less than 1%. The constants C_{44} and C_{33} of MnAs as well as C_{12} of gold are an exception with higher deviation of 7.5%, 12.5%, and 15.9%, respectively. Noteworthy is the fact that the *ab initio* MnAs elastic constants are taken from an external source [66]. Hence, the values do not only help validating the potential, but they confirm the *ab initio* calculations of this work in general.

In the case of gold, the trend of the corresponding experimental elastic constants is well reproduced by the EAM potential. The relative ordering of the three constants is conserved, the values are shifted in the same direction, and the relative deviations range from 20 to 40%. The same cannot be stated for MnAs, as seen

⁹ located in the “examples” folder of the installation directory

by the high relative deviations. However, one has to consider that the experimental values are measured at 303 K and, most importantly, in the paramagnetic state, where the hexagonal NiAs crystal structure is slightly distorted (orthorhombic) [68]. Still, the relative ordering of the constants is reproduced except for C_{12} and C_{13} , which the EAM potential also missed in comparison to the *ab initio* values. This is acceptable, since the values are relatively close together.

The elastic constants and their counterparts – *ab initio* and experimental – are displayed in Table 3.3 in addition to the lattice constants. The table also shows the potential energy per unit cell as well as the experimental lattice constants for MnAs and Au.

Surface Energies of MnAs. Apart from the validation of the potential, the purpose of calculating the surface energies of MnAs was also to analyze which surface structure is the most stable. This information has been used later for the surface and deposition simulations.

The surface energy is the difference in energy between a surface structure and a bulk reference structure per surface area. Hence, in this work the surface energies are calculated according to the following definition,

$$\sigma_{\text{surf}} = \frac{E_{\text{surf}}^N - E_{\text{bulk,ref}}^N}{2A}, \quad (3.4)$$

with $E_{\text{bulk,ref}}^N = N^{(\text{Mn})} E^{(\text{Mn})} + N^{(\text{As})} E^{(\text{As})}$.

E_{surf}^N denotes the energy of an N -layer surface slab. $E_{\text{bulk,ref}}^N$ is the energy of the corresponding N -layer bulk reference structure, which consists of the energy per layer of each element, $E^{(\text{Mn})}$ or $E^{(\text{As})}$, times the number of occurring layers, $N^{(\text{Mn})}$ or $N^{(\text{As})}$, respectively. Symbol A represents the area of the surface. The factor two stems from the fact that the slab is usually described by a structure where the periodic boundaries are turned off in directions of the surface, leading to two surface sides. The surface energies are obtained in a static calculation, meaning one uses ideal structures with atoms in their equilibrium position. The considered surface structures are motivated from experiment. In Figure 3.6 three different surface directions are shown, which the MnAs nanoclusters exhibit during their growth [2, 4]. Each direction can be terminated with different layers, being either a Mn layer, an As layer, or – in case of the {10-11} surface – a mixed layer of Mn and As.

Comparing the surfaces energies of different terminations to *ab initio* data is subject to some restrictions. In order to calculate the energy per layer of Mn or As, the energy of one Mn or As atom in the bulk is required. This is not possible with the used *ab initio* code VASP. However, the energy of the periodic MnAs unit cell can be calculated, which consists of two Mn and two As atoms. For this reason a reference bulk energy is obtained as multiples of the energy per unit cell. Consequently, comparisons are only considered for surface structures which can be periodically continued. The surface terminates directly at the boundary of a periodic cell of MnAs. Such structures usually consist of two different surface terminations at

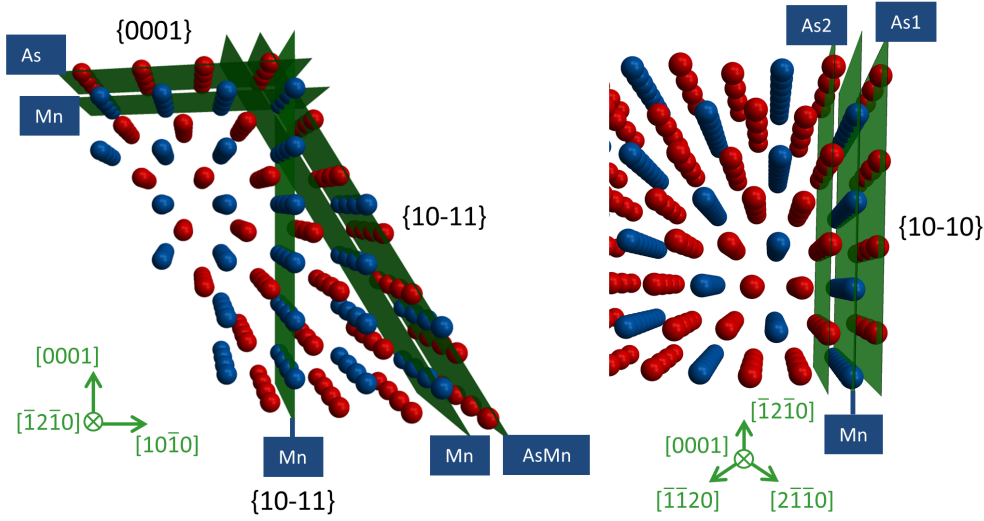


Figure 3.6. The different terminations of the MnAs surface planes $\{10-10\}$, $\{10-11\}$, and $\{0001\}$: The $\{0001\}$ surface has two possible terminations, consisting either of one As layer (As) or one Mn layer (Mn). The $\{10-11\}$ surface can be terminated with one Mn layer (Mn) or a mixed layer of As and Mn (As_Mn). Both surface planes are displayed on the left. On the right, the three different terminations of the $\{10-10\}$ surface are shown, labeled as As1, Mn, and As2. The latter corresponds to two successive As layers.

both open ends. The resulting surface energies are therefore a mean of both surface terminations. The exception is the $\{10-10\}$ surface, since – when applying periodic boundaries in that direction – the surface structure starts and ends with the As1 layer at both sides.

In summary, four different comparisons are carried out by this approach. They are listed in Table 3.4. The relative deviations are at least lower than 12%, two of which even show a deviation around 1%. In that case, surface slab and bulk reference energies exhibit the same deviation from the corresponding *ab initio* values. Thus, the deviation gets canceled out when taking the difference. The already good agreement gains more importance considering the statement of Rösch et al. [71]. They express the fact that surface energies are hard to reproduce even with EAM potentials. Their published potential for NbCr₂ shows a deviation in surface energy of about 30%. Another noteworthy aspect concerns the selection of the reference configuration. Recalling Table 3.1, the reference configurations only include the $\{10-10\}$ surface direction. Nevertheless, the other surfaces are described with a similar accuracy, proving the transferability of the effective potential in this regard.

Since the energy per atom species can be computed with the EAM potential, (3.4) is further applied to calculate the surface energies of the remaining individual surface terminations. Hence, the additional surface energies in Table 3.4 are actually predictions.

Table 3.4. Surface energies of MnAs in eV/Å²: The surface energies of the first four entries are calculated with surface and bulk reference structures having the same stoichiometry as the MnAs periodic cell. Hence, comparisons to *ab initio* data were possible. Three of the four surface energies are the mean of two different terminations due to the periodic cell requirement. The surface structures of the remaining table entries do not fulfill the periodic cell requirement. However, the effective potential is still able to predict the surface energies of those terminations.

MnAs: surface type	EAM	GGA_PBE
{10-10}_As2_Mn	0.0973	0.1070
{10-11}_Mn_AsMn	0.0693	0.0699
{0001}_As_Mn	0.0831	0.0942
{10-10}_As1	0.0595	0.0589
{10-10}_As2	0.1232	
{10-10}_Mn	0.0714	
{10-11}_Mn	0.0642	
{10-11}_AsMn	0.0745	
{0001}_Mn	0.0640	
{0001}_As	0.1023	

4 Simulation Results

The developed EAM potential for the MnAs/Au interface system has been applied in various MD simulations. In order to find a suitable MnAs surface for the growth simulation, an analysis of different possible MnAs surfaces was done at first. Afterwards, the actual deposition simulation of Au on MnAs was performed.

All MD simulations are done with the MD package LAMMPS [61, 62]. The visual representation of the MD snapshots is realized with the visualization software *ovito* [72, 73]. Next to the visualization of atomistic simulation data, the software has also a few analysis features, which have been used to investigate the grown structure of gold.

4.1 Surface Simulations

Before performing the actual deposition simulations, the MnAs surface has to be prepared in a preceding surface simulation. When starting from a cut bulk structure as surface structure, one has to make sure that the surface is described without introducing artificial effects and that the surface is relaxed appropriately. Furthermore, the exact structure and stability of the different surface terminations of MnAs nanoclusters are experimentally unknown. Hence, it is also an interesting question for the experimentalists, besides that it is necessary to know on which surface the deposition should be simulated. The most stable structure in simulation is most likely the surface structure occurring in experiment.

Figure 4.1 displays a cross-sectional transmission electron microscopy (TEM) image of a typical MnAs nanocluster from experiment. The surface directions of the three different surfaces are indicated, which have also been characterized in experiment. The surface facets of the nanoclusters exhibit no atomic steps, i.e., they are atomically flat [2]. This is an important information considering the correct setup of the surface structure for the simulation. The according surface terminations have been already introduced in the discussion and validation of the surface energies (Section 3.2.2). This time, they are shown in comparison to an experimental MnAs nanocluster, illustrating the direct connection to the experimental structure.

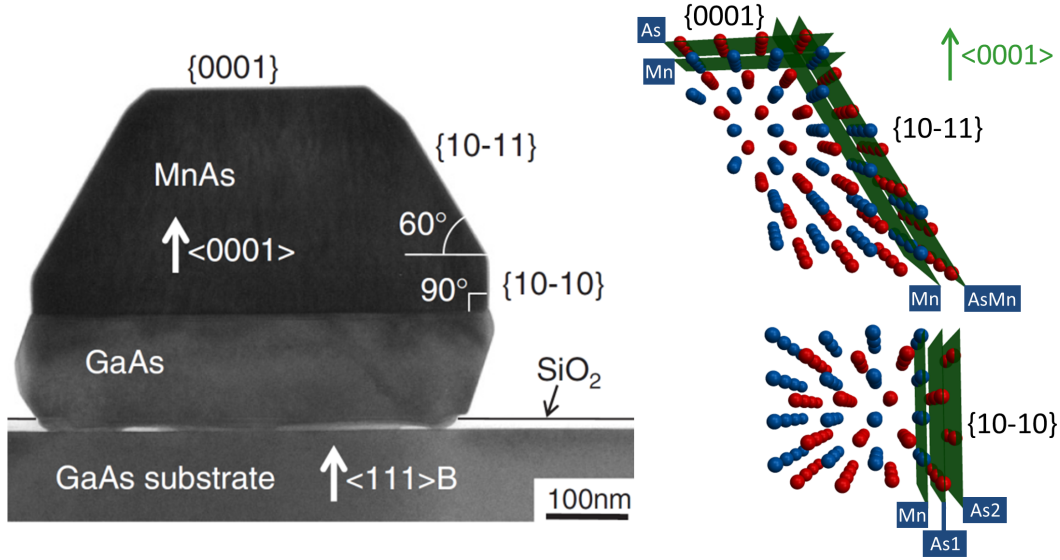


Figure 4.1. Surfaces in experiment and simulation: On the left, a cross-sectional TEM image of a typical MnAs nanocluster, taken from [2]. The surface directions are determined by experiment, whereas the explicit surface terminations are unknown. On the right, the already presented different surface terminations in direct comparison to the MnAs nanocluster.

4.1.1 Simulation Setup and Settings

For the preparation of the surfaces, a few things have to be considered in order to reproduce the surface behavior correctly in the simulations. Figure 4.2 shows the used setup of the simulation box. The atomic layers of the surface structure – or substrate – are assigned to three areas which are treated differently in the MD simulation. The lowest atomic layers are kept fix by excluding them from the actual MD integration scheme, by which the atom positions are updated each time step. Since periodic boundary conditions are turned off in the direction perpendicular to the surface, the fixed layers avoid a drift of the whole structure. This is required especially in a deposition simulation, because incoming atoms (adatoms) hit the substrate and transfer their momenta to the latter.

The area above the fixed layers is temperature controlled (NVT ensemble). The second area enables temperature control without influencing the surface structure directly. Furthermore, in the following deposition simulations the substrate will be heated by the incoming deposition particles, as they transfer their kinetic energy towards the substrate. Hence, the additional kinetic energy has to be withdrawn from the system. The explicit thickness of the thermalized area is less important. It just should be ensured that the additional kinetic energy is sufficiently removed from the system over time. The actual surface area is not constrained by a thermostat and represents a standard NVE ensemble. Thus, the surface can develop freely and

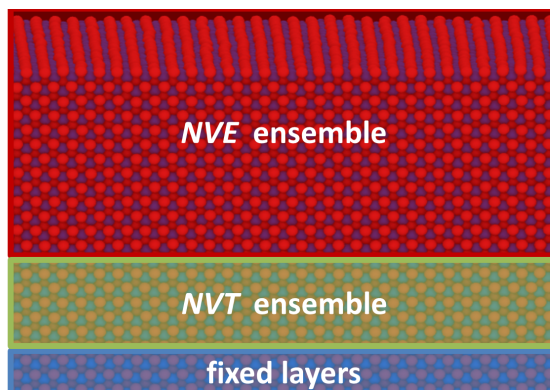


Figure 4.2. The general simulation setup for the different surfaces: In order to describe all possible relaxations or reconstructions of a surface, the structure is prepared in three different areas. The lowest layers of atoms are kept fixed. Above, an *NVT* ensemble is employed with the help of a thermostat. The layers at the top are not thermalized by using a standard *NVE* ensemble. With regard to the following deposition simulations, this setup additionally guarantees that momentum and kinetic energy transferred to the substrate by an incoming deposition particle do not lead to a position shift or heating of the substrate.

all possible relaxations or reconstructions¹ can take place. A basic rule is that the layer thickness of this area has to be bigger than the cutoff radius of the interaction model. Such a fixed/*NVT*/*NVE* layer setup mimics a surface in the best way.

For each surface terminations, simulations with similar settings were performed. The average particle number of all simulation boxes with the different surface terminations is 100 000. Depending on the specific surface terminations, the number varies slightly. When generating the structures, the number of considered unit cells in each dimension were chosen in a way to have comparable surfaces. The dimensions of the simulation box are in the order of 10 nm in each space direction (values between 8 and 16 nm). However, the box is not cubic. It is a tilted triclinic box due to the hexagonal symmetry of the MnAs structure. According to the specific set up shown in Figure 4.2, the explicit division of the different areas is as follows: At least 3 atomic layers are kept fix, while around 15 layers are controlled by a thermostat. The remaining layers (40 to 50) stay in an *NVE* ensemble.

The simulation run is split in two phases. First, a kinetic energy corresponding to a temperature of 300 K is distributed to every atom. At the beginning of the simulation, the kinetic energy drops to the half, because the other half converts to potential energy. Therefore, the Langevin thermostat is applied to get the sample quickly to the desired temperature of 300 K, since this kind of thermostat is especially suited for this purpose. Afterwards, when the temperature is reached, the Nose-Hoover thermostat generates the canonical ensemble (*NVT*) at that temperature in the middle area. Each phase is simulated for 50 000 time steps, resulting in a total number of 100 000 steps. With a time step size of 1 fs, the overall simulation duration is therefore 0.1 ns.

¹ with emphasis on “possible”, since – depending on the explicit box size or atom composition at the surface – not every surface reconstruction is possible.

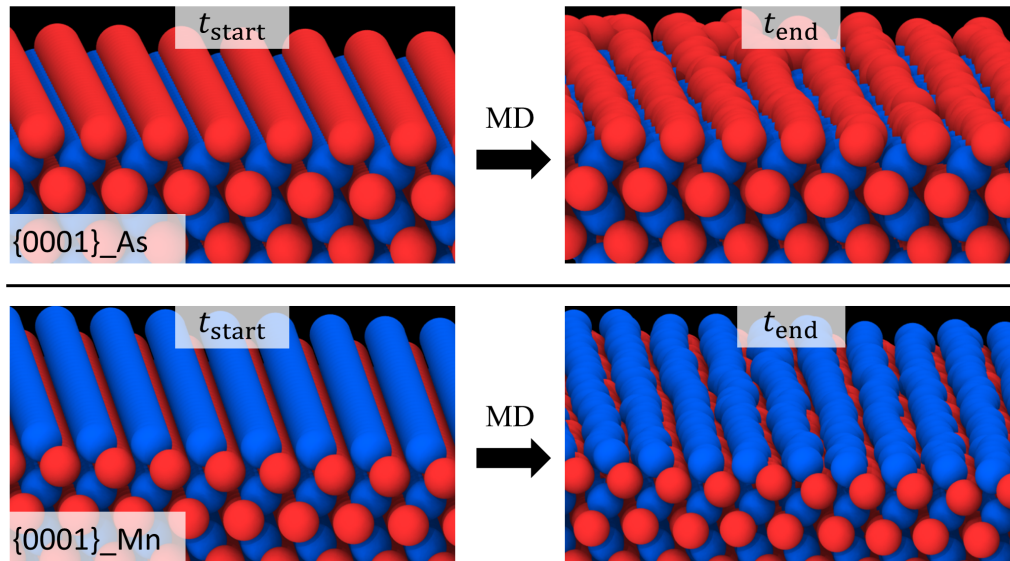


Figure 4.3. Basic stability analysis of the $\{0001\}$ surface in the As termination (top) and Mn termination (bottom): On the left, the surface structure before the simulation based on a cut, ideal bulk structure. On the right, the relaxed surface structure after the simulation at 300 K. The As terminated surface is stable to some extent. A few As atoms move away from the original layer position and build a bond to neighboring As atoms. This effect is not observed in the case of the Mn termination. The surface structure stays intact.

4.1.2 Analysis of the Different Surfaces of MnAs

General Stability of the Surface Terminations. The calculated static surface energies presented in Section 3.2.2 give first clues on the stability of the surfaces. However, as it will be clear during the following analysis, a low surface energy does not necessarily result in a stable structure when running a dynamic surface simulation.

Figure 4.3, Figure 4.4, and Figure 4.5 summarize the basic results of all seven surface simulations for each surface termination by displaying the start and end configuration of the structures. The start configurations (on the left) are the cut bulk structures before the actual simulation. The end configurations (on the right) are the resulting structures after performing the simulation with the above introduced parameters and settings, which prepare the surface to a temperature of 300 K. Only the top layers and an extract of the whole surface plane are illustrated in these figures. Each figure belongs to one surface direction with all its terminations.

The simulation results for the $\{0001\}$ surface direction – Figure 4.3 – suggest stable surfaces, as the basic surface structure stays intact for both terminations. However, at the As terminated surface some distortions are visible. A few As atoms build closer bonds to neighboring As atoms. Comparison to the surface energies reveals that the surface energy for the Mn terminated surface fits the result of the simulation, since the surface energy is relatively small and, hence, suggesting that the surface structure is stable. For the As termination the conclusion cannot be

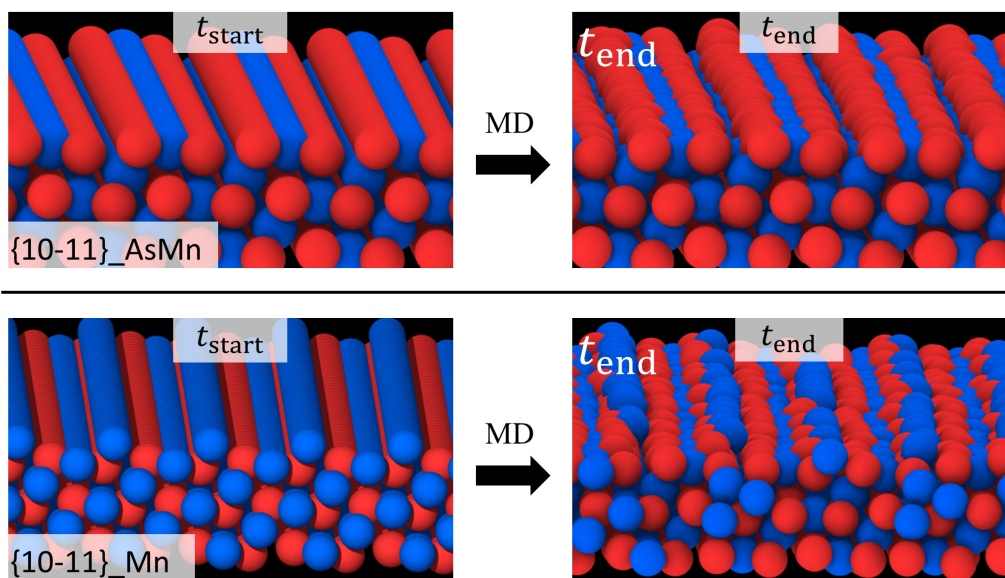


Figure 4.4. Basic stability analysis of the $\{10-11\}$ surface in the AsMn termination (top) and Mn termination (bottom): On the left, the surface structure before the simulation based on a cut, ideal bulk structure. On the right, the relaxed surface structure after the simulation at 300 K. The AsMn terminated surface remains intact. The surface in the Mn termination keeps its basic structure. Nonetheless, a few Mn atoms diffuse into the substrate and occupy interstitial sites of the third layer, also a Mn layer (see Section **Mn Interstitials** below for further analysis).

drawn this easily. The surface energy is relatively big (second largest surface energy). Still, the surface remains stable to some extent. But as shown later, heating the substrate leads to further decomposition of the first layer structure. Some As dimers are created, hovering and desorbing from the surface (see also Section **As Dimers** below).

In case of the $\{10-11\}$ surface direction – Figure 4.4 – the surface with the mixed Mn and As layer remains intact. For the Mn terminated surface, the basic surface structure is intact. However, Mn atoms of the first layer diffuse into the substrate and occupy interstitial states of the third layer (see also Section **Mn Interstitials** below). The simulation results agree with the considerable low surface energies. However, although the Mn terminated surface has a lower surface energy than the AsMn termination, the simulation shows that it is energetically more favorable for some Mn atoms to diffuse into the substrate.

According to the simulation results in Figure 4.5, only the As1 termination of the $\{10-10\}$ surface direction remains stable at 300 K. The first layer of the As2 termination immediately dissolves and the As atoms move towards the second As layer. There, close bonds are formed and As dimers are beginning to desorb from the surface, hovering above it (see also Section **As Dimers** below). In case of the Mn terminated surface, the surface starts losing its structure after a short simulation duration. Several layers deep an amorphous structure of mixed As and Mn atoms occurs.

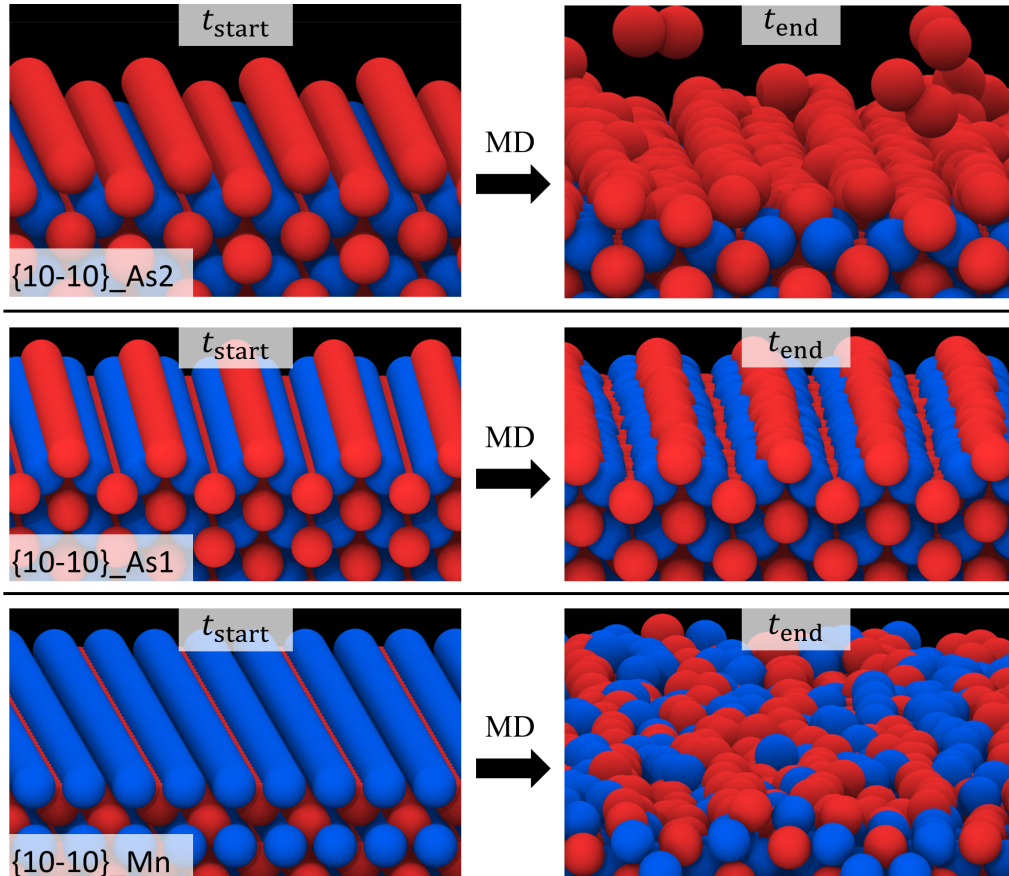


Figure 4.5. Basic stability analysis of the $\{10-10\}$ surface in the As2 termination (top), As1 termination (middle), and Mn termination (bottom): On the left, the surface structure before the simulation based on a cut, ideal bulk structure. On the right, the relaxed surface structure after the simulation at 300 K. The first As layer of the As2 terminated surface immediately dissolves at the beginning of the simulation. All its As atoms move to the second layer of As atoms and start to form close bonds. During that process a few arsenic dimer molecules desorb from the surface by hovering above the latter (see also Section **As Dimers** below). The surface structure of the As1 termination stays intact. In contrast to the stable As1 terminated surface, the surface of the Mn termination loses completely its structure and an amorphous structure of several atom layer thickness is built.

The stability of the As1 termination fits very well to the corresponding surface energy. As a matter of fact, it is the lowest surface energy of all the terminations. Hence, the stability of the surface structure has been expected. The same holds for the As2 termination. Since it has the highest surface energy, the instability of the surface structure has been also expected. However, the instability of the Mn termination contradicts the relatively low surface energy of the Mn termination.

Especially the last case proves the statement made in the introduction of this section: a low surface energy does not necessarily result in a stable structure when running a dynamic surface simulation. If a particular surface coordination is “energetically close” to another surface structure with a lower energy, the system may be able to evolve into the structure with lower energy. For the Mn termination of the {10-10} direction, the consideration of the surface energy over time revealed a significant drop in this “dynamic” surface energy and, therefore, confirming such a suggested behavior. The same drop in surface energy is observed for the {10-11}_Mn surface termination, after a significant number of Mn atoms diffused into the substrate. With the same reasoning the stability of the {0001}_As surface termination – despite the relatively high surface energy – is explained. The surface stays stable, since in the energy hypersurface no other local energy minima are “reachable” for the current system state. However, after heating the system it is able to evolve to other energy states.

In summary, at least one termination of each surface direction is stable in an MD simulation. Which is an important result, because in experiment those three surface directions are observed. Hence, the surface simulations show consistency with experiment.

As Dimers. The As dimers occurring in the MD simulation of the {10-10}_As1 termination are also observed in other research studies. Experimental investigations [74–76], *ab initio* calculations [77–79], and MD simulations [80–82] deal with epitaxial growth of thin film GaAs and the role of As dimers during molecular beam epitaxy (MBE). In such MBE growth experiments molecular beams of As₂ (also As₄) and atomic Ga are produced to deposit the material on the substrate. Investigations involve – among other things – the desorption and sticking rates of As dimers on the substrate surface as well as bond length and binding energies (for the latter see Table 4.1 on p. 61).

The *ab initio* and MD studies analyze especially the dynamics and adsorption mechanism of the As dimers, which cannot be observed directly in experiment. Those studies report different binding states of As₂, including a strong chemisorption state and an intermediate, physisorbed energy plateau. This physisorbed state corresponds to As₂ molecules hovering slightly above the substrate surface, since they are weakly bound. Without significantly changing their energy, those physisorbed As₂ molecules are quite mobile on the surface, making it possible for them to find stronger bonding sites [77]. Furthermore, the studies calculated bond lengths of isolated, physisorbed (about 2.12 Å), and strongly bound chemisorbed As dimers (about 2.54 Å) [80].

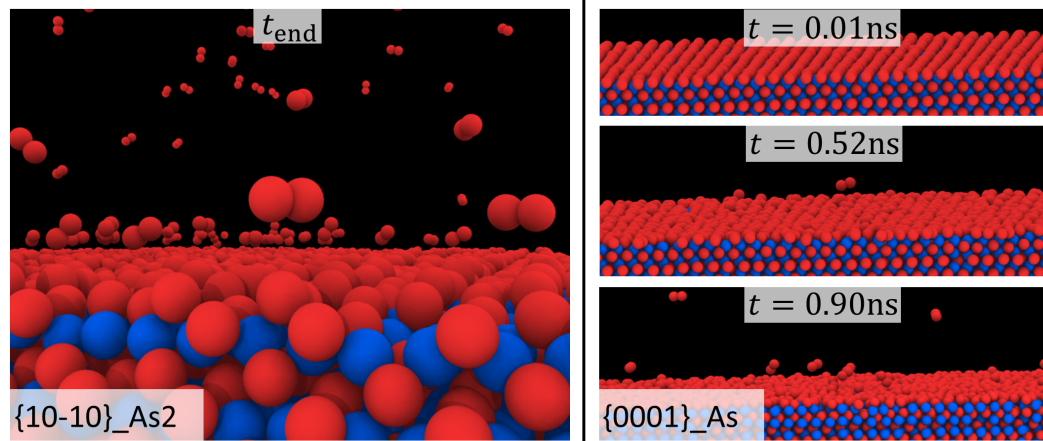


Figure 4.6. Formation and desorption of As dimers at the $\{10-10\}$ _As2 surface (left) and the $\{0001\}$ _As surface (right): Both substrates are heated up to 600 K in the course of the simulation. In case of the $\{0001\}$ _As surface the heating is necessary to dissolve the structure of the surface further to force the formation of As dimers, which is shown in the sequence of MD snapshots. The $\{10-10\}$ _As2 surface on the other hand exhibits As dimers already at 300 K. However, the process gets accelerated when heating the substrate, displayed in the end configuration on the left.

All the above stated findings about As dimers are observed in the present surface simulations as well and, therefore, confirm the predictions of the EAM potential in that particular situation. These findings also suggest a reasonable and correct behavior of the potential in MD simulations of MnAs surfaces. The physisorbed state of several hovering As_2 molecules is visible in Figure 4.6 on the left. Some isolated As dimers can also be seen. When performing a longer MD run, the weakly bound As dimers occasionally get the appropriate momentum transferred by the surface and desorb from the latter. This process can be accelerated by continuously heating the substrate. Figure 4.6 shows the MD snapshot after such heating. Simulation parameters are the same as those for the surface simulation done before, except longer time steps and heating is ensured.

The right side of Figure 4.6 shows the same heating simulation for the $\{0001\}$ _As surface termination. Like mentioned before, this surface remains unchanged to a certain degree. Some As atoms of the top layer break the order of the original structure by moving closer to neighboring As atoms. The assumption that this might be the beginning formation of As dimers has been confirmed by the heating simulation, which is shown in the sequence of MD snapshots in Figure 4.6 on the right. At first, heating causes a continuous formation of As dimers and therefore the top layer vanishes. Then, first As dimers detach directly from the surface and hover in the lower bound state above the surface. And finally – like in the case of the $\{10-10\}$ _As1 – a number of As dimers desorb entirely from the surface.

The MnAs nanocluster investigated in this study are grown with metal-organic vapour phase epitaxy (MOVPE), not with MBE. Hence, As_2 and also Mn are not introduced directly into the growth chamber (reactor). Instead, a manganese

Table 4.1. Bond length (d_0 in Å) and binding energy (E_B in eV) of As_2 and As_4 : Comparison between the EAM model, *ab initio* data, and experiment.

As molecule	EAM	B3PW91 ^a	Experiment ^{b,c}
As ₂ (dimer)			
d_0	1.97	2.12	2.10
E_B	4.90	4.05	3.96
As ₄ (tetrahedron)			
d_0	2.45	2.46	2.44
E_B	8.54	10.73	10.21

^a *ab initio* values for both As_2 and As_4 from [78]

^b experimental values for As_2 from [75]

^c experimental values for As_4 from [76]

organometallic precursor – $(\text{CH}_3\text{C}_5\text{H}_4)_2\text{Mn}$ – and arsine – AsH_3 – is transferred to the reactor. During the high temperatures of the growth process (around 850 °C), the precursors are decomposed in gas phase reactions [2–4]. Thus, at this stage As dimers will play a role in the crystallization. Nonetheless, MBE growth of MnAs has also been done [83–86]. However, with such low temperature MBE, only thin film MnAs structures are possible. In both cases a high arsenic pressure is required, since As is volatile and desorbs easily into the gas phase. Again, this proves the consistency with the results of the surface simulations.

In Table 4.1 bond length and binding energy of As_2 and As_4 are given, calculated with the EAM potential and compared to *ab initio*² and experimental values. This explicit comparison reveals a very good structural agreement to experiment. The bond length for As_2 has a relative deviation of 6.2%. With 0.4% the one for As_4 is even significantly smaller. The trend in binding energies³ is well reproduced, relative deviations being 23.7% and 16.4%. This qualitative trend is to be rated even higher when considering the fact that the reference configurations have never been intended for describing As dimers or tetrahedrons. In the reference configurations the As dimer distance has not been taken into account, because in there the minimal As-As interaction is only 2.53 Å. Also, a specific structure of elemental As has not been considered; particularly the explicit structure of an arsenic dimer or tetrahedron is not included. Therefore, it is clearly an extrapolation as the potential predicts properties which are not represented in the reference data. It shows the transferability of the potential in this regard. Consequently, the overall conclusion is that the predicted As dimers on MnAs surfaces are a reasonable result of the simulations.

² Note: the *ab initio* calculations use a different functional (PW91) than the *ab initio* calculation of this work (PBE).

³ The potential energy of the present effective potential does not represent a binding or cohesive energy, since no energies of free atoms were considered during the setup of the reference configurations. That was only done for this calculation by subtracting the energy of isolated atoms for each element from the total potential energy of the corresponding molecule.

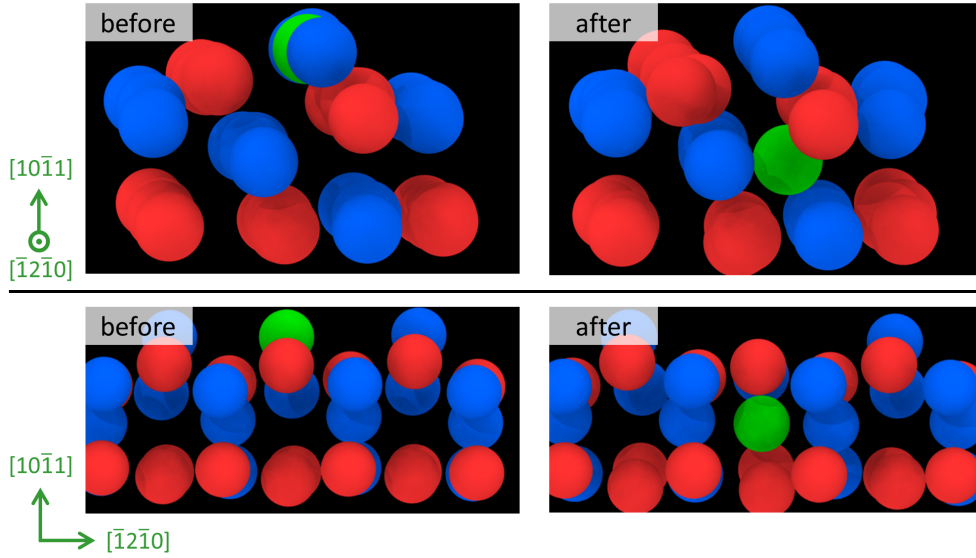


Figure 4.7. Diffusion of one Mn atom (green) from the top layer to an interstitial site in the third layer of the $\{10\text{-}11\}$ _Mn surface: The MD snapshots represent a small section of the simulated structure from the previous stability analysis, with smaller atom radii for better visualization. At the top, the snapshots show the cross section of the surface in direction of the a -axis $[\bar{1}2\bar{1}0]$, before (left) and after (right) the diffusion. The same is displayed at the bottom with the exception that the structure is rotated in the surface plane by 90° .

Mn Interstitials. At the Mn terminated $\{10\text{-}11\}$ surface, Mn atoms of the first layer start diffusing into the substrate and occupy interstitial sites in the third layer. When heating the structure – like it was done for the $\{10\text{-}10\}$ _As2 and $\{0001\}$ _As termination – the diffusion process is accelerated until all Mn atoms of the first layer diffuse into the substrate. Figure 4.7 conveys this process by displaying start and end configuration of the diffusion. The explicit position of the interstitial site is visible as well. Like for the MnAs surface facets and terminations in general, this has not been experimentally investigated yet. However, a similar behavior is described in the literature [2]. Wakatsuki *et al.* report that Mn adatoms on semiconductor surfaces (GaAs) diffuse into underlying layers. This statement suggests that the Mn diffusion at the $\{10\text{-}11\}$ _Mn surface is a reasonable prediction of this study.

4.2 Deposition Simulations of Au on MnAs

Now, after preparing the different surfaces in MD simulations, the main objective of this work – finding out the structure of gold on MnAs – is analyzed. However, considering the surfaces in Figure 4.1, only the {10-10}_As1 surface termination is chosen for the following deposition simulation as a first test. The particular surface has the lowest surface energy and proved to be one of the stablest surfaces during the previous simulations.

4.2.1 Deposition on the {10-10}_As1 Surface Termination

Simulation Settings. From the preceding surface simulations, the surface structure with As1 termination – as seen in the previous paragraph, Figure 4.5 – was used for the deposition simulation. The basic setup for the deposition simulation was the same as those for the surface simulations. Again, the substrate had to be cooled with a thermostat, otherwise the transferred kinetic energy of the gold adatoms would have continuously heated up the substrate. Also, a total shift of the substrate due to the transferred momenta of the adatoms is avoided by fixing the lowest layers of the substrate.⁴

The gold atoms were created 6 nm (60 Å) above the substrate surface with x - and y -positions randomly chosen. Each gold atom has been assigned a velocity value perpendicular to the surface, a value chosen close to the mean thermal velocity⁵ of the melting temperature of gold ($T_{\text{melt}} = 1330$ K). The number of time steps was 6.16 million with a time step size of one femtosecond. Every 200th time step a new gold atom was generated. The last 160 000 steps were used just for relaxation, leading to 30 000 deposited gold atoms in summary. All of this was simulated at room temperature. With an overall computation time of 42 hours, the simulation was performed on 72 cpu cores on a high-performance computing cluster.

When doing deposition simulations in MD, one has to consider the intrinsic limitation concerning the timescale of MD simulations. Because of that limitation, the deposition rates are orders of magnitudes higher than in experiment. The typical time needed for one monolayer to grow in simulations is in the range of nanoseconds. This differs significantly from experiment, where typical growth durations for monolayers are in the range of seconds. Hence, it is important to keep in mind the time limitation when analyzing the results. The best way to approach this problem is to ask how such a high deposition rate influences the simulation results. Or, conversely, does a higher deposition rate in experiment lead to the same results?

⁴ Further rule for deposition simulations: the total mass of the substrate should be larger than the total mass of incoming atoms to avoid a bounce back effect.

⁵ $\bar{v} = \sqrt{\frac{8k_{\text{B}}T}{\pi m}}$

This cannot be answered in general, but several things can be checked. Are the basic simulation results consistent with the experimental context or do the results contradict basic physical rules and mechanisms? When increasing the deposition cycle or increasing the substrate area, does the simulation result change significantly? In the end of next paragraph those questions will be addressed again, when discussing the growth mode of the observed deposition simulation.

Growth Mode. The deposition simulation revealed a specific growth mode of the gold atoms, as it can be seen on the numbered snapshots at the bottom of Figure 4.8. In the beginning the gold atoms form one layer by depositing on the sites where the atoms of the second As layer would have been (1. snapshot). A few gold atoms even replace an As atom of the first layer (substitutional impurity atom)⁶. Then, instead of building a second layer, islands start to grow (2. snapshot), move and coalesce to bigger islands (3. snapshot), until a closed surface structure appears when grain and crystal growths begins (4. snapshot).

This behavior is a well-known growth mode from experiment, first described by Stranski and Krastanov in 1938 [87]. For that reason it is named Stranski-Krastanov growth⁷. The mode consists of two steps. In the beginning the surface adhesive force is stronger than the adatom cohesive force and wetting layers are formed. At some critical layer thickness this relation changes and the adatom-adatom interaction is stronger, which then leads to the island growth in a second step. This critical layer thickness depends on the mismatch of lattice parameters between deposited film and substrate. A greater lattice mismatch triggers a smaller critical layer thickness [88]. Also, the misfit strain at the surface increases significantly with each deposited layer, making it necessary for the system to stop the layer growth at this critical thickness in order to reduce the strain. Typical critical thicknesses range from sub-monolayer coverage to several monolayers [89].

In the present case the lattice mismatch between the MnAs {10-10}_{As1} substrate – including the first deposited gold wetting layer – and a crystalline thin film structure of fcc gold on top of this wetting layer is significant. The lateral symmetry of the one gold wetting layer is governed by the hexagonal lattice parameters a and c , resulting in a rectangular layer pattern with the dimensions of a and c . Such a pattern does not fit to any possible symmetry direction of an fcc gold lattice. The closest, possible direction is the one of the {110} fcc surface, as it has a rectangular pattern. But the in-plane dimensions exhibit a mismatch and the induced strain prevents the continuous growth of a suitable, next gold layer. For that reason, the critical thickness is just one monolayer or even in the sub-monolayer range, when the nucleation of islands starts to relieve the mismatch strain.

Coming back to the earlier mentioned aspect of the high deposition rate, the simulation results show great consistency within the experimental context. As stated in the beginning, the Stranski-Krastanov growth is well-known from experiment.

⁶ The remaining As atoms of such an exchange are considerably free and diffuse always to the top of the current deposited surface structure.

⁷ It is also known by ‘layer-plus-island growth’.

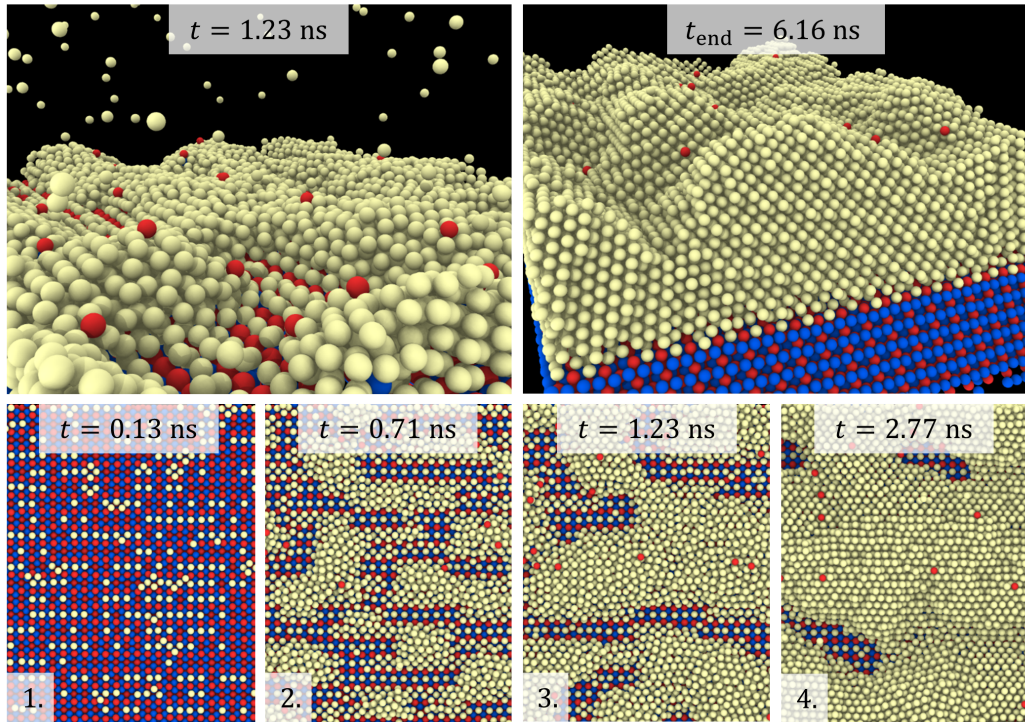


Figure 4.8. Snapshots of the deposition simulation at various time steps: The two pictures at top are side views of the substrate during the deposition process (left) and at the end of the whole simulation run (right). The four pictures at the bottom are top views of the substrate and convey the different steps of the observed Stranski-Krastanov growth, which is 1. formation of the wetting layer, 2. island growth, 3. coalescence of islands, and 4. grain and crystal growth.

There are several studies which show the different stages – as seen in Figure 4.8 – with the help of atomic force microscopy (AFM). For example, in one of the earlier mentioned works on MnAs thin film growth, the surface morphology of the MnAs films was studied *ex situ* with an AFM [84]. There is even an *in situ* study of gold on gold growth, where the deposition is continuously scanned with an AFM during the process and visualized with a video of AFM images later [90, 91]. Next to this general consistency concerning the growth mode, test runs with lower deposition rates and substrate dimensions did not hint to a different growth mode of the deposition. One could raise the question that the islands are growing, because the Au atoms have no time to relax. But long simulation runs of only the grown islands show that the island do not dissolve into a second layer. Hence, the adatoms have enough time to relax. Furthermore, the following analysis of the crystal structure reveals no contradiction to basic physical rules and mechanisms as well, supporting the conclusion that the presented deposition simulation produces meaningful results, despite high deposition rates.

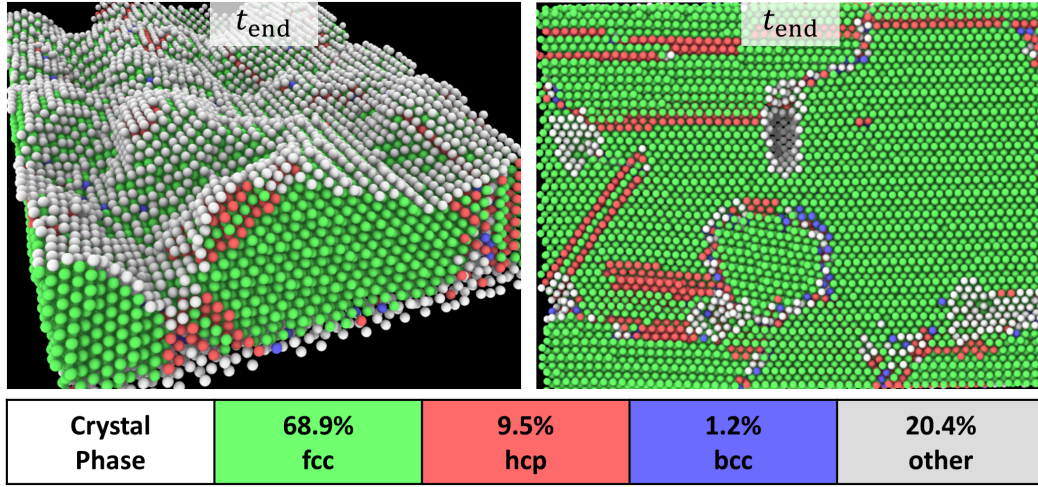


Figure 4.9. Bond-angle analysis of the grown gold structure: The percentage values at the bottom give the fractions of each crystal phase the deposited structure consists of, determined with the software tool *ovito* [73]. By considering also the fraction of 9.5% hexagonal closed packed phase (hcp) – representing fcc stacking faults and twin boundaries – nearly 80% of the analyzed structure belongs to the fcc phase. The surface atoms and the atoms of the interface region make for the 20.4% of unassigned atoms. The left snapshot is the same from Figure 4.8 (top right), but now with the bond-angle analysis. The right snapshot is a cross section parallel to the substrate. There, the stacking faults and different grains are visible.

4.2.2 Analysis of the Grown Gold Structure

Crystal Structure. After the deposition simulation the grown gold structure has been analyzed with a bond-angle analysis (see Figure 4.9). A bond-angle analysis assigns every atom of the structure to a crystal phase by comparing the local environment to the known structures of the cubic crystal systems. The analysis shows that the gold grows as an fcc crystal. Nearly 80% of the analyzed structure belongs to the fcc phase. The 9.5% hexagonal closed packed phase (hcp) phase can be misleading, since this percentage stems from the stacking faults and twin boundaries of the fcc crystal. Hence, the hcp fraction is included in those 80%. The 1.2% body centered cubic phase (bcc) is only assigned for local atoms, pointing to some possible local defects in the fcc structure. The surface atoms and the atoms of the interface region do not belong to any phase, resulting in a fraction of 20% for that group (other).

Historically, a stacking fault produced by vacancy agglomeration (one layer missing in the stacking sequence) is called intrinsic stacking fault. On the other hand, a stacking fault produced by interstitial agglomeration (one layer additional to the stacking sequence) is called extrinsic stacking fault [92]. Both types of stacking faults occur in the grown gold structure and are displayed in Figure 4.10, next to a combination of those stacking faults as well as a twin boundary. Twin boundaries do not count as stacking faults. On the contrary, due to the mirroring at the boundary they avoid stacking faults and the structure keeps the bond lengths and angles. By looking at the labelling of stacked layers in Figure 4.10, it is also evident why the

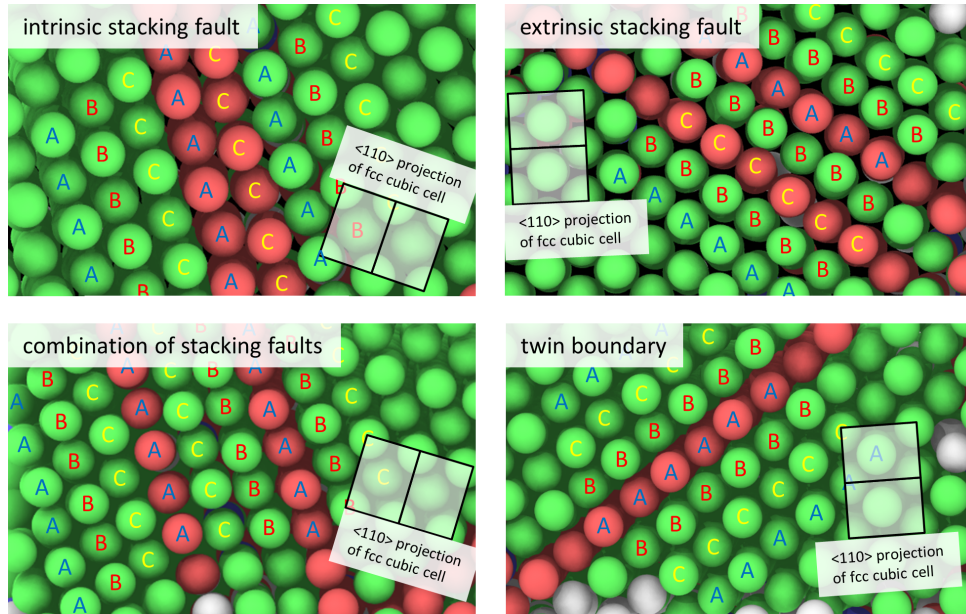


Figure 4.10. Stacking faults and twin boundaries seen from the $\langle 110 \rangle$ cubic direction of the grown fcc gold: The snapshot in the top left corner shows an intrinsic stacking fault. One B-layer is missing, changing the stacking sequence from standard fcc ABCABCABC to ABCACABC (bold letters highlight the faulty part of the stacking sequence). On the upper right snapshot, one B-layer is additional to the original stacking, leading to the sequence of an extrinsic stacking fault, ABCBABC. At the lower left corner, a combination of both type is present, since a B-layer is removed and added at the same time. This is basically a swapping of the C- and B-layer in the middle, resulting in the sequence ABCACBABC. It could be also viewed as two successive twin boundaries. Such a twin boundary is shown at the lower right, as the sequence ACBABCA is mirrored at the middle A-layer, avoiding the stacking fault and therefore keeping the bond lengths and angles of the fcc structure.

bond-angle analysis assigns certain atom layers to an hcp phase. Since those layers are surrounded by identical layers due to stacking faults or twin boundaries, they appear as locally hcp layers (local stacking sequence ABA instead of ABC).

One of the reasons for the building of such defects is clearly the strain mentioned earlier in the context of the growth mode. As there is a considerable high strain in the structure because of the lattice mismatch, the stacking faults reduce this strain. Temporarily “undesired” growth conditions like the local thermodynamic situation may also prevent perfect fcc growth, but in this case stacking faults and twin boundaries result mainly from the way how the gold grows on the surface, developing a certain crystal orientation towards the surface. In the following paragraph this crystal orientation will be discussed in detail.

Crystal Orientation. Looking at the exact orientation of the gold structure leads to a more quantitative description of the grown fcc crystal. In Figure 4.11 the orientation is implied by drawing the $\langle 110 \rangle$ projection of the fcc unit cell and the corresponding lattice directions. Two basic orientations of the unit cell can be

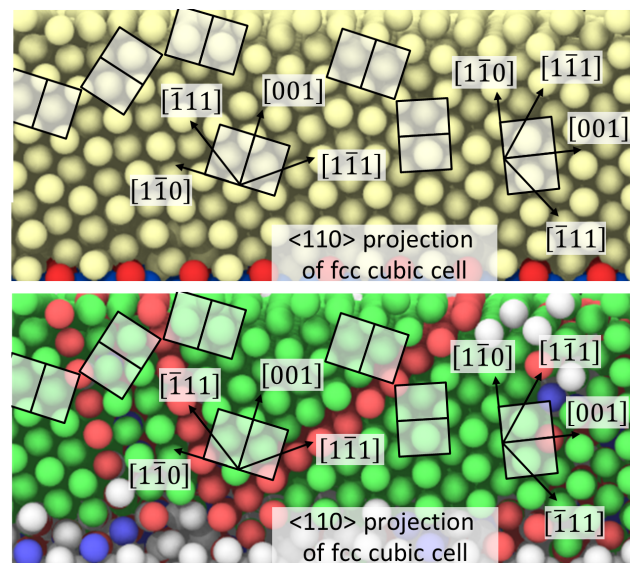


Figure 4.11. Crystal orientation of the grown gold: At the top, the cross-section view of the substrate in the $\langle 110 \rangle$ direction of the fcc crystal. At the bottom, the same snapshot, but this time the results of the bond-angle analysis are included. It can be seen from the indicated fcc cubic cells in $\langle 110 \rangle$ projection that the unit cells are tilted upright, standing with one corner of the cube on the MnAs substrate. There are two principle types of orientation. The cube of the unit cell can have a relative low angle towards the surface (left) or a quite steep angle (right). The transition between those orientations takes place at a twin boundary, which is most evident in the the lower snapshot with the bond-angle analysis.

determined. Both of them are tilted upright and stay on one corner of the cube with respect to the substrate. Additionally, Figure 4.11 shows that the stacking faults and twin boundaries originate at the interface of the MnAs substrate and the grown gold. From there, they continue to spread out through the grown structure. This relationship between the crystal defects and the interface is closely connected to the question of which specific orientation will be formed during the growth. To overcome the lattice mismatch at the interface, defects like edge dislocations are created, which lead to the stacking faults. But also the fact that the islands grow initially separately from each other results in different crystal orientations, since the orientation of the islands is independent from each other. And when the islands coalesce there is a higher probability for stacking faults or twin boundaries to occur at the boundary of those islands.

An analysis of the first gold layer – the wetting layer – is crucial to understand the beginning growth process and the reasons for the resulting crystal orientations of the grown structure. Figure 4.12 displays the first layer at the beginning and at the end of the simulation. It is also viewed from two different directions. The figure shows how the original form of the layer – the gold atoms taking the positions of the next As layer – changes over the course of the simulation. The rows of gold atoms in the $[0001]$ direction are distorted, since further gold atoms are added to the first layer.

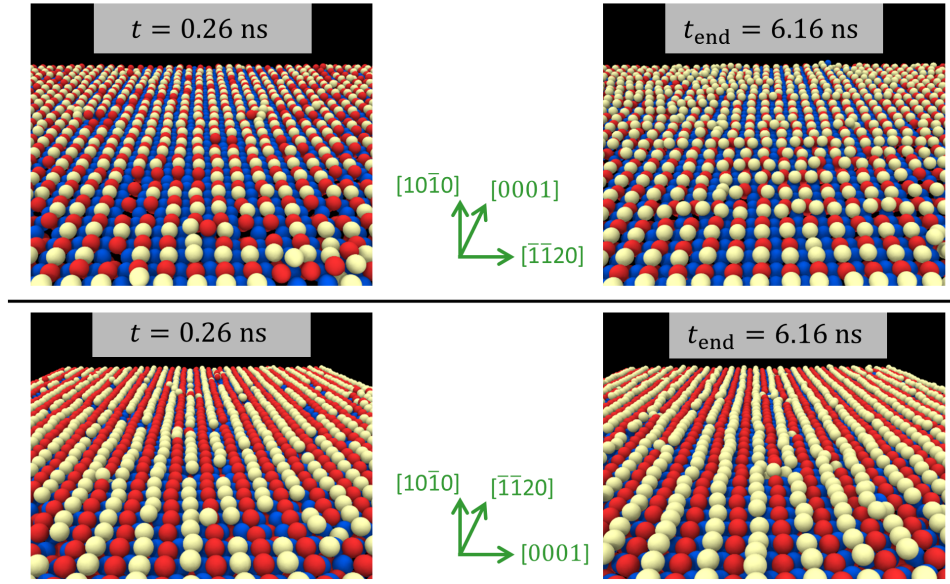


Figure 4.12. The first layer of gold at the beginning and at the end of the simulation: The first layer is viewed alongside the $[0001]$ and $[\bar{1}\bar{1}20]$ directions (c - and a -axis) of the MnAs cell, shown in the upper and lower snapshots respectively. Other deposited gold atoms above the first layers are not visible. From the snapshots on the left (first layer at the beginning), it is evident that the gold atoms deposit at the atom sites of the next As layer. The structure seems to be same at the end of the simulation, when looking at the first layer only in the $[\bar{1}\bar{1}20]$ direction. However, the perspective in the $[0001]$ direction reveals that the structure significantly changed.

The background is now that the observed fcc structure would not have been possible if the first layer kept its original form. The gold atoms take the position of the next As layer. Hence, they build a rectangular pattern at first. This is highlighted by the green rectangles in the upper right snapshot of Figure 4.13. The rectangles have the dimensions of the MnAs hexagonal lattice – a and c – but since the lattice mismatch between gold and those MnAs lattice dimensions is significant, islands start to grow instead of a second layer. The islands grow in fcc, and with that, imprinting the fcc structure on the wetting layer. The original positions of the gold atoms are changed and – most importantly – gold atoms are added to the first layer. From the four gold rows seen in the lower right snapshot of Figure 4.13, there are two rows where the number of gold atoms doubles. This leads to the indicated triangle pattern, where the small side of the triangle has the length of the smallest distance in the gold fcc structure, $a_{\text{Au}}/\sqrt{2}$. Such a pattern is necessary for the observed structure of tilted fcc cubes, since the corner points of the cubes sit diagonally shifted behind one another.

The additional gold atoms in the first layer are possible, because the energy landscape of the particular MnAs surface has a convenient shape. On the left side of Figure 4.13, the potential energy of one gold atom above the MnAs surface is shown. The potential minima – elongated in the $[\bar{1}\bar{1}20]$ direction of the substrate – make

it possible for two gold atoms to fit in the same minima. However, as this is not the ideal pattern, the whole structure is under a lot of strain. Consequently, this results in the mentioned stacking faults and different orientations of the fcc structure. Furthermore, the triangle pattern is not perfectly formed throughout the layer. For example, there is the gold atom which is labeled in Figure 4.13 as a substitutional impurity atom. The gold atom took the place of an As atom of the first layer of the substrate. Those kind of defects and dislocations break the pattern and, therefore, avoid also the perfect fcc growth of the gold on the $\{10\text{-}10\}$ _As1 MnAs surface.

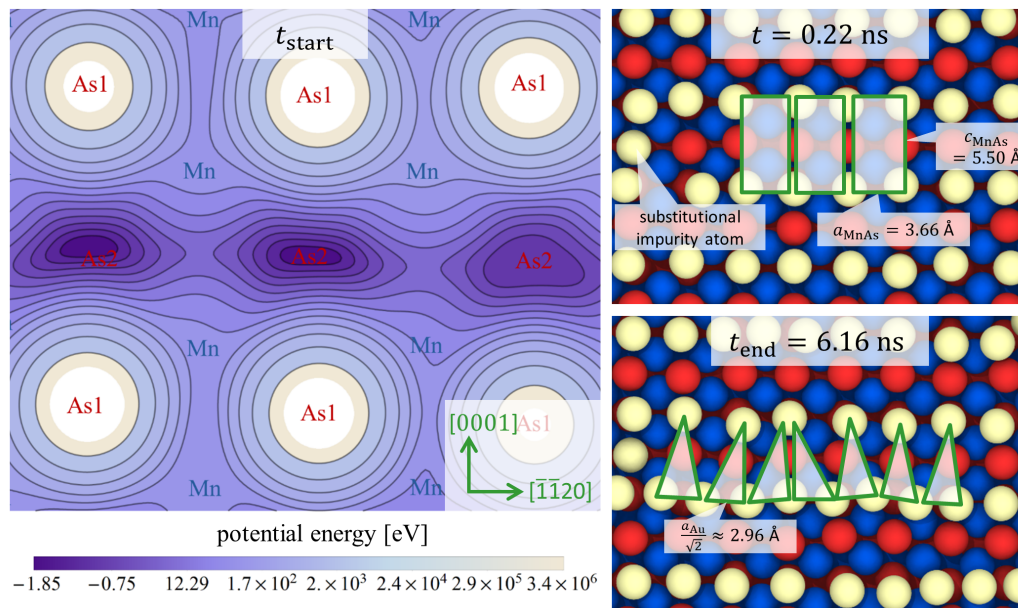


Figure 4.13. Further analysis of the first layer in top view: On the left, the energy landscape of one gold atom being 0.35 Å above the MnAs substrate is shown, which is the situation at the start of the simulation. The labels drawn in the landscape are the first three layers of the $\{10\text{-}10\}$ _As1 surface. It is evident from the energy landscape that the gold atoms deposit at the energy minima positioned in the middle of the four Mn atoms of the second MnAs layer. This is visible in the upper right snapshot. Like mentioned before, the gold atoms take the dimensions of the MnAs substrate and form a rectangular pattern for the first layer. However, the pattern changes to a sort of triangular pattern at the end of the simulation, as seen in the lower right snapshot. Since the energy minima are elongated in the $[\bar{1}\bar{1}20]$ direction of the substrate, two gold atoms fit in those minima, leading to the triangle patterns.

5 Conclusions

Summary. Within the framework of this thesis, an EAM potential for the MnAs/Au interface system has been generated and successfully applied to investigate the main objective of the thesis at hand: performing a Molecular Dynamics simulation of gold growth on MnAs and analyzing the grown gold structure. Further, this work provides a new effective potential – not only for MD simulations of MnAs/Au interface systems – but also for MnAs bulk systems. Both systems have never been described with MD simulations and, consequently, no effective potential has been developed for those systems until now.

Force Matching (FM) – the method of fitting a potential model to *ab initio* data – offers the possibility to create effective potentials for MD simulations and keep the predictive power of *ab initio* calculations. However, generating the needed MnAs/Au potential showed that FM is by far no simple black box producing potentials at the push of a button. For this reason detailed descriptions of the explicit steps and fitting strategies have been given in this work. The fitting process is an iterative optimization cycle with a various number of parameters, which are very different in nature. The present work summarizes those parameters and discusses their different nature and roles during the optimization. There is no general systematic strategy to optimize the parameters, but the potential generation revealed some guidelines and rules. One of the important lessons is the fact that there is some sort of hierarchy within the parameters, meaning some parameters are more important than others at certain stages of the optimization. Another helpful advice concerns the early use of the potential validation, which happens after the actual optimization run. Including validation results as soon as possible helps steering the fitting process from the start.

Validating the potential is an important step in creating effective potentials. The comparison of potential properties to data not included in the fitting database proves the reliability of the potential. Comparing lattice constants and potential energy of the unit cells – derived from the MnAs/Au potential – to the corresponding *ab initio* values reveals an excellent structural agreement, with relative deviations being lower than at least 0.2%. The corresponding experimental lattice constants show a typical relative deviation to *ab initio* lattice constants of a few percent. The comparison of the elastic constants to the *ab initio* counterparts reveals a mean relative deviation of 5%. For the experimental counterparts, the trend – meaning the relative ordering – is reproduced. However, the comparison is problematic in case of MnAs,

since the experimental measurements were performed in the paramagnetic state and not in the ferromagnetic state. The relative deviations of the surface energies to *ab initio* values are at least lower than 12%, two even less than 1%. For some surface terminations, the surface energies are predictions, as the corresponding reference bulk structures – needed for calculating the surface energies – cannot be represented by periodic cells. Hence, it was not possible to perform *ab initio* calculations for comparisons in these cases. Experimental values of surface energies were not available.

With the developed potential, MD simulations of different surface facets and terminations were performed to find the most stable surface structures for the deposition simulations. The exact surface terminations are also not known from experiment. In the course of stability tests, two interesting effects occurred. At two surface terminations As dimers are formed at the surface and desorbing occasionally from the latter. At a Mn terminated surface Mn atoms diffuse into the substrate, occupying interstitial sites of the substrate. Both effects – As dimers on surfaces and Mn diffusion into substrates – are observed in other research studies as well, including experimental studies. In case of As dimers, bond length and energy have been compared to *ab initio* calculations and experimental measurements.

The surface which proved to be the stablest during the surface simulation was picked for the final deposition simulations of gold on MnAs. The deposition simulations on the specific surface reveal a growth mode known as the Stranski-Krastanov growth or ‘layer-plus-island growth’. After forming a wetting layer of one monolayer thickness, the deposited gold atoms grow mainly in an fcc structure with several stacking faults and twin boundaries. Those crystal defects stem primarily from the lattice mismatch between the gold and the MnAs surface, which is also the reason for the beginning of island growth after the formation of one monolayer. The particular form of the wetting layer has been investigated in depth, since it plays an important role for the specific structure and orientation of the grown fcc gold. The investigation shows that the fcc cubic unit cells are tilted upright and stay on one corner of the cube with respect to the substrate.

Outlook. In conclusion, with this work and the resulting effective potential the crucial groundwork for future calculations has been done. Besides the generation of the potential, the thesis also shows the reliability of the latter. The simulation of any physical situation dealing with bulk structures of MnAs or Au as well as MnAs/Au interface systems should be possible as long as the physical situation is close to the used reference data of the created potential. The potential may perform well in other situations, but care must be taken. In such cases validation tests concerning the new situation is advisable.

In the explicit case of the deposition of gold on MnAs, further investigations can be pursued. The deposition simulation of gold on the $\{10\bar{1}0\}$ _As1 MnAs surface was a first test. Like mentioned in the introduction, determining the exact structure of gold on MnAs is a necessary step for transport calculations through a MnAs/Au/MnAs layer. With further analysis it should be possible to deduce a

suitable structure for such calculations. Investigating different parameters of the deposition simulations – like the substrate temperature – or the strain and dislocations via Burger vectors [92] should offer a deeper understanding of the gold structure and growth mechanism. Gold deposition on the other MnAs surfaces has yet to be analyzed. Also, applying the potential within the so-called adaptive kinetic Monte Carlo (akMC) [93, 94] method is an option to extend the time scale of the deposition simulation. By using this method the simulation is split into two parts. MD is used to simulate the adsorption process while akMC handles the time evolution between those adsorptions.

Besides this continuing research of gold deposition simulations, there are other interesting questions for which the developed potential can be applied. For example, in regard of MnAs surface facets and their formation, the simulation of MnAs growth might give some helpful insight. Drautz et al. [21, 81] simulated the growth of GaAs with MD by inserting Ga atoms and As dimers at different ratios. Such a growth simulation should be also possible for MnAs. Another example are surface reconstructions at epitaxial MnAs films grown in the $\langle 0001 \rangle$ direction, which have been observed in [83]. Such surface reconstructions can be investigated with the potential as well. The last example concerns the arsenic dimers and their adsorption behavior. Murdick et al. analyzed quantitatively the sticking rates and different binding states of the dimers on GaAs [80]. This can also be done with the As dimers on MnAs.

Those examples give an idea of the variety of different applications the potential can be used for. Again, since effective potentials provide in general the interaction in MD simulations, the availability of such potentials for new material systems – like it is the case for the MnAs/Au system – opens up possibilities to a wide range of future research.

Appendix

MnAs/Au EAM potential

Table 1. Fitted spline knots: the pair functions – part I

<i>i</i>	Mn-Mn		Mn-As		Mn-Au	
	<i>r</i> Å	$\phi_{11}(r)$ eV	<i>r</i> Å	$\phi_{12}(r)$ eV	<i>r</i> Å	$\phi_{13}(r)$ eV
1	2.2000000	0.1909667	2.1000000	0.2230760	1.8219600	5.2972670
2	2.4526316	-0.1562470	2.3578947	-0.2586972	2.2300000	0.3610386
3	2.7052632	-0.2630174	2.6157895	-0.2772406	2.4811765	-0.2149425
4	2.9578947	-0.2497912	2.8736842	-0.1695126	2.7323529	-0.2954656
5	3.2105263	-0.2043759	3.1315789	-0.0587907	2.9835294	-0.2564881
6	3.4631579	-0.1611091	3.3894737	0.0134258	3.2347059	-0.2168010
7	3.7157895	-0.1297717	3.6473684	0.0198989	3.4858824	-0.1858822
8	3.9684211	-0.1095001	3.9052632	0.0019406	3.7370588	-0.1481191
9	4.2210526	-0.0955310	4.1631579	-0.0098992	3.9882353	-0.1005256
10	4.4736842	-0.0808108	4.4210526	-0.0123951	4.2394118	-0.0643107
11	4.7263158	-0.0622304	4.6789474	-0.0092053	4.4905882	-0.0399483
12	4.9789474	-0.0428311	4.9368421	-0.0063731	4.7417647	-0.0185665
13	5.2315789	-0.0283612	5.1947368	-0.0051965	4.9929412	-0.0047006
14	5.4842105	-0.0212414	5.4526316	-0.0054328	5.2441176	0.0000000
15	5.7368421	-0.0144647	5.7105263	-0.0064467		
16	5.9894737	-0.0079313	5.9684211	-0.0077240		
17	6.2421053	-0.0042519	6.2263158	-0.0074236		
18	6.4947368	-0.0027209	6.4842105	-0.0064168		
19	6.7473684	-0.0014654	6.7421053	-0.0027790		
20	7.0000000	0.0000000	7.0000000	0.0000000		
	$\phi'_{11}(r_1)=$	$\phi'_{11}(r_{20})=$	$\phi'_{12}(r_1)=$	$\phi'_{12}(r_{20})=$	$\phi'_{13}(r_1)=$	$\phi'_{13}(r_{14})=$
	-2.0897755	0.0000000	-3.6269510	0.0000000	-22.3509534	0.0000000

Table 2. Fitted spline knots: the pair functions – part II

i	As-As		As-Au		Au-Au	
	r Å	$\phi_{22}(r)$ eV	r Å	$\phi_{23}(r)$ eV	r Å	$\phi_{33}(r)$ eV
1	2.5300000	0.7451029	1.7048000	9.4147916	1.6700000	17.3441935
2	2.7652632	0.5688803	1.9600000	3.1861000	1.9189474	7.7548944
3	3.0005263	0.4109402	2.2270588	1.0146358	2.1678947	2.7004053
4	3.2357895	0.2831523	2.4941176	0.3634111	2.4168421	0.8145668
5	3.4710526	0.1809801	2.7611765	0.1946045	2.6657895	0.1917274
6	3.7063158	0.1057746	3.0282353	0.1367242	2.9147368	-0.0133208
7	3.9415789	0.0576829	3.2952941	0.0901886	3.1636842	-0.0716446
8	4.1768421	0.0348080	3.5623529	0.0454760	3.4126316	-0.0820686
9	4.4121053	0.0255996	3.8294118	0.0105528	3.6615789	-0.0911388
10	4.6473684	0.0109333	4.0964706	0.0000000	3.9105263	-0.0952499
11	4.8826316	-0.0099149			4.1594737	-0.0868812
12	5.1178947	-0.0186470			4.4084211	-0.0676554
13	5.3531579	-0.0151856			4.6573684	-0.0417379
14	5.5884211	-0.0141592			4.9063158	-0.0226049
15	5.8236842	-0.0159378			5.1552632	-0.0104941
16	6.0589474	-0.0167367			5.4042105	-0.0028562
17	6.2942105	-0.0147992			5.6531579	0.0031786
18	6.5294737	-0.0097173			5.9021053	0.0032866
19	6.7647368	-0.0031646			6.1510526	0.0005293
20	7.0000000	0.0000000			6.4000000	0.0000000
	$\phi'_{22}(r_1)=$	$\phi'_{22}(r_{20})=$	$\phi'_{23}(r_1)=$	$\phi'_{23}(r_{10})=$	$\phi''_{33}(r_1)=$	$\phi'_{33}(r_{20})=$
	-0.9027886	0.0000000	-37.0869443	0.0000000	0.0000000	0.0000000

Table 3. Fitted spline knots: the transfer functions

i	r Å	$\rho_{\text{Mn}}(r)$ arb.unit.	r Å	$\rho_{\text{As}}(r)$ arb.unit.	r Å	$\rho_{\text{Au}}(r)$ arb.unit.
1	2.1000000	0.1140399	2.1000000	0.2380951	1.6700000	0.4629435
2	2.3578947	0.0798480	2.3578947	0.1355340	1.9189474	0.1922209
3	2.6157895	0.0588453	2.6157895	0.0699135	2.1678947	0.1213196
4	2.8736842	0.0426584	2.8736842	0.0364299	2.4168421	0.0935327
5	3.1315789	0.0252335	3.1315789	0.0172917	2.6657895	0.0637170
6	3.3894737	0.0088171	3.3894737	0.0082482	2.9147368	0.0363665
7	3.6473684	0.0022950	3.6473684	0.0039220	3.1636842	0.0188351
8	3.9052632	-0.0017430	3.9052632	0.0023127	3.4126316	0.0122440
9	4.1631579	-0.0025544	4.1631579	0.0025354	3.6615789	0.0090895
10	4.4210526	-0.0021374	4.4210526	-0.0000494	3.9105263	0.0019440
11	4.6789474	-0.0006423	4.6789474	0.0000000	4.1594737	0.0000000
12	4.9368421	0.0000000				
	$\rho'_{\text{Mn}}(r_1)=$	$\rho'_{\text{Mn}}(r_{12})=$	$\rho'_{\text{As}}(r_1)=$	$\rho'_{\text{As}}(r_{11})=$	$\rho''_{\text{Au}}(r_1)=$	$\rho''_{\text{Au}}(r_{11})=$
	-0.1689742	0.0000000	-0.5651179	0.0000000	0.0000000	0.0000000

Table 4. Fitted spline knots: the embedding functions

i	n arb.unit.	$U_{\text{Mn}}(n)$ eV	n arb.unit.	$U_{\text{As}}(n)$ eV	n arb.unit.	$U_{\text{Au}}(n)$ eV
1	0.1082540	-5.8004128	0.0837536	-3.9210478	0.0975431	-1.8580498
2	0.2356463	-5.7385859	0.1685326	-5.0671553	0.2103502	-2.2818910
3	0.3630385	-5.6617462	0.2533117	-5.6749254	0.3231574	-2.5523032
4	0.4904308	-5.6195953	0.3380907	-5.9229799	0.4359645	-2.7135417
5	0.6178231	-5.6212328	0.4228698	-5.9293174	0.5487716	-2.7668005
6	0.7452154	-5.6867491	0.5076489	-5.8077803	0.6615787	-2.7150242
7	0.8726077	-5.8121850	0.5924279	-5.5481988	0.7743858	-2.5516436
8	1.0000000	-6.0144097	0.6772070	-5.1542209	0.8871929	-2.2552997
9					1.0000000	-1.8473042
	$U'_{\text{Mn}}(n_1)=$	$U'_{\text{Mn}}(n_8)=$	$U'_{\text{As}}(n_1)=$	$U'_{\text{As}}(n_8)=$	$U''_{\text{Au}}(n_1)=$	$U''_{\text{Au}}(n_9)=$
	0.1781385	-1.7838855	-15.8409234	5.3750200	0.0000000	0.0000000

Bibliography

- [1] H. Okamoto. ‘The As-Mn (Arsenic-Manganese) system’. In: *Bulletin of Alloy Phase Diagrams* 10.5 (1989), pp. 549–554. DOI: 10.1007/BF02882414.
- [2] T. Wakatsuki, S. Hara, S. Ito, D. Kawamura and T. Fukui. ‘Growth Direction Control of Ferromagnetic MnAs Grown by Selective-Area Metal–Organic Vapor Phase Epitaxy’. In: *Japanese Journal of Applied Physics* 48.4S (2009), p. 04C137. DOI: 10.1143/jjap.48.04c137.
- [3] S. Hara, D. Kawamura, H. Iguchi, J. Motohisa and T. Fukui. ‘Self-assembly and selective-area formation of ferromagnetic MnAs nanoclusters on lattice-mismatched semiconductor surfaces by MOVPE’. In: *Journal of Crystal Growth* 310.7 (2008), pp. 2390–2394. DOI: 10.1016/j.jcrysgro.2007.12.026.
- [4] M. T. Elm. ‘Tuning the magnetic interactions in GaAs:Mn/MnAs hybrid structures by controlling shape and position of MnAs nanoclusters’. PhD thesis. Justus-Liebig-Universität Giessen, 2010. URL: <http://geb.uni-giessen.de/geb/volltexte/2010/7896/>.
- [5] H.-A. K. von Nidda, T. Kurz, A. Loidl, T. Hartmann, P. J. Klar, W. Heimbrodt, M. Lampalzer, K. Volz and W. Stolz. ‘Tuning the magnetic properties of GaAs:Mn/MnAs hybrids via the MnAs cluster shape’. In: *Journal of Physics: Condensed Matter* 18.26 (2006), p. 6071. URL: <http://stacks.iop.org/0953-8984/18/i=26/a=025>.
- [6] P. Grünberg, R. Schreiber, Y. Pang, M. Brodsky and H. Sowers. ‘Layered magnetic-structures - evidence for antiferromagnetic coupling of fe layers across cr interlayers’. In: *Physical review letters* 57.19 (1986), pp. 2442–2445. DOI: 10.1103/physrevlett.57.2442.
- [7] M. Baibich, J. Broto, A. Fert, F. Vandau, F. Petroff, P. Eitenne, G. Creuzet, A. Friedrich and J. Chazelas. ‘Giant magnetoresistance of (001)fe/(001) cr magnetic superlattices’. In: *Physical review letters* 61.21 (1988), pp. 2472–2475. DOI: 10.1103/physrevlett.61.2472.
- [8] M. Julliere. ‘Tunneling between ferromagnetic films’. In: *Physics Letters A* 54.3 (1975), pp. 225–226. DOI: 10.1016/0375-9601(75)90174-7.
- [9] G. A. Prinz. ‘Magnetoelectronics’. In: *Science* 282.5394 (1998), pp. 1660–1663. DOI: 10.1126/science.282.5394.1660.

- [10] T. Perez and C. De Rose. *Non-Volatile Memory: Emerging Technologies And Their Impacts on Memory Systems*. 2010. DOI: 10.13140/RG.2.1.3037.6486.
- [11] http://gerardnico.com/wiki/data_storage/ram, retrieved on 05-Aug-2016.
- [12] R. Sbiaa, H. Meng and S. N. Piramanayagam. ‘Materials with perpendicular magnetic anisotropy for magnetic random access memory’. In: *physica status solidi (RRL) – Rapid Research Letters* 5.12 (2011), pp. 413–419. DOI: 10.1002/pssr.201105420.
- [13] G. A. Prinz. ‘Magnetoelectronics applications’. In: *Journal of Magnetism and Magnetic Materials* 200.1–3 (1999), pp. 57–68. DOI: 10.1016/S0304-8853(99)00335-2.
- [14] D. Ralph and M. Stiles. ‘Spin transfer torques’. In: *Journal of Magnetism and Magnetic Materials* 320.7 (2008), pp. 1190–1216. DOI: 10.1016/j.jmmm.2007.12.019.
- [15] J. J. Nowak, R. P. Robertazzi, J. Z. Sun, G. Hu, J.-H. Park, J. Lee, A. J. Annunziata, G. P. Lauer, R. Kothandaraman, E. J. O. Sullivan, P. L. Trouilloud, Y. Kim and D. C. Worledge. ‘Dependence of Voltage and Size on Write Error Rates in Spin-Transfer Torque Magnetic Random-Access Memory’. In: *IEEE Magnetism Letters* 7 (2016), pp. 1–4. DOI: 10.1109/lmag.2016.2539256.
- [16] M. T. Elm. *private communication*.
- [17] M. Fischer, M. T. Elm, S. Sakita, S. Hara and P. J. Klar. ‘Magnetoresistance effects and spin-valve like behavior of an arrangement of two MnAs nanoclusters’. In: *Applied Physics Letters* 106.3, 032401 (2015). DOI: 10.1063/1.4906036.
- [18] C. Heiliger, M. Czerner, P. J. Klar and S. Hara. ‘Magnetic Sensor Devices Based on Ordered Planar Arrangements of MnAs Nanocluster’. In: *IEEE Trans. Magn.* 46.6 (June 2010), pp. 1702–1704. DOI: 10.1109/tmag.2010.2041194.
- [19] N. Levanov, V. Stepanyuk, O. Trushin and K. Kokko. ‘Molecular dynamics simulation of Co thin films growth on Cu(001)’. In: *Surface Science* 400 (1998), pp. 54–62. DOI: 10.1016/s0039-6028(97)00841-8.
- [20] K. Kadau. ‘Molekulardynamik-Simulationen von strukturellen Phasenumwandlungen in Festkörpern, Nanopartikeln und ultradünnen Filmen’. PhD thesis. Gesamthochschule Duisburg, 2001. URL: <http://purl.oclc.org/NET/duett-05252001-103521>.
- [21] R. Drautz, X. Zhou, D. Murdick, B. Gillespie, H. Wadley and D. Pettifor. ‘Analytic bond-order potentials for modelling the growth of semiconductor thin films’. In: *Progress in Materials Science* 52.2–3 (2007). Modelling electrons and atoms for materials science, pp. 196–229. DOI: 10.1016/j.pmatsci.2006.10.013.

- [22] X. W. Zhou, J. J. Chavez, S. Almeida and D. Zubia. ‘Understanding misfit strain releasing mechanisms via molecular dynamics simulations of CdTe growth on {112}zinc-blende CdS’. In: *J. Appl. Phys.* 120.4 (2016), p. 045304. DOI: 10.1063/1.4959609.
- [23] J. J. Chavez, D. K. Ward, B. M. Wong, F. P. Doty, J. L. Cruz-Campa, G. N. Nielson, V. P. Gupta, D. Zubia, J. McClure and X. W. Zhou. ‘Defect formation dynamics during CdTe overlayer growth’. In: *Phys. Rev. B* 85.24 (2012). DOI: 10.1103/physrevb.85.245316.
- [24] D.-P. Song, Y.-C. Liang, M.-J. Chen and Q.-S. Bai. ‘Molecular dynamics study on surface structure and surface energy of rutile TiO₂ (110)’. In: *Applied Surface Science* 255.11 (2009), pp. 5702–5708. DOI: 10.1016/j.apsusc.2008.12.062.
- [25] B. J. Alder and T. E. Wainwright. ‘Studies in Molecular Dynamics. I. General Method’. In: *J. Chem. Phys.* 31 (Aug. 1959), pp. 459–466. DOI: 10.1063/1.1730376.
- [26] G. Czycholl. *Theoretische Festkörperphysik*. Springer Berlin Heidelberg, 14th Dec. 2007. URL: http://www.ebook.de/de/product/19291990/gerd_czycholl_theoretische_festkoerperphysik.html.
- [27] R. Hentschke, E. Aydt, B. Fodi and E. Stöckelmann. *Molekulares Modellieren mit Kraftfeldern - Einführung in die Theorie und Praxis der Computersimulation molekularer Systeme*. 2004. URL: http://www.materials.uni-wuppertal.de/skripten/skript_modellierung/molmodell.pdf.
- [28] M. Griebel, S. Knapek and G. Zumbusch. *Numerical Simulation in Molecular Dynamics: Numerics, Algorithms, Parallelization, Applications*. 1st. Springer Publishing Company, Incorporated, 2007. ISBN: 3540680942, 9783540680949. URL: <http://www.springer.com/us/book/9783540680949>.
- [29] H. S. Walter Greiner Ludwig Neise. *Thermodynamics and Statistical Mechanics*. Springer, 14th Nov. 2001. 480 Seiten. ISBN: 0387942998. URL: http://www.ebook.de/de/product/1321342/walter_greiner_ludwig_neise_horst_stoecker_thermodynamics_and_statistical_mechanics.html.
- [30] N. Hairer and Wanner. *Solving Ordinary Differential Equations I*. Springer Berlin Heidelberg, 1993. DOI: 10.1007/978-3-540-78862-1.
- [31] M. P. Allen. ‘Introduction to Molecular Dynamics Simulation’. In: *Computing* 23.2 (2004). Ed. by N. Attig, K. Binder, H. Grubmüller and K. Kremer, p. 128. URL: <http://wwwabi.snv.jussieu.fr/jompo/Public/PSF/IntroductionMolecularDynamics.pdf>.

- [32] G. Sutmann. ‘Molecular Dynamics - Vision and Reality’. In: *Computational Nanoscience: Do It Yourself*. Eds. J. Grotendorst, S. Blügel, and A. Muramatsu. NIC-series 31 (2006). retrieved on 05-Aug-2016, pp. 159–187. URL: <http://juser.fz-juelich.de/record/51140/files/FZJ-2014-02215.pdf>.
- [33] D. Frenkel and B. Smit. *Understanding Molecular Simulation*. Ed. by A. Press. 2001. URL: http://www.acmm.nl/molstim/frenkel_smit/.
- [34] F. Ercolessi, M. Parrinello and E. Tosatti. ‘Simulation of gold in the glue model’. In: *Philosophical Magazine A-Physics of condensed matter structure defects and mechanical properties* 58.1 (1988), pp. 213–226. DOI: 10.1080/01418618808205184.
- [35] M. Finnis and J. Sinclair. ‘A simple empirical N-Body Potentials for transition-metals’. In: *Philosophical Magazine A-Physics of condensed matter structure defects and mechanical properties* 50.1 (1984), pp. 45–55. DOI: 10.1080/01418618408244210.
- [36] M. S. Daw and M. I. Baskes. ‘Semiempirical, quantum-mechanical calculation of hydrogen embrittlement in metals’. In: *Physical Review Letters* 50.17 (1983), pp. 1285–1288. DOI: 10.1103/physrevlett.50.1285.
- [37] F. Ercolessi, M. Parrinello and E. Tosatti. ‘Simulation of gold in the glue model’. In: *Philosophical Magazine A-Physics of condensed matter structure defects and mechanical properties* 58.1 (1988), pp. 213–226. DOI: 10.1080/01418618808205184.
- [38] P. Brommer. ‘Entwicklung und Test von Wechselwirkungspotenzialen in Quasikristallen’. MA thesis. Universität Stuttgart, 2003. DOI: 10.18419/opus-4703.
- [39] L. Verlet. ‘Computer experiments on classical fluids .i. thermodynamical properties of lennard-jones molecules’. In: *Phys. Rev.* 159.1 (1967), 98–&. DOI: 10.1103/physrev.159.98.
- [40] C. Störmer. ‘Sur les trajectoires des corpuscules électrisés dans l’espace sous l’action du magnétisme terrestre, avec application aux aurores boréales’. In: *Le Radium* 9.11 (1912), pp. 395–399. DOI: 10.1051/radium:01912009011039501.
- [41] W. C. Swope. ‘A computer simulation method for the calculation of equilibrium constants for the formation of physical clusters of molecules: Application to small water clusters’. In: *The Journal of Chemical Physics* 76.1 (1982), p. 637. DOI: 10.1063/1.442716.
- [42] H. Berendsen, J. Postma, W. Vangunsteren, A. Dinola and J. Haak. ‘Molecular-Dynamics with coupling to an external bath’. In: *Journal of chemical physics* 81.8 (1984), pp. 3684–3690. DOI: 10.1063/1.448118.
- [43] W. G. Hoover. ‘Canonical dynamics: Equilibrium phase-space distributions’. In: *Phys. Rev. A* 31.3 (Mar. 1985), pp. 1695–1697. DOI: 10.1103/physreva.31.1695.

-
- [44] S. Nosé. ‘A molecular dynamics method for simulations in the canonical ensemble’. In: *Molecular Physics* 52.2 (June 1984), pp. 255–268. DOI: 10.1080/00268978400101201.
- [45] W. Hoover. *Computational Statistical Mechanics*. Studies in Modern Thermodynamics. Elsevier Science, 2012. ISBN: 9780444596598. URL: <https://books.google.es/books?id=7XSQYjZdRKMC>.
- [46] T. Schneider and E. Stoll. ‘Molecular-dynamics study of a three-dimensional one-component model for distortive phase transitions’. In: *Phys. Rev. B* 17.3 (Feb. 1978), pp. 1302–1322. DOI: 10.1103/physrevb.17.1302.
- [47] http://lammmps.sandia.gov/doc/fix_langevin.html, retrieved on 19-Aug-2016.
- [48] F. Ercolessi and J. Adams. ‘Interatomic Potentials from First-Principles Calculations: The Force-Matching Method’. In: *Europhysics Letters* 26.8 (1994), pp. 583–588. DOI: 10.1209/0295-5075/26/8/005.
- [49] P. Brommer. ‘Development and Test of Interaction Potentials for Complex Metallic Alloys’. PhD thesis. Universität Stuttgart, 2007. DOI: 10.18419/opus-4819.
- [50] S. Kirkpatrick, C. Gelatt and M. Vecchi. ‘Optimization by simulated annealing’. In: *Science* 220.4598 (1983), pp. 671–680. DOI: 10.1126/science.220.4598.671.
- [51] N. Metropolis, A. Rosenbluth, M. Rosenbluth, A. Teller and E. Teller. ‘Equation of state calculations by fast computing machines’. In: *Journal of chemical physics* 21.6 (1953), pp. 1087–1092. DOI: 10.1063/1.1699114.
- [52] A. Corana, M. Marchesi, C. Martini and S. Ridella. ‘Minimizing multimodal functions of continuous-variables with the simulated annealing algorithm’. In: *Acm transactions on mathematical software* 13.3 (1987), pp. 262–280. DOI: 10.1145/29380.29864.
- [53] M. Powell. ‘A method for minimizing a sum of squares of non-linear functions without calculating derivatives’. In: *Computer Journal* 7.4 (1965), pp. 303–307. DOI: 10.1093/comjnl/7.4.303.
- [54] R. P. Brent. *Algorithms for Minimization without Derivatives*. Englewood Cliffs, N.J.: Prentice-Hall, 1973. DOI: 10.1109/TAC.1974.1100629.
- [55] <http://potfit.us.to/wiki/doku.php?id=start>, retrieved on 16-Mar-2016.
- [56] Y. Mishin, D. Farkas, M. Mehl and D. Papaconstantopoulos. ‘Interatomic potentials for monoatomic metals from experimental data and ab initio calculations’. In: *Phys. Rev. B* 59.5 (1999), pp. 3393–3407. DOI: 10.1103/physrevb.59.3393.
- [57] G. Kresse and J. Hafner. ‘Ab initio molecular-dynamics for liquid-metals’. In: *Phys. Rev. B* 47.1 (1993), pp. 558–561. DOI: 10.1103/PhysRevB.47.558.

- [58] G. Kresse and J. Hafner. ‘Ab initio molecular-dynamics simulation of the liquid-metal amorphous-semiconductor transition in germanium’. In: *Phys. Rev. B* 49.20 (1994), pp. 14251–14269. DOI: 10.1103/physrevb.49.14251.
- [59] G. Kresse and J. Furthmüller. ‘Efficiency of ab-initio total energy calculations for metals and semiconductors using a plane-wave basis set’. In: *Computational materials science* 6.1 (1996), pp. 15–50. DOI: 10.1016/0927-0256(96)00008-0.
- [60] G. Kresse and J. Furthmüller. ‘Efficient iterative schemes for ab initio total-energy calculations using a plane-wave basis set’. In: *Phys. Rev.* 54.16 (1996), pp. 11169–11186. DOI: 10.1103/PhysRevB.54.11169.
- [61] S. Plimpton. ‘Fast parallel algorithms for short-range molecular dynamics’. In: *Journal of computational physics* 117.1 (1995), pp. 1–19. DOI: 10.1006/jcph.1995.1039.
- [62] <http://lammps.sandia.gov>, retrieved on 30-Jun-2016.
- [63] B. Dutta and B. Dayal. ‘Lattice Constants and Thermal Expansion of Gold up to 878 C by X-Ray Method’. In: *physica status solidi (b)* 3.3 (1963), pp. 473–477. DOI: 10.1002/pssb.19630030312.
- [64] M. Moreno, V. Kaganer, B. Jenichen, A. Trampert, L. Däweritz and K. Ploog. ‘Micromechanics of MnAs nanocrystals embedded in GaAs’. In: *Physical Review B* 72.11 (2005), p. 115206. DOI: 10.1103/physrevb.72.115206.
- [65] N. Grazhdankina and A. Burkhanov. ‘Elastic Properties of Manganese Arsenide in the Magnetic Transformation Region’. In: *Soviet Physics JETP* 23.6 (1966). URL: http://jetp.ac.ru/cgi-bin/dn/e_023_06_1013.pdf.
- [66] M. Jamal, N. K. Sarvestani, A. Yazdani and A. H. Reshak. ‘Mechanical and thermodynamical properties of hexagonal compounds at optimized lattice parameters from two-dimensional search of the equation of state’. In: *RSC Adv.* 4.101 (Oct. 2014), pp. 57903–57915. DOI: 10.1039/c4ra09358e.
- [67] A. Zieba, K. Selte, A. Kjekshus, A. F. Andresen, O. Smidsrød, C.-O. Pontchour, P. Phavanantha, S. Pramatus, B. N. Cyvin and S. J. Cyvin. ‘Phase Transitions in MnAs.’ In: *Acta Chem. Scand.* 32a (1978), pp. 173–177. DOI: 10.3891/acta.chem.scand.32a-0173.
- [68] M. Dörfler and K. Bärner. ‘The elastic constants of MnAs’. In: *physica status solidi (a)* 17.1 (1973), pp. 141–148. DOI: 10.1002/pssa.2210170113.
- [69] R. W. G. Wyckoff and R. W. Wyckoff. *Crystal structures*. Vol. 1. Interscience New York, 1960. URL: <https://books.google.com/books?id=40uGpwaACAAJ>.
- [70] J. Neighbours and G. Alers. ‘Elastic constants of silver and gold’. In: *Physical Review* 111.3 (1958), p. 707. DOI: 10.1103/physrev.111.707.
- [71] F. Rösch, H.-R. Trebin and P. Gumbsch. ‘Interatomic potentials and the simulation of fracture: C15 NbCr2’. In: *International journal of fracture* 139.3-4 (2006), pp. 517–526. DOI: 10.1007/s10704-006-0065-8.

- [72] A. Stukowski. ‘Visualization and analysis of atomistic simulation data with OVITO—the Open Visualization Tool’. In: *Modelling and Simulation in Materials Science and Engineering* 18.1 (2009), p. 015012. DOI: 10.1088/0965-0393/18/1/015012.
- [73] <http://ovito.org/>, retrieved on 25-Jun-2016.
- [74] R. Fernandez. ‘Sticking and Desorption Coefficients of As₄ and As₂ During Group V and Group III Controlled MBE Growth’. In: *MRS Proceedings*. Vol. 263. Cambridge Univ Press. 1992, p. 71. DOI: 10.1557/proc-263-71.
- [75] K. Balasubramanian. ‘Electronic structure of (GaAs)₂’. In: *Chemical Physics Letters* 171.1 (1990), pp. 58–62. DOI: 10.1016/0009-2614(90)80050-n.
- [76] J. Murray, C. Pupp and R. Pottie. ‘Heat of dissociation of As₄ (g) and the heat of formation of As₂ (g)’. In: *The Journal of Chemical Physics* 58.6 (1973), pp. 2569–2578. DOI: 10.1063/1.1680663.
- [77] C. Morgan, P. Kratzer and M. Scheffler. ‘Arsenic dimer dynamics during MBE growth: theoretical evidence for a novel chemisorption state of As₂ molecules on GaAs surfaces’. In: *Physical review letters* 82.24 (1999), p. 4886. DOI: 10.1103/PhysRevLett.82.4886.
- [78] J. J. BelBruno. ‘Bonding and energetics in small clusters of gallium and arsenic’. In: *Heteroatom Chemistry* 14.2 (2003), pp. 189–196. DOI: 10.1002/hc.10127.
- [79] A. Ishii, K. Seino and T. Aisaka. ‘Role of As₂ molecules on Ga-terminated GaAs (001) surfaces during the MBE growth’. In: *Journal of crystal growth* 236.4 (2002), pp. 511–515. DOI: 10.1016/S0022-0248(01)02226-6.
- [80] D. Murdick, H. Wadley and X. Zhou. ‘Condensation mechanisms of an arsenic-rich vapor on GaAs (001) surfaces’. In: *Physical Review B* 75.12 (2007), p. 125318. DOI: 10.1103/physrevb.75.125318.
- [81] D. Murdick, X. Zhou, H. Wadley, R. Drautz and D. Pettifor. ‘Molecular dynamics simulation of GaAs molecular beam epitaxy’. In: (). URL: http://www.virginia.edu/ms/research/wadley/Documents/Publications/Molecular_Dynamics_Simulation_of_GaA_Molecular_Beam_Epitaxy.pdf.
- [82] D. A. Murdick. ‘Simulating the Atomic Assembly of Gallium Arsenide’. PhD thesis. University of Virginia, 2006. URL: <http://www.virginia.edu/ms/research/wadley/Thesis/DMurdickPhd.pdf>.
- [83] A. Ouerghi, M. Marangolo, M. Eddrief, B. Lipinski, V. Etgens, M. Lazzeri, H. Cruguel, F. Sirotti, A. Coati and Y. Garreau. ‘Surface reconstructions of epitaxial MnAs films grown on GaAs (111) B’. In: *Physical Review B* 74.15 (2006), p. 155412. DOI: 10.1103/physrevb.74.155412.
- [84] J. Sadowski, J. Kanski, L. Ilver and J. Johansson. ‘Surface morphology of MnAs overlayers grown by MBE on GaAs (111) B substrates’. In: *Applied surface science* 166.1 (2000), pp. 247–252. DOI: 10.1016/S0169-4332(00)00428-1.

- [85] M. Kästner, L. Däweritz and K. Ploog. ‘Surface reconstruction, screw dislocations and anisotropic step flow growth of MnAs on GaAs (111) B substrates’. In: *Surface science* 511.1 (2002), pp. 323–330. DOI: 10.1016/S0039-6028(02)01515-7.
- [86] V. Etgens, M. Eddrief, D. Mosca, M. Marangolo and J. George. ‘Growth morphology and magnetism of MnAs/GaAs (001) epilayers’. In: *Journal of magnetism and magnetic materials* 226 (2001), pp. 1577–1579. DOI: 10.1016/S0304-8853(01)00009-9.
- [87] I. N. Stranski and L. Krastanow. ‘Zur Theorie der orientierten Ausscheidung von Ionenkristallen aufeinander’. In: *Monatshefte für Chemie und verwandte Teile anderer Wissenschaften* 71.1 (1938), pp. 351–364. DOI: 10.1007/BF01798103.
- [88] J. W. Matthews. *Epitaxial growth*. English. Ed. by edited by J. W. Matthews. Academic Press New York, 1975, 2 v. : ISBN: 0124809014. DOI: 10.1016/c2013-0-11156-7.
- [89] J. Venables. *Introduction to surface and thin film processes*. Cambridge University Press, 2000. DOI: 10.1017/cbo9780511755651.
- [90] M. Rost. ‘In situ real-time observation of thin film deposition: roughening, zeno effect, grain boundary crossing barrier, and steering’. In: *Physical review letters* 99.26 (2007), p. 266101. DOI: 10.1103/physrevlett.99.266101.
- [91] STM movie: Real Time Observation of Polycrystalline Thin Film Growth / Deposition. <https://www.youtube.com/watch?v=1D5tdT0dTgw>, retrieved on 30-Jun-2016.
- [92] H. Föll. *Defects in Crystals*. http://www.tf.uni-kiel.de/matwis/amat/def_en/, retrieved on 14-Jul-2016.
- [93] S. T. Chill, M. Welborn, R. Terrell, L. Zhang, J.-C. Berthet, A. Pedersen, H. Jónsson and G. Henkelman. ‘EON: software for long time simulations of atomic scale systems’. In: *Modelling and Simulation in Materials Science and Engineering* 22.5 (May 2014), p. 055002. DOI: 10.1088/0965-0393/22/5/055002.
- [94] <http://theory.cm.utexas.edu/eon/index.html>, retrieved on 05-Aug-2016.

Danksagung

Mit der Fertigstellung dieser Dissertation neigt sich eine interessante, prägende, spannende, fordernde, aufschlussreiche, informative und vor allem lange Studienzeit allmählich dem Ende entgegen. In dieser Zeit haben zahlreiche Personen, direkt oder indirekt, bewusst aber auch unbewusst, im Großen wie im Kleinen ihren Anteil dazu beigesteuert, dass ich auf meinem Studienweg nicht stecken geblieben bin, sondern erfolgreich bis hierhin bestreiten konnte. Jetzt, wo der Abschluss meiner Promotion kurz bevor steht, findet sich wohl wohl kein besserer Moment als an dieser Stelle die Gelegenheit zu ergreifen, all diesen Personen ein aufrichtiges Dankeschön für diese Wegbegleitung auszusprechen.

Eine der letzten Hürden dieses Weges war die Doktorarbeit, die mich abschließend nochmal vor einige Herausforderungen stellte. Auch hier sind viele Leute verantwortlich dafür, dass diese Herausforderungen auch bewältigt wurden. In erster Linie geht daher ein Dank an ...

- *Prof. Dr. Christian Heiliger*, meinen Doktorvater, der mir die Möglichkeit gegeben hat in seiner Arbeitsgruppe zu promovieren und meine Arbeit auch betreute. Ich danke ihm für seine Unterstützung, die ich über die Jahre von ihm erfahren habe, das interessante Promotionsthema, welches mich in das Gebiet der Computersimulation geführt hat, sowie die Besuche von internationalen Workshops und Konferenzen, insbesondere den kurzen Aufenthalt in Japan, die er mir bereitwillig gestattete. Die Zeit in seiner Arbeitsgruppe war sehr lehrreich und ich konnte wertvolle Erfahrungen für die Zukunft sammeln.
- *Prof. Dr. Peter J. Klar* für die unkomplizierte Übernahme des Zweitgutachtens und die sonstige problemlose Zusammenarbeit, sowie die am Ende einfache aber auch hilfreiche und augenöffnende Erkenntnis, dass das Verfassen einer Arbeit in englischer Sprache auch bildet.
- *Dr. Matthias Elm*, der erste Ansprechpartner zu Fragen und Problemen, welche die experimentelle Seite meines Promotionsthema betrafen. Er war diesbezüglich immer ansprechbar und hilfsbereit, was zu notwendiger Aufklärung und Verständnis meinerseits führte. Zudem ist er derjenige, der auf die Idee kam, mir die Reise zu den Kollaborationskollegen in Japan vorzuschlagen und sich im Zuge dessen als hervorragender Reisebegleiter und -leiter erwies, indem er mir u.a. die Einführung und Vorstellung am Forschungsinstitut in Sapporo

erleichterte. Dort hatte ich die einmalige Gelegenheit Vorort zu verstehen und zu lernen, wie die MnAs Nanocluster im Labor hergestellt werden.

- *Alle Mitglieder der AG Heiliger.* Traten Probleme jeglicher Art bei meiner Forschungsarbeit auf, konnte ich mich darauf verlassen bei jedem Mitglied der AG Hilfe zu erfragen. Im Rahmen ihrer Zeit und Möglichkeiten haben sie mir immer ihre Unterstützung angeboten. Bezüglich fachlichen Inhalten, aber auch besonders zu technischen Fragen wie z.B. den Rechnungen auf den Computer-Clustern, konnten sie mir meistens entscheidend weiterhelfen.
- *Prof. Dr. Shinjiro Hara.* I would like to thank him for kindly answering all my questions concerning his research work and its connection to mine, in particular the MnAs nanocluster surface facets, and the interest he took in my research work during our discussions. It was a great help. Further, I want to take this opportunity to express my gratitude to him and his group members at the Research Center for Integrated Quantum Electronics for the friendly welcome and the great hospitality. I had a wonderful time in Sapporo and it was a trip I will never forget.
- *Dr. Benedikt Kramm,* der einen entscheidenden Beitrag leistete, indem er mir eine schnelle Einführung in Origin gab, sodass ich sehr zeitsparend die benötigte Potential-Datenbank aufbauen konnte, ohne die eine umfassende Optimierungsanalyse nicht zum Erfolg geführt hätte. Er stand mir mit Tipps und gutem Rat zu Verfügung, vor allem in der Schreibphase der Doktorarbeit, und mutierte stellenweise zu meinem persönlichen psychologischen Berater, der für die freizeitliche Ablenkung, Motivation und Aufmunterung sorgte.
- *Dr. Florian Gather* für die vielen Ratschläge in den letzten Monaten. Er lieferte Unterstützung beim Aufsetzen des Formats für die Doktorarbeit und wollte es sich nicht nehmen lassen trotz gut gefüllter Berufstage sich beim Korrekturlesen zu revanchieren. Seit des Beginns unseres Studiums bestand zwischen uns eine gegenseitige Zusammenarbeit und trotz der mittlerweile größeren Entfernung haben wir den regen Austausch beibehalten können.
- *Dr. Thomas Sander,* der stets ein offenes Ohr für Fragen und Probleme hatte, die ein Doktorrand vor Beendigung der Promotion so haben kann. Er zeigte wertvolles Verständnis für meine Situation und versuchte mich wo es ging zu unterstützen. Des Weiteren war er daran beteiligt den Blick über die Promotionszeit hinaus zuschärfen, was insbesondere eine motivierende Wirkung hatte.
- die weiteren Korrekturleser *Carsten Mahr, Raphael Knecht, Marcel Giar* und *Eva Basalo Cibeiras,* die sich, obwohl sie selbst viel eigene Arbeit zu bewältigen hatten, Zeit nahmen meine Entwürfe gewissenhaft Korrektur zu lesen.
- das *I. Physikalische Institut,* insbesondere die vielen fleißigen Helfer im Vorder- sowie Hintergrund, die das Institut am „Leben“ halten und bei vielen Gele-

genheiten ihre Hilfsbereitschaft unter Beweis stellen. Sie haben dafür gesorgt, dass ich eine angenehme Zeit am Institut verbringen konnte.

- *meine Freunde*, welche die richtige Ablenkung während der Promotionszeit lieferten. Ob musikalische Aktivitäten mit den Mitgliedern der ehemaligen *IPI-Band*, die intensiven Diskussionen des IPI-Band-Stammtisches mit *Achim Kronenberger* und *Benedikt Kramm*, die sportlichen und freizeitlichen Betätigungen mit den *Kollegen der TSG Lollar* oder die gemeinsamen Ausflüge und Besuche meiner *Jungs & Mädels* aus ganz Deutschland, alles trug dazu bei, dass ich die Forschungsarbeit auch mal gedanklich zur Seite legen konnte.
- *meine Familie*, deren stetige und unermüdliche Unterstützung für alle Belange ich vor allem in den schwierigen Phasen besonders gespürt habe. Auch die neuen Mitglieder der Familie, unser jüngstes Mitglied mit eingeschlossen, haben hierbei mitgewirkt. Dafür bin ich unendlich dankbar.

Versicherung gemäß § 17 Absatz 2 der Promotionsordnung der Gemeinsamen Kommission Naturwissenschaften für die Naturwissenschaftlichen Fachbereiche der Justus-Liebig-Universität Gießen vom 4. Februar 2005

Ich erkläre: Ich habe die vorgelegte Dissertation selbständig und ohne unerlaubte fremde Hilfe und nur mit den Hilfen angefertigt, die ich in der Dissertation angegeben habe. Alle Textstellen, die wörtlich oder sinngemäß aus veröffentlichten Schriften entnommen sind, und alle Angaben, die auf mündlichen Auskünften beruhen, sind als solche kenntlich gemacht. Bei den von mir durchgeführten und in der Dissertation erwähnten Untersuchungen habe ich die Grundsätze guter wissenschaftlicher Praxis, wie sie in der „Satzung der Justus-Liebig-Universität Gießen zur Sicherung guter wissenschaftlicher Praxis“ niedergelegt sind, eingehalten.

Gießen, den 24. Oktober 2016

Andreas Rühl